Investigation of ternary AlInN and quaternary AlGaInN alloys for High Electron Mobility Transistors by Transmission Electron Microscopy

Hichem Ben Ammar

Normandie Université

THESE

Pour obtenir le diplôme de doctorat

Spécialité PHYSIQUE

Préparée au sein de l'ENSICAEN et de l'UNICAEN

Investigation of ternary AlInN and quaternary AlGaInN alloys for High Electron Mobility Transistors by Transmission Electron

Présentée et soutenue par
Hichem BEN AMMAR

Thèse soutenue publiquement le 01/12/2017 devant le jury composé de		
Madame Valérie POTIN	Maître de conférences HDR, Université de Bourgogne Franche-Comté	Rapporteur
Monsieur Jean-Luc MAURICE	Directeur de Recherche CNRS, École Polytechnique Palaiseau	Rapporteur
Madame Laurence MECHIN	Directeur de Recherche CNRS, ENSICAEN	Examinateur
Monsieur Farid MEDJDOUB	Chargé de Recherches CNRS HDR, Université de Lille 1	Examinateur
Madame Magali MORALES	Maître de conférences HDR, UNICAEN	Examinateur
Monsieur Pierre RUTERANA	Directeur de Recherche CNRS, ENSICAEN	Directeur de thèse

Thèse dirigée par Dr. RUTERANA Pierre, Laboratoire CIMAP

UNIVERSITÉ CAEN NORMANDIE

ENSICAEN ÉCOLE PUBLIQUE D'INGÉNIEURS CENTRE DE RECHERCHE

ED PSIME

CIMAP

Acknowledgments

This thesis has been carried out at CIMAP Laboratory (Centre de recherche sur les Ions, les Matériaux et la Photonique) from October 2014 to October 2017. It was carried out in the scope of the ANR-LHOM project. I'm thankful to Pierre RUTERANA my research supervisor for the countless fruitful discussions, suggestions and support of my work.

My grateful thanks go to Valérie Potin and Jean Luc Maurice who have kindly accepted to review my manuscript and be part of the jury. Farid MEDJDOUB of IEMN carried for device fabrication/characterization and has kindly accepted to be member of the jury, I am very thankful to his valuable inputs. Special thanks go to Magali MORALES, the coordinator of the LHOM project and for having accepted to judge my work as a member of the jury. I am grateful to Laurence MECHIN of GREYC for having shared her valuable expertise AFM, and for accepting to judge my work as a member of my jury.

My gratitude goes to Albert MINJ for his help and the answers he brought to my many questions. I am also grateful toward all the collaborators from the different institutions involved in the LHOM project, especially Piero GAMARRA and his colleagues from III-V Labs who performed the growth of most of the materials that have been investigated. I also would like to acknowledge Lorenzo RIGUTTI for the APT measurements.

I would like to thank all the following people that were involved not only in my work but also in everyday life in the lab, special thanks to Marie-Pierre CHAUVAT, Delphine and Phillippe MARIE, Michael BOISSERIE, Thomas DIETSCH, Emmanuel GARDES, Cedric FRILAY, Sylvain FOUBERT, Patrick VOIVENEL, Cédric GENDREAU, and all the colleagues not mentioned from the different teams and laboratories of CIMAP and GREYC.

I would like to thank finally all my friends, Florian, Jennifer, Nicolas, Lucile, Nicolas (they are two), Charlène, Anaïs, Clément, Basile, … Thanks for all the enjoyable moments that we have spent together during these three years.

The problem is not the problem; the problem is your attitude about the problem.
“Cpt. Sparrow”

Table of contents

Résumé

Les Nitrures

Les semi-conducteurs III-N possèdent des propriétés remarquables et sont largement étudiés depuis les années 90. D'une part, AlN, GaN et InN ont leurs bandes interdites directes à 6.2 eV, 3.39 eV et 0.65 eV, respectivement. Par conséquent, les alliages AlGaN, InGaN et AlInN couvrent le spectre de longueur d'onde du lointain ultra-violet (UV) au proche infrarouge (IR). En comparaison à d'autres semi-conducteurs III-V, III-As et III-P ne couvrent le spectre que de l'IR au jaune. D'autre part, les propriétés physiques et chimiques des III-N leur confèrent une bonne stabilité. Par conséquent les dispositifs à base de ces matériaux sont susceptibles de fonctionner dans des conditions extrêmes telles que très hautes températures ou forts courants. Les nitrures sont donc de très bons candidats pour la fabrication de composants avec applications tant dans les domaines civils que militaires. Ils sont employés dans les diodes électroluminescentes (LED pour « light emitting diodes »), dans l'électronique de puissance, etc…. En effet les LEDs et les lasers bleus sont désormais disponibles sur le marché. Néanmoins, un certain nombre de problèmes subsistent. Les III-N sont le plus souvent utilisés sous forme de couches minces obtenues par la croissance épitaxiale sur des substrats faits d'autres matériaux. Ceci est à l'origine de la contrainte entre couche et substrat et de grandes densités de défauts cristallins qui dégradent la qualité des dispositifs et réduit leur efficacité. Plus particulièrement, il reste quelques défis technologiques dont 1) la fabrication de sources de lumière blanche sans avoir recours à l'utilisation d'un phosphore convertisseur. 2) la fabrication de transistors à effet de champ, appelés aussi Transistors à Haute mobilité Electronique (HEMT pour « high electron mobility transistor ») à base de barrière AlInN épitaxié sur GaN, pouvant travailler avec de forte densité de puissance à très haute fréquence.

Le premier rapport connu sur AlN synthétisé en chauffant de l'azote gazeux avec de l'aluminium dans un tube a été publié en 1907. Plus tard en 1910, InN a été obtenu et, enfin, en 1932 le GaN a été produit par un mélange de gaz d'ammoniac condensé et de « gallium tribromide ».

Quand des techniques de croissance plus modernes ont été développées, GaN a ensuite été épitaxié en phase vapeur hybride (HVPE pour « hydride vapor phase epitaxy ») en 1969. Par la suite, AlN et GaN ont été synthétisés sur saphir par l'épitaxie en phase vapeur d'organométallique (MOVPE pour « metal organic vapour phase epitaxy »), mais aussi par épitaxie par jets moléculaire (MBE pour « molecular beam epitaxy »). Au début des années 1980, les recherches sur ces composés ont explosé à partir de la mise au point des couches tampons déposées à basse température et du dopage p-GaN par le magnésium, conduisant naturellement à la fabrication de LEDs comme UV-LEDs, des Lasers et LEDs violettes.

Parallèlement au développement du marché des LEDs, les dispositifs microélectroniques et plus particulièrement les HEMTs connaissent un essor important. En effet, en comparaison à d'autres semi-conducteurs comme le silicium on s'attend à de plus forte puissance en utilisant les nitrures. La première démonstration de la haute mobilité électronique a été faite sur l'héterostructure AlGaN/GaN grâce aux polarisations spontanée et piézoélectrique qui donnent naissance à une densité de gaz bidimensionnel (2DEG pour « 2 dimensional electron gas») à l'interface.

Parmi les alliages (Al, Ga, In)-N, $Al_{1-x}In_xN$ a son paramètre accordé à celui du GaN pour x=0.18. En 2001, une étude théorique a montré que des HEMTs basé sur AlInN devraient présenter des performances meilleures que ceux utilisant des barrières AlGaN. Ceci grâce à la charge induite par une plus forte polarisation spontanée dans AlInN conduisant à une densité plus grande du 2DEG. Une autre propriété intéressante est la différence entre les indices de réfraction entre AlInN et GaN (environ 7%), ainsi des miroirs de Bragg (DBR pour « distributed Bragg reflectors ») avec une réflectivité presque de 100% ont été fabriqués. Ceci a constitué un pas important vers la fabrication de laser à cavité verticale (VCSEL pour « vertical-cavity surface-emitting laser »)

En comparaison à l'AlInN, l'alliage quaternaire AlGaInN offre des degrés de liberté supplémentaires. En effet par rapport au GaN, on peut 1) accorder séparément les bandes interdites et les paramètres de maille et 2) ajuster séparément les polarisations spontanée et piézoélectrique

Objectifs

Ce travail a été effectué dans le cadre du projet ANR-LHOM (AlInN Layers and AlInN Heterostructures for Optimized high electron Mobility transistors). En collaboration avec les équipes partenaires du projet (IEMN, III-VLab, GREYC), ma contribution a été centrée sur la caractérisation par microscopie électronique en transmission (TEM pour « transmission electron microscopie ») des alliages AlInN et AlGaInN. Le but était ainsi d'aider à comprendre les mécanismes de croissance de ces alliages et d'assurer le suivi de la structure des dispositifs vers une optimisation de leur performance.

La difficulté de l'épitaxie de ces matériaux réside dans le fait que les composés binaire de base ont des propriétés physiques assez différentes. Par exemple, les températures de croissance MOVPE pour AlN, GaN et InN sont >1200 °C, 1000 °C et < 600 °C, respectivement. Tous les travaux récents montrent que les surfaces de couches épitaxiales de ces alliages sont parsemées de pyramides inversées dénommées 'pinhole' dont la formation a été longtemps reliée à la présence des dislocations traversantes dans les couches sous-jacentes. Plus récemment, ce type de défauts a été aussi rapporté après une croissance d'AlInN sur du GaN avec taux de défauts très faible ($<10^5$ cm^{-2}), il a alors été proposé qu'il devait y avoir un mécanisme intrinsèque de formation de ces pinholes par coalescence des zones de croissance à trois dimension (hillocks). Au cours de ce travail de thèse, on a donc cherché à comprendre la structure de ces alliages par une étude détaillée de microscopie. Ainsi, nous avons étudié le processus d'épitaxie MOVPE et les influences des paramètres de croissance sur la qualité des barrières. Ce faisant, nous avons mis en évidence les différents types de défauts à commencer par ceux provenant des couches sous-jacentes et leurs effets sur la structure de l'alliage. Ensuite, nous nous sommes attachés à analyser en détail les dégradations intrinsèques de ces alliages qui se manifestent spontanément lorsque l'épaisseur des couches est augmentée et sans présenter d'épaisseur critique de formation.

Ce travail est discuté en sept chapitres

Le **chapitre 1** présente les propriétés structurelles des nitrures. Nous avons, d'abord, décrit la principale phase dans laquelle ces matériaux cristallisent (la structure wurtzite). Les propriétés de polarisations, les origines de la polarisation spontanée et piézoélectrique ont été ensuite discutées. Nous nous sommes ensuite intéressés aux alliages AlInN et AlGaInN pour lesquels nous avons récapitulées les principales propriétés structurelles. Finalement, les principaux défauts cristallographiques rencontrés dans la structure wurtzite ont été discutés.

Le **chapitre 2** concerne les techniques de caractérisation utilisées durant ce travail. Les topographies ont été étudiées avec la microscopie à force atomique (AFM pour « atomic force microscopy ») pour déterminer les morphologies de surface et les rugosités. Une bonne partie des lames minces pour microscopie électronique en transmission (TEM pour « transmission electron microscopy ») a été préparée par faisceaux d'ions focalisés (FIB pour « focused ion beam »). Le TEM constitue la technique de caractérisation principale utilisée durant ce travail de thèse. Grâce au TEM, les défauts cristallins sont observés, différenciés et caractérisés par type et origine potentiel. La microstructure des couches minces a été observée jusqu'à l'échelle atomique.

Nous avons aussi pu avoir accès à la sonde atomique tomographique (APT pour « atome probe tomography ») qui a été utilisée pour déterminer la distribution atomique tridimensionnelle. Cette dernière a été le fruit d'une collaboration avec le GPM de l'université de Rouen. Elle nous a apporté une bonne confirmation des résultats de TEM.

Le **chapitre 3** présente d'abord la technique de croissance MOVPE. Elle est à l'origine de toutes les couches minces étudiées ; elles ont été élaborées dans deux chambres de croissance de géométries différentes, l'une dite horizontale, la seconde verticale. La première chambre permet de croître des alliages AlInN ternaires, alors que dans le bâti vertical, une incorporation non intentionnelle de galium est observée conduisant à un alliage quaternaire AlGaInN. Dans ce chapitre, nous avons essayé d'expliquer l'origine de l'incorporation du Ga en analysant les effets de la géométrie de la chambre et l'influence des paramètres de dépôt.

Suite à cette étude, les sources de cette incorporation sont les parois internes de la chambre verticale ainsi que de la paroi d'accès des organométalliques connue sous le nom de « shower head ». Nous avons ensuite observé que la quantité de gallium incorporée peut être réduite de deux manières. 1) une réduction à 2% si la chambre de dépôt est préalablement nettoyée donc en éliminant le gallium résiduel, ou 2) à 6% en faisant l'épitaxie à 80 Torr qui semble diminuer la réactivité du gallium résiduel.

Le **chapitre 4** a été consacré à l'étude des défauts extrinsèques qui sont dus aux dislocations traversantes et des domaines d'inversions issus du GaN. En croisant, les données d'AFM et du TEM, nous avons mis en évidence que les dislocations de type « a+c » et « c » s'ouvrent en pinholes localisés au milieu d'hillocks ayant des dimensions plus grandes qu'une dislocation de type « a ». Parmi les défauts observés, nous avons répertorié des tranchés, dus à des domaines d'inversion dans le GaN. La formation des tranchées a été expliquée par la dynamique de croissance autour d'une région GaN de polarité azote au-dessus duquel la vitesse de croissance est réduite. On montre aussi que la contrainte observée entre les régions de différentes polarités est accompagnée par 1) la fluctuation de compositions entre des régions riches en aluminium ou en indium et 2) l'interaction avec une couche AlN à l'interface AlGaInN/GaN. Le résultat sur la morphologie de surface se manifeste par l'apparition d'un certain nombre de tranchées autour du domaine d'inversion. En fonction de l'épaisseur de la couche mince, ces tranchées peuvent présenter de pinholes séparés ou non.

Par ailleurs, dans cette analyse, nous montrons qu'une certaine population des « pinholes » n'est pas reliée aux dislocations et découle donc d'une dégradation intrinsèque de la couche d'alliage.

Dans **chapitre 5**, nous montrons d'abord que la condition d'accord de paramètres de mailles peut être obtenue pour des températures de croissance différentes. Cependant, la qualité des couches dépend fortement de ces conditions de croissance et notamment, la rugosité de surface peut être réduite avec un jeu de paramètres adéquats. Dans les conditions que nous avons pu explorer, la morphologie obtenue indique que la croissance est toujours de façon tridimensionnelle.

Le **chapitre 6** présente une analyse des défauts intrinsèques de ces alliages. En effet, même avec des conditions de croissance optimisées et pour des couches accordées en paramètres de maille, si on augmente l'épaisseur on observe 1) de fortes fluctuations de compositions pouvant dépasser les 30% 2) des structures polycristallines ayant des désorientations localisées 3) une forte rugosité indiquant une accentuation du mode de croissance en 3D.

Durant ce travail, nous avons collaboré aussi à la caractérisation de dispositifs HEMTs. Les résultats de cette contribution sont récapitulés dans le **chapitre 7**. Les principaux constituants optimisés sont les contacts ohmiques et Schottky ainsi que la couche de passivation. Une comparaison des caractéristiques de nos dispositifs avec la littérature y est rapportée. Grâce aux améliorations apportées durant le projet LHOM aux différentes parties du dispositif, nous avons atteint une mobilité électronique de l'ordre de 1800 $cm2V^{-1}s^{-1}$ avec une densité du 2DEG de 2×10^{13} cm^{-2}. Actuellement, ces transistors peuvent supporter des tensions jusqu'à 200 V et ont démontré une fréquence de coupure de 260 GHz.

Introduction

I. III-Nitrides

Group III-Nitrides based on aluminum, gallium and indium exhibit outstanding properties and have been investigated since early 1900. On one hand, AlN, GaN, and InN have direct band gaps of 6.2 eV, 3.39 and 0.65 eV, respectively[1]. Therefore, their alloys cover from deep ultraviolet (UV) to near infrared (IR) across the visible range of wavelengths. In comparison, other III-V semiconductors such as III-As and III-P have their band gap ranging from IR to yellow as shown in figure 1.

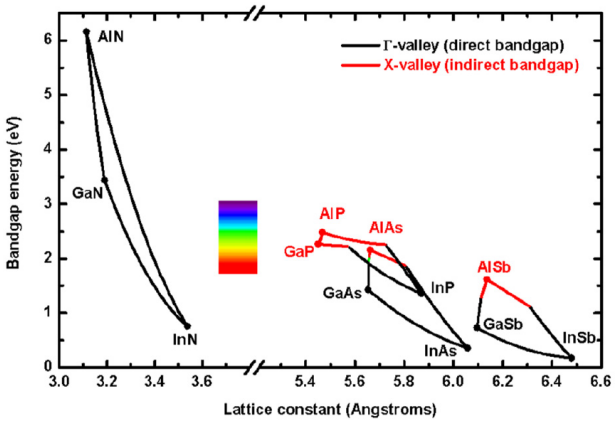

Figure 1: Band gap of semiconductors plotted as a function of their lattice parameter[2].

On the other hand, the short bond lengths of the binary compounds lead to high bond energy. Therefore, III-Nitrides have high thermal and chemical stability. Thus they can stand harsh working conditions such as high temperatures as well as high voltages and currents. These properties make them suitable for many applications in both civil and military fields; high power electronics, LEDs, etc….. Indeed, the blue LEDs and lasers are now commercially available, as well as their translation to solid-state lighting. The main drawback of III-N is that no suitable native substrate is available for the growth of the active devices; this is at the origin of high strain and high density of crystallographic defects in the heterostructures which degrade the quality of the devices. In particular, there are still two main challenges: 1) the fabrication of white light without the use of phosphors which will rely on the growth of good quality high indium content InGaN/GaN quantum wells, 2) the production of high-performance AlInN/GaN high mobility transistors for high speed, high density, high power telecommunication.

The first record for AlN was in 1907[3] which was synthesized by heating gaseous nitrogen with aluminum in a tube. Later, in 1910[4], InN was synthesized and then in 1932[5] GaN was produced by a mixture of condensed ammonia gas and gallium tribromide. After modern growth techniques have been developed, GaN was epitaxially grown by hybrid vapor phase epitaxy (HVPE) in 1969[6] and then AlN and GaN by metal organic vapor phase epitaxy (MOVPE)[7] and later AlN by means of molecular beam epitaxy (MBE)[8]. In these instances, the used substrate was sapphire. Starting in the 1980's, these compounds went under huge investigation after the discovery of GaN p-doping by magnesium[9,10] which bridged towards the fabrication of light emitting diodes (LEDs) such as UVLEDs[11,12], lasers[13], and violet LEDs[14].

Beside the development of the LED market, microelectronic devices, especially high electron mobility transistors (HEMTs), have also been extensively investigated. Indeed, in comparison to other semiconductors like silicon-based devices, it is expected to attain higher output power densities using III-N devices. The first demonstration of enhanced electron mobility has been demonstrated on AlGaN grown on GaN[15,16] which is due to strain and the spontaneous piezoelectric polarization which can be tuned to have a two-dimensional gas (2DEG) at an adequate hetero-interface.

Among the (Al, Ga, In)-N alloys family, $In_xAl_{1-x}N$ exhibits the above properties and in addition, it can be grown lattice-matched (LM) to GaN and thus suppress the strain when the molar fraction of InN is $x \approx 18\%$. In 2001, Kuzmik et al.[17] theoretically predicted that LM-AlInN based HEMT should exhibit higher drain currents than those using AlGaN barriers. He pointed out that this is due to the higher polarization-induced charge in AlInN leading to a higher density of 2DEG. Another interesting property of these LM alloys was reported just after in 2003 by Carlin and Ilegems[18,19], they grew LM-AlInN/GaN distributed Bragg reflectors with a nearly 100% reflectivity due to the high contrast between the refractive indices around 7%. This constituted an important step toward vertical cavity surface emitting lasers (VCSELs). Since then, as shown in figure 2 which represents a statistical survey retrieved from *Web of Science*[20], the number of publications counts using (In, Al)N as keywords have increased steadily. However, since 2010, the number has settled to

a maximum of around 100/year. This is probably due to the difficulties encountered in growing high-quality layers[18,19,21].

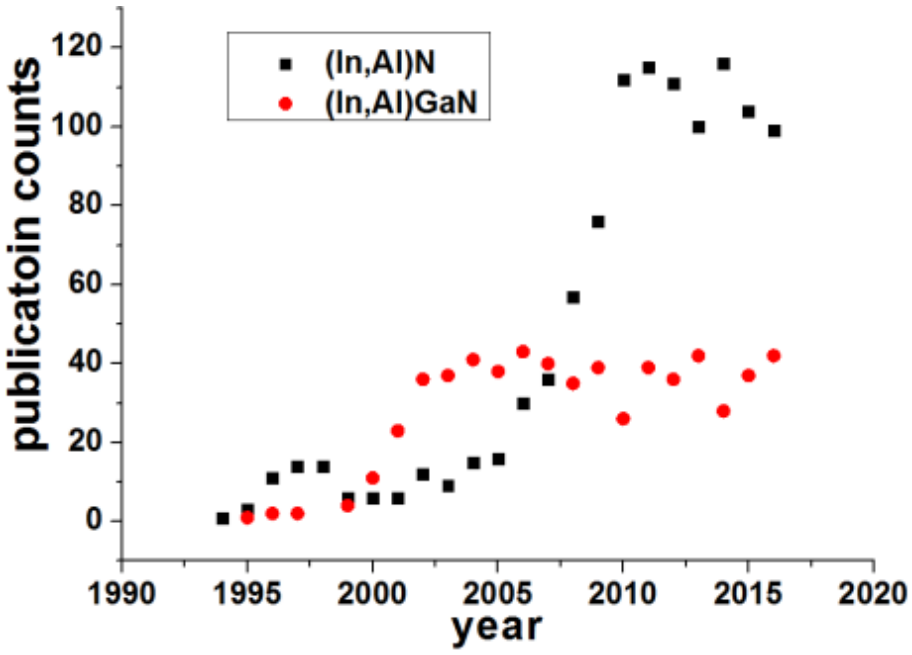

Figure 2: Records statistics according to Web of Science with InAlN, AlInN, AlInGaN and InAlGaN as keywords entry

In comparison to AlInN, the quaternary alloy AlGaInN offers additional degrees of liberty as suggested by McIntosh et al.[22] and then Jena et al.[23]. The latter explored the possibilities of 1) tuning independently the band gap and the lattice parameter and 2) adjusting separately both the spontaneous and piezoelectric polarization as shown in figure 3, which could offer more flexibility in the substrate choice. In particular, AlInN can be grown theoretically lattice matched to GaN at around 18% of indium content[21] and for AlGaInN the lattice match condition may be obtained for more extended indium compositions[24].

As can be seen in figure 2, the first record on quaternary alloys are around 1995[22,25] almost at the same time as AlInN, however, the research on this alloys seems to have taken off more slowly (fig. 2). The quaternary AlGaInN is a promising candidate for power devices[26]; indeed, as has been reported, in comparison to AlInN, AlGaInN might have higher 2DEG and higher electron mobility[24,27] with low leakage current[28].

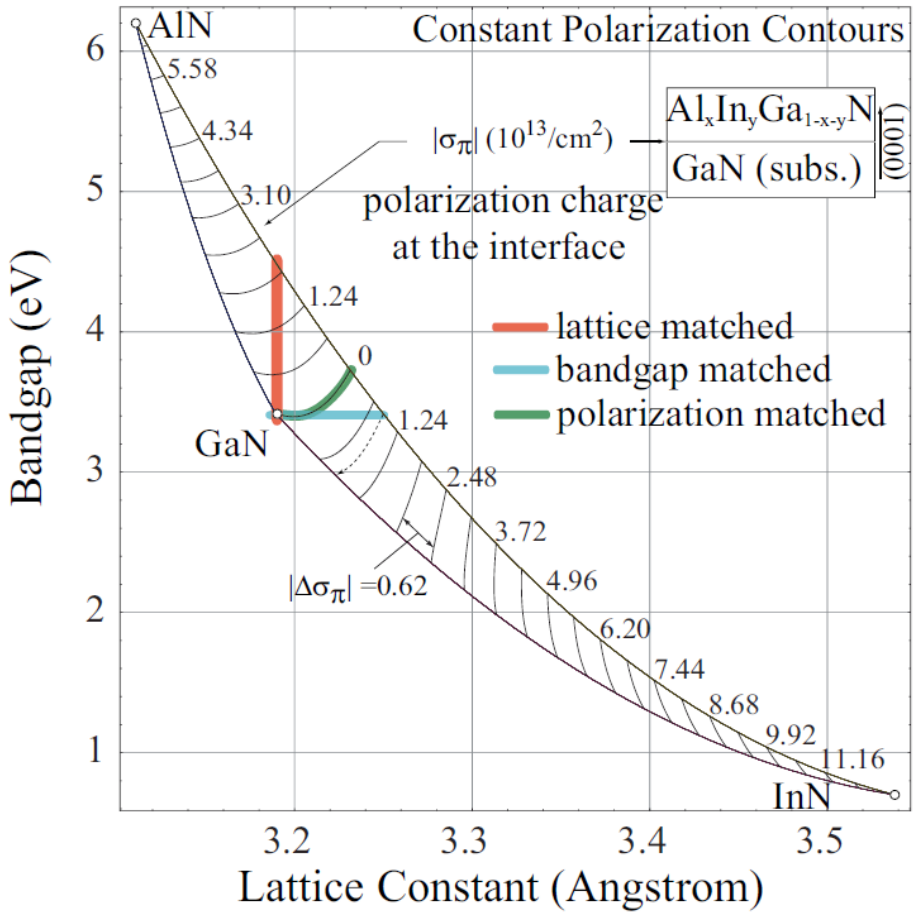

Figure 3: The possibilities that offer AlGaInN alloys in terms of the lattice parameters, bandgap, and polarization matches while grown on (0001)-GaN[23].

II. Objectives

This work was carried out in the frame of the project ANR-LHOM (InAlN Layers and InAlN Heterostructures for Optimized high electron Mobility transistors). In close collaboration with the growers, my contribution was focused on the structural characterization of AlInN and AlGaInN alloys toward the improvement of devices quality and performances. The aim was thus to help understanding defects formation mechanisms with respect to the growth conditions.

In fact, the growth of these alloys is not straightforward due mostly to the highly different physical properties of the end compounds. For instance, the growth temperature for AlN, GaN, and InN are approximately 1200 °C, 800 °C and 600 °C, respectively using MOVPE. Defects are systematically observed and the layers can have poor crystalline quality with high roughness. For instance, dislocations are found to be topped with pinholes at the barriers[29,30]. Furthermore, layers grown on low dislocation density freestanding GaN can develop pinholes when the thickness

is increased[31]. These pinholes are inverted empty pyramids features. In addition, AlInN, as well as AlGaInN are observed to have surface morphology dominated systematically by hillocks. During this work, we have studied the crystalline quality and surface morphology of AlInN and AlGaInN. We have studied the MOVPE setup and growth parameters influences on the barriers quality. Furthermore, we have studied defects that may or may not originate from the underlying GaN. Thus, defects were termed as intrinsic or extrinsic depending on their potential origin in order to better understand their formation mechanisms. Indeed; the scope is to contribute to the understanding of the alloying process during the growth and enhance the quality of HEMTs performances that were fabricated during the project LHOM.

III. Outline

The manuscript is divided into seven chapters.

Chapter 1 introduces the structural properties of group III-Nitrides. The crystal is firstly described then its polar behavior properties. The properties of AlInN and AlGaInN are summarized and lastly the main of crystallographic defects are discussed.

Chapter 2 presents the characterization techniques. On one hand, the samples topographies were observed with atomic force microscopy (AFM). On the other hand, samples for transmission electron microscopy observation (TEM) were prepared. In fact, TEM constitutes the main characterization technique used during this thesis; therefore, in chapter 2, TEM techniques are described, including imaging, defect analysis by diffraction contrast, chemical and strain contrast. Finally, atom probe tomography (APT) was used to access the three-dimensional atomic distribution

Chapter 3 deals with the influence of the growth chamber geometry and growth parameters on the unintentional incorporation of gallium in the intended ternary AlInN alloy leading to a quaternary AlGaInN. The studied layers were grown in two MOVPE chambers both from AIXTRON. They are described in the first part of chapter 3 with the epitaxial process. It is found that gallium is unintentionally incorporated into layers grown in the vertical chamber whereas no Ga is observed when the growth is carried out in the horizontal chamber.

In chapter 4, we firstly, recall the available substrate for III-nitrides. Then, we discuss extrinsic defects that are due to sub-grain boundaries and inversion domains (IDs) from the underlying GaN. It is shown that the dislocations types affect differently the morphology of the terminating pinholes. AFM was used to classify statistically defects through their dimensions. Convergent beam electron diffraction (CBED) was used for IDs characterization in TEM, finally, the conventional TEM determination of the dislocation types was found to correlate with the AFM statistical analysis. In this analysis, we show that a substantial fraction of pinholes population is not connected to dislocations.

In chapter 5, we discuss the effects of the growth conditions on the structural and morphological quality of AlInN and AlGaInN. We show that the lattice match condition can be obtained for different growth temperatures and V/III ratios while the average quality of the layers depends strongly on these growth conditions as well as the growth pressure. In this instance, we found that for optimized growth conditions compositional fluctuation can be decreased to few percent, and the surface morphology is dominated by extrinsic defects.

In addition to the extrinsic defects, systematic degradations are commonly observed in AlInN and AlGaInN. These are intrinsic to the alloy and are discussed in chapter 6. Even with optimized growth conditions at the lattice match condition, increasing the thickness or changing the nominal composition of the alloy (thanks to the flexibility of AlGaInN) lead to strong fluctuations, polycrystalline structures with high roughness. It is further found that this begins from the early stages of the growth in a three dimensional way. In this chapter, mechanisms of these degradations are discussed.

During this thesis, we have collaborated in the characterization of HEMTs devices. The results of our work are summarized in chapter 7. The main optimized constituents of the studied devices are the ohmic and Schottky contacts and the silicon nitride passivation layer. A comparison of the characteristics before and after optimization is discussed with respect to the available data in the literature.

1 Properties of III-Nitrides

The aim of this chapter is to summarize the structural properties of group III-N. The crystalline structure is firstly described, then, their polar character is addressed. The properties of the alloys that have been studied in this work are next addressed. Finally, the common crystallographic defects are recalled.

1.1. Crystalline structure

Group III-N namely AlN, GaN, InN and their ternary and quaternary alloys may occur in three different crystallographic structures. They may crystallize in wurtzite (hexagonal), zinc blende (cubic) and rock salt (cubic). The corresponding space groups are $P6_3mc$, $F\bar{4}3m$ and $Fm\bar{3}m$, respectively. The wurtzite configuration is the most stable at room temperature and atmospheric pressure, while the zinc blend and the rock salt are metastable[32,33]. In this manuscript only the wurtzite phase will be considered, it is exhibited in figure 1.1a. It is formed by two close packed hexagonal (hcp) sub-lattices of group III metals (Al, Ga, In) and group V (N), connected by a translation vector. The hcp unit cell is formed by 3 equivalent primitive unit cells where each atom occupies a tetrahedron site leading to 4 atoms per unit cell. The translation vector from the III to V atoms is $\vec{u} = (3/8)\,\vec{c}$ along the growth direction considered in this manuscript: $\vec{c} = c[0001]$ where its modulus denotes the "c" lattice parameter. It is worth to mention that "u" represents the anion to cation distance and will depend on their respective radii.

The hexagonal basis set is formed by $\vec{a}_1, \vec{a}_2, \vec{a}_3$ *and* $\vec{c}$ vectors as depicted in figure 1.1b. The vectors of the basal c-plan are 120° apart. $\vec{c}$ is orthogonal to c-plan. For each direction a four indices (h, k, i, l) notation is assigned where $i = -(h + k)$. This notation is useful to designate equivalent families of crystallographic plans and directions by exchanging the three first indices.

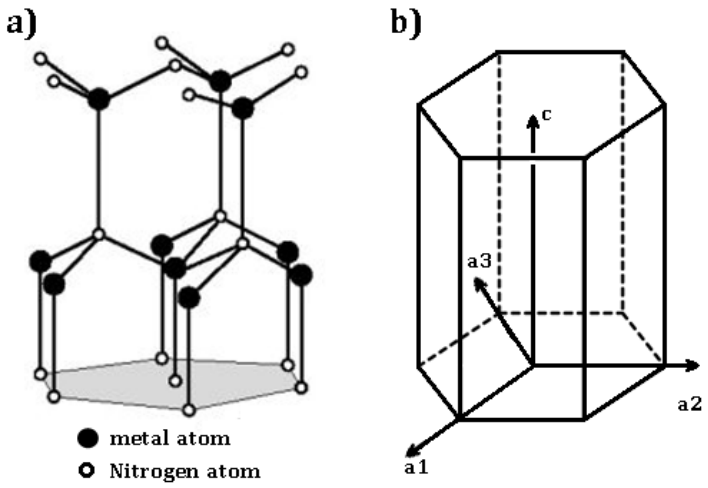

Figure 1.1: a) Wurtzite stacking of group III (Al, Ga or In) and group V (N) atoms of nitride semiconductors b) the hexagonal unit cell.

The lattice parameters of the three compounds AlN, GaN, and InN are given in table1.1[1]. As can be seen, in this materials family, where only the metal atom is changing from one compound to the other, any heterostructure growth along the c axis leads to a large mismatch as high as 13% in the case of growth of InN on AlN. This misfit is obtained using (1.1) relationship where a_f and a_s designate the film and substrate a-lattice parameter, respectively.

$$\Delta a = \frac{a_f - a_s}{a_s} \qquad 1.1$$

When $\Delta a > 0$, the layer is compressed to the substrate and when $\Delta a < 0$ the layer is under tensile strain. For instance, when grown on GaN, AlN and InN would be under tensile and compressive strain, respectively.

Parameter [Å]	AlN	GaN	InN	Growth on GaN	Mismatch
a_0	3.1114	3.189	3.544	AlN	-0.0243
c_0	4.9792	5.185	5.718	InN	0.1113

Table 1.1: The lattice parameters of III-N compounds[1]. The misfit is calculated with respect to GaN.

1.2. Unit cell deformation: strain and stress

Geometrical modifications of the unit cell can be expressed by a tensor that links the primitive lattice vectors to a new set of basis vectors. It expresses normal and shear modification of the primitive unit cell due to, for example, the mismatch between lattice parameters or thermal expansion coefficients. If the original basis is defined by

an orthonormal set $(\vec{e}_x, \vec{e}_y, \vec{e}_z)$ and the modified one is $(\vec{e}'_x, \vec{e}'_y, \vec{e}'_z)$ then the strain tensor $[\epsilon_{kl}]$ is given by (1.2):

$$[\epsilon_{kl}] = \begin{pmatrix} 1+\varepsilon_{xx} & \varepsilon_{xy} & \varepsilon_{xz} \\ \varepsilon_{yx} & 1+\varepsilon_{yy} & \varepsilon_{yz} \\ \varepsilon_{zx} & \varepsilon_{zy} & 1+\varepsilon_{zz} \end{pmatrix} \quad 1.2$$

The coefficients ε_{kk} represent the normal strain while ε_{kl} represent the shear strain components. When no rotational modifications are involved, the strain tensor is symmetric.

Considering that the modification of the unit cell is due to a set of forces applied to the crystal then it can be described by a stress tensor $[\sigma_{ij}]$. The above tensors are connected by the elastic constants(C_{ijkl}) as follows:

$$\sigma_{ij} = C_{ijkl}\varepsilon_{kl} \quad 1.3$$

Due to the symmetry of $[\epsilon_{kl}]$ the matrix form of the elastic tensor can be simplified in a contracted (6×6) symmetric matrix. The contraction can be obtained using the Einstein summation convention, thus each term of (1.3) can be written as:

$$\sigma_m = C_{mn}\varepsilon_n \quad 1.4$$

Furthermore, it is helpful to consider the symmetry of the crystal to reduce the number of the independent elements of (C_{mn}). In the case of the hexagonal symmetry, this tensor can be written in the following form:

$$C_{mn}^{hexagonal} = \begin{pmatrix} C_{11} & C_{12} & C_{13} & 0 & 0 & 0 \\ C_{12} & C_{11} & C_{13} & 0 & 0 & 0 \\ C_{13} & C_{13} & C_{33} & 0 & 0 & 0 \\ 0 & 0 & 0 & C_{44} & 0 & 0 \\ 0 & 0 & 0 & 0 & C_{44} & 0 \\ 0 & 0 & 0 & 0 & 0 & C_{66} \end{pmatrix} \quad 1.5$$

In the hexagonal system, this 6*6 matrix can take a simpler form, moreover, when the growth is carried out along the [0001] axis, the crystal does not experience stress along the z-axis, as it is free to expand or contract; and the deformation should be isotropic in the basal plane. These conditions lead to the following equalities:

$$\begin{gathered} \sigma_{33} = 0; \\ \sigma_{11} = \sigma_{22} = \sigma_a \end{gathered} \quad 1.6$$

$$\varepsilon_{11} = \varepsilon_{22} = \varepsilon_a$$

Hence, the strain-stress relationship becomes:

$$\begin{pmatrix} \sigma_a \\ \sigma_{33} \end{pmatrix} = \begin{pmatrix} C_{11} + C_{12} & C_{13} \\ 2C_{13} & C_{33} \end{pmatrix} \begin{pmatrix} \varepsilon_a \\ \varepsilon_{33} \end{pmatrix} \quad 1.7$$

Equation (1.7) can be expressed with an in-plane component and an out-of-plane component:

$$\begin{aligned} (\varepsilon_a; \varepsilon_{33}) &= (\varepsilon_{\parallel}; \varepsilon_{\perp}) \\ (\sigma_a; \sigma_{33}) &= (\sigma_{\parallel}; \sigma_{\perp}) \end{aligned} \quad 1.8$$

Taking into account that $\sigma_{33} = 0$, equation (1.7) with (1.8) becomes:

$$\varepsilon_{\perp} = -2\frac{C_{13}}{C_{33}}\varepsilon_{\parallel} \quad 1.9$$

In equation (1.9), $\varepsilon_{\perp} = \frac{c-c_0}{c_0}$, $\varepsilon_{\parallel} = \frac{a-a_0}{a_0}$ where (a_0, c_0) and (a, c) are respectively the relaxed and strained lattice parameters and the term $\left(-2\frac{C_{13}}{C_{33}}\right)$ is the biaxial term. The relation (1.9) shows that, for instance, a layer under compressive in-plane stress will expand in the out-of-plane direction; this is known as the Poisson effect. For the in-plane case, the stress is related to the strain as follows:

$$\sigma_{\parallel} = \left(C_{11} + C_{12} - 2\frac{{C_{13}}^2}{C_{33}}\right)\varepsilon_{\parallel} \quad 1.10$$

The values of the elastic coefficients are given in table 1.2

Compound:	**AlN**	**GaN**	**InN**
C_{11}[GPa]	396	367	223
C_{12}[GPa]	137	135	115
C_{13}[GPa]	108	103	92
C_{33}[GPa]	116	405	224

Table 1.2: Elastic coefficient of binaries III-Nitrides[34]

1.3. Spontaneous and piezoelectric polarizations

In III-N compounds, one has to take into account the electronegativity of each Al, Ga, In and N; it is 1.61, 1.81, 1.78 and 3.04, respectively and it induces a displacement of the negative charges barycenter towards the N-atoms. Therefore, depending on the

crystal symmetry, charge dipoles can be present and the crystal exhibits spontaneous polarization at equilibrium.

For both wurtzite and zinc blende phases, each group III-atom is tetrahedrally bonded to nitrogen atoms. For the zinc blende, the stacking is …ABCABC… along the 4 symmetric [111] directions of the cubic system. Hence, the four dipoles are compensated by the four symmetric equivalent polar family planes <111> and no spontaneous polarization is present. In contrast, for the wurtzite structure, there is only one direction along which the stacking …ABAB… takes place; this direction is [0001]. Along this direction a spontaneous polarization at equilibrium $(\vec{p}_{sp})$ is always present. Therefore [0001] and $[000\bar{1}]$ are not equivalent as the group III-Nitrides have no inversion center**.** By convention, the polarity is defined by the vector pointing from the nitrogen atom to metal atom along the [0001]. Figure 1.2 shows Ga-polar case as projected along $[11\bar{2}0]$ direction. In this instance the $(\vec{p}_{sp})$ points in the opposite direction of the [0001] growth directions.

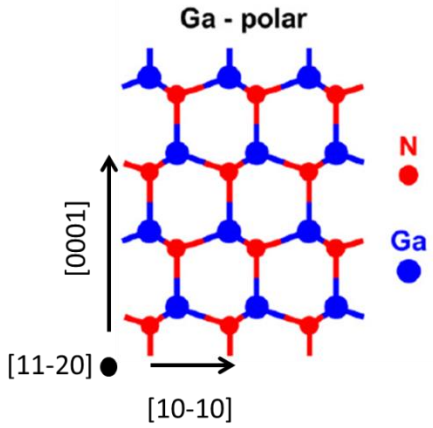

Figure 1.2: Projection of Ga-polar of GaN wurtzite crystal observed along the $[11\bar{2}0]$ *direction[35].*

In the case of the growth of a heterostructure, the lattice mismatch leads to the appearance of additional polarization. This polarization is known as piezoelectric polarization$(\vec{p}_{pz})$. For instance, a $(\vec{p}_{pz})$ can also appear in a zinc blende structure by carrying out the growth along one of the polar directions <111> which cancels out the symmetry along the growth direction as the dipolar momentum is no more compensated. In wurtzite, the growth of a heterostructure along [0001] direction with a lattice mismatch will strain the barrier creating a $(\vec{p}_{pz})$, this will reinforce or decrease $(\vec{p}_{sp})$ depending on the sign of the strain. Thus, the total amount of the

polarization will be the sum of the two contributions $\left([\vec{P}] = [C/m^2]\right)$. The consequence of the dipolar momentum is a specific charge distribution along the whole volume of a layer and the charge density is given by: $\rho_v = -div(P)$. At the surfaces or interfaces, the excess electrical charges are given by: $\sigma_s\vec{n} = P\vec{n}$ where $\vec{n}$ is the normal vector pointing outside of the considered surface. For instance, III-polar surface of a bulk crystal will have a negative charge sheet (σ^-) while N-polar surface will carry a positive charge sheet (σ^+). Figure 1.3 shows the spontaneous polarizations in the case of a) relaxed and the appearance of the piezoelectric polarization in b) stressed GaN with a biaxial tensile strain. Figure 1.3c shows the case of AlN/GaN heterostructure for which AlN is under tensile strain to a relaxed GaN.

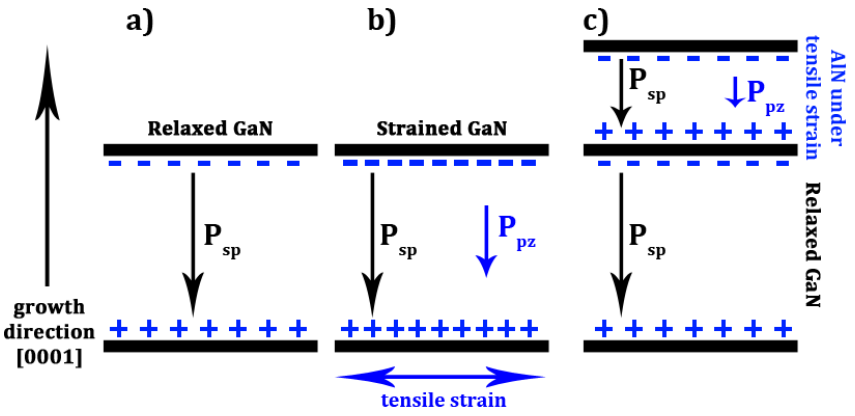

Figure 1.3: The spontaneous and piezoelectric polarizations in the case of a) bulk GaN, b) GaN under tensile strain and c) AlGaN/GaN

The values of the spontaneous polarization were calculated by Bernardini et al.[36] and are reported in table 1.3. More recently, Bechstedt et al.[37] showed that these constants are highly sensitive to infinitesimal changes in the crystal structure such as c/a ratio and bond lengths or even uncertainties in the structural parameters might change drastically the outcome of the simulations. In particular, InN and its alloys still lack reliable experimental data, thus the interpretation of its behavior may still be controversial. The piezoelectric polarization can be determined from the piezoelectric tensor of the corresponding space group. For the wurtzite symmetry $P6_3mc$ space group, it is as follows:

$$p_{pz} = \begin{pmatrix} 0 & 0 & 0 & 0 & e_{15} & 0 \\ 0 & 0 & 0 & e_{15} & 0 & 0 \\ e_{31} & e_{31} & e_{33} & 0 & 0 & 0 \end{pmatrix} \begin{pmatrix} \varepsilon_{11} \\ \varepsilon_{22} \\ \varepsilon_{33} \\ \varepsilon_{23} \\ \varepsilon_{13} \\ \varepsilon_{12} \end{pmatrix} \quad 1.11$$

Where e_{ij} are the piezoelectric elements of the tensor, ε_{kk} are the uniaxial strain elements and ε_{kl} (with k≠l) are the shear strain elements. The values of e_{ij} are also reported in table 1.3. Considering the absence of shear and only the biaxial strain for the growth along [0001], (1.11) can be combined to (1.09) to become:

$$p_{pz}[0001] = 2\frac{a - a_0}{a}\left(e_{31} - e_{33}\frac{C_{13}}{C_{33}}\right) \quad 1.12$$

In devices such as HEMTs, the polarization is of primary importance as it impacts the density of the carrier and the mobility of the 2DEG. In wurtzite symmetry materials, the piezoelectric polarization is one order of magnitude higher than in zinc blende materials and a large spontaneous polarization is indeed present[38].

Compound:	**AlN**	**GaN**	**InN**
P_{sp} [C/m²][39]	-0.09	-0.034	-0.042
e_{33}[C/m²][36]	1.46	0.73	0.97
e_{31}[C/m²][36]	-0.6	-0.49	-0.5

Table 1.3: Spontaneous polarization and piezoelectric coefficients of the III-Nitrides

1.4. Properties of AlInN and AlGaInN alloys

Conventionally, many properties of an alloy like the bandgap energy or lattice parameters can be calculated using a linear combination of those of the parent compounds, and this is known as the empirical Vegard's law. Considering that α and β are the binaries with x the mole fraction of α, then the desired property is extracted from a linear equation (1.13) for a ternary alloy.

$$\Upsilon(x) = x\Upsilon_\alpha + (1 - \mathrm{x})\Upsilon_\beta \quad 1.13$$

Where Υ is the unknown physical property, for a quaternary alloy (1.13), it becomes:

$$\Upsilon(x, y, z) = x\Upsilon_\alpha + \mathrm{y}\Upsilon_\beta + \mathrm{z}\Upsilon_\delta \quad 1.14$$

In (1.14) y and z are the mole fractions of β and δ binary compounds with $\mathrm{x} + \mathrm{y} + \mathrm{z} = 1$.

The applicability of the linear form is controversial since deviations are often reported. Using ab initio density functional simulations (DFT), Bernardini et al.[39] showed that for AlInN, the spontaneous polarization and thus the macroscopic polarization exhibits a large deviation from linearity. The deviation is taken into account by the introduction of a non-linear term to the Vegard's law. This macroscopic deviation has been attributed to the microscopic hydrostatic stress and internal strain due to chemical ordering[39,40]. Thus for the spontaneous polarization (1.13), the above authors proposed:

$$p^{sp}(x) = xp_{\alpha}^{sp} + (1-x)p_{\beta}^{sp} + b_{sp,\alpha\beta}x(1-x) \qquad 1.15$$

Where $b_{sp,\alpha\beta}$ is the deviation from linearity and it is also called "bowing parameter", for the ternary alloys (AlInN, InGaN and AlGaN), they calculated 0.071 C/m^2 0.037 C/m^2 and 0.019 C/m^2 respectively [39]. On the same basis, equation (1.14) becomes for a quaternary alloy [38]:

$$p^{sp}(x,y,z) = xp_{\alpha}^{sp} + yp_{\beta}^{sp} + zp_{\delta}^{sp} + b_{sp,\alpha\delta}x(1-x) + b_{sp,\beta\delta}y(1-y) + xy(b_{sp,\alpha\beta} - b_{sp,\alpha\delta} - b_{sp,\beta\delta}) \qquad 1.16$$

In 2003, Voznyy et al.[40] calculated the bandgap bowing energies for III-N ternaries using pseudo-potential simulations; they reported that AlInN has the largest value of 3.62 eV in comparison to AlGaN and InGaN (0.3 eV and 1.89 eV, respectively). Later that year, Dridi et al.[41] reported similar values for InGaN and AlGaN but for AlInN their calculation based on DFT leads to reevaluating it at 4.09 eV. In 2006, Terashima et al.[42] reported that the bandgap bowing might approach 4.96±0,28 eV. As also suggested by Gorczyca and coworkers[43–45] between 2009 and 2011, the higher values of this bowing are characteristic of indium-containing alloys. They suggest a quadratic compositional dependence of the bandgap bowing for both ternary AlInN and then quaternary AlGaInN alloys that takes into account indium clustering. In this instance, a uniform alloy AlInN has its bowing parameter from 2.1 eV to 6.2 eV (4.4 eV for 50% indium content) whereas the model taking into account the indium clustering AlInN has its bowing parameter ranging from 3.9 eV to 14 eV (8.6 eV for 50% indium content).

Regarding the lattice parameters “a” and “c”, Darakchieva et al.[46] reported, using ab initio calculations, that both (a,c)-lattice parameters exhibit a deviation from the linear form and proposed the following bowing parameters: $b_a = 0.0412 \pm 0.0039$ Å and $b_c = -0.060 \pm 0.010$ Å. Subsequently, the same group [47] reported that using the above parameters, one may have consistency between x-ray diffraction (XRD) and Rutherford back scattering (RBS) experiments. However, they have pointed out that a perfect agreement might not be achieved due to non-random distribution of indium atoms, the possible contamination with gallium atoms (up to 2%) or to the presence of defects.

Therefore, the physical properties of InN are still under constant discussion in the field. In fact, from 1994 to 2017, the in-plane lattice parameter “n” of this binary went from 3.548 Å[32] to 3.544 Å[1]. However, in 2002, Davydov et al.[48] reported that a_{InN}= 3.5365 Å from X-ray analysis. Later, in 2006, GaN et al.[49] optimized from first principal calculation the a-lattice parameter of InN around 3.518 Å. Considering the ternary alloy, while using the lattice parameters of the binary compounds provided in ref.[1] and by applying Vegard’s law without deviation, the lattice match of $Al_{1-x}In_xN$/GaN is for 18% of indium content. Furthermore, if the deviation from Vegard’s law is taken into account as suggested by Darakchieva et al.[46], then a lattice parameter of 3.189 Å (a-GaN) is obtained at 19.5% of indium content. Moreover, for the quaternary alloy, the solution can be obtained by any triplet (x, y, z) satisfying the unmodified equation 1.14. Thus, for both ternary and quaternary alloys, the determination of a physical property depends on the knowledge we have on the properties of the end binary compounds.

1.5. Structural defects in III-Nitrides

Crystalline materials exhibit mostly point, line and planar defects[50]. The efficiency of devices is critically dependent on the density of these defects which can be present in the processed material needed for their fabrication. It is therefore important to study them in order to understand their structure, chemistry and formation mechanisms, and eventually help to grow better quality materials for optimized devices performance.

1.5.1. Point defects

In a perfect crystal, atoms occupy specific crystallographic sites, however, due to many reasons; a number of such sites may not be occupied, which gives rise to vacancies. The atoms can also be located out of these specific sites, thus becoming interstitial impurities. Moreover, the purity of materials is never 100%, foreign impurities are incorporated during the synthesis, and such foreign impurities may occupy the specific atomic sites of the material, in which case they are called substitutional impurities, or be located at interstitial sites. Kim et al.[51] carried out the growth of Si-doped GaN. The authors correlated the concentrations of silicon and oxygen impurities while increasing the ammonia flow rate; they reported a decrease in the Hall mobility when the impurities concentration is increased. Similarly, Fang et al.[52] reported an increase in nitrogen vacancies in Si-doped GaN grown by reactive molecular beam epitaxy (r-MBE) when the temperature is lower than 800 °C. Thus the concentration of impurities may lead to a change in the doping and/or the mobility of the carriers. In contrast, Li et al. [53] by density functional theory (DFT) showed that gallium interstitial might enhance the yellow luminescence which is an impurity level often present in photoluminescence spectra of GaN films.

1.5.2. Dislocations

Dislocations are line defects in crystals that are characterized by a line direction (l) and a displacement vector known as the Burgers vector induced inside the crystal along the line. When the Burgers vector is a linear combination of lattice vectors the dislocation is called entire, and when it corresponds to a fraction of a lattice parameter, the dislocation is said to be partial[54]. As the dislocation is completely defined by its line ($\vec{u}$) and Burgers vector ($\vec{b}$), the geometrical relationship between the two vectors determines the type of the dislocation. The dislocation is of screw or edge type when $\vec{u}$ and $\vec{b}$ are parallel or perpendicular, respectively, otherwise, it is of mixed type. Figure 1.4 shows the two types of dislocations, in a cubic symmetry material.

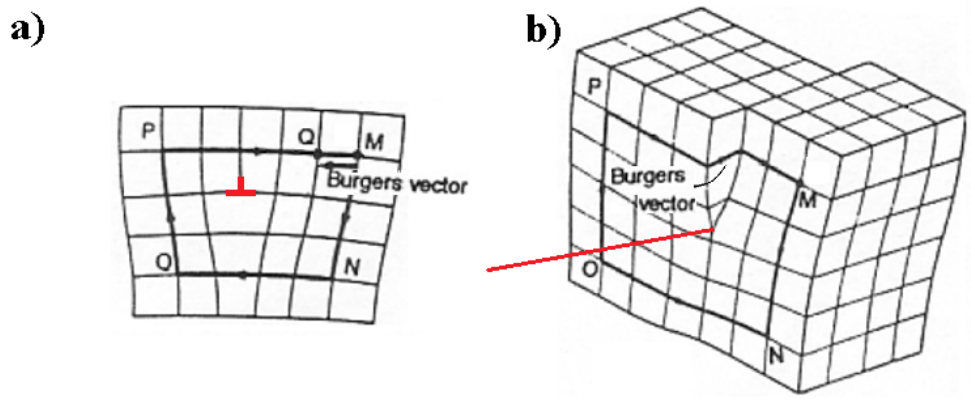

Figure 1.4: a) Representation of an edge dislocation. The red inverted T-shape shows that the dislocation line is out of the plane (MNOP) and is perpendicular to its Burgers vector b) Representation of a screw type dislocation in a 3D view. The red line shows that the dislocation line and its Burgers vector are parallel[55].

An edge dislocation can be formed by inserting a half-plane in the crystal. The dislocation line position is at the end of this additional plane as shown in figure 1.4a by an inverted red "T" and its Burgers vector is orthogonal to the dislocation line. A screw dislocation can be generated by pushing half of the crystal along a particular line by an amount of the lattice parameter as depicted in figure 1.3b. In this case, the dislocation line (shown with a red line) and the Burgers vector are parallel. A general dislocation of mixed type has an edge and a screw component.

In the hexagonal lattice, as encountered in nitride materials, a perfect dislocation can have "$\vec{a}$", "$\vec{c}$" and "$\vec{a}$+$\vec{c}$" as possible Burgers vectors. As an example, let's consider the $\vec{a}$ dislocation, if its line is located in the basal plane, it can be of edge or mixed type. When the line is along [0001], it is of edge type. In that case, it propagates from the interface of epitaxially grown layers towards the layer surface and it is referred to as $\vec{a}$ threading dislocation (TD). In the same geometry, the $\vec{c}$ dislocation is of screw type and $\vec{a}$+$\vec{c}$ type is a TD of mixed type. Table 3 summarizes common dislocations and their Burgers vectors. The partial dislocation in the $\frac{1}{3}[10\bar{1}0]$ is called the Shockley partial and note as "p".

Dislocation character	Symbol	Burgers vector
perfect	**a**	$\frac{1}{3}[11\bar{2}0]$
perfect	**a**	[0001]
perfect	**a+c**	$\frac{1}{3}[11\bar{2}3]$
Partial (Shockley)	p	$\frac{1}{3}[10\bar{1}0]$
Partial (Frank)	**c**/2	$\frac{1}{2}[0001]$
Partial (Frank-Shockley)	p+**c**/2	$\frac{1}{6}[20\bar{2}3]$

Table 1.3: Dislocations and their burgers vectors in the close-packed hexagonal system with Miller-Bravais notation

The impacts of dislocations on devices are various. For instance, Jena et al. [56] showed theoretically that the mobility of the 2DEG in a HEMT structures such as AlGaN/GaN can be strongly decreased with increasing the dislocation density. In this instance, Kotani et al.[57] observed a reduction by up to four orders of magnitude of the leakage current measured at the gate Schottky contact of an AlInN/AlN/GaN HEMT whenever the dislocation density is decreased from 1.8×10^{4} cm^{-2} to 1.2×10^{9} cm^{-2}.

1.5.3. Planar defects

A planar defect is present when the crystal periodicity is interrupted along a well-defined plane through a displacement (translation) or a more complex combination of group symmetry operations. Planar defects can be stacking faults (SF), inversion domains boundaries (IDB) and grain boundaries (GB). They are described by the interrupted symmetry operation that connects the two sides of the crystal limited by the boundary.

Stacking Faults

Focusing on the wurtzite lattice, the SFs are classified into three types: intrinsic I_1, intrinsic I_2 and extrinsic E. In terms of formation energy, it increases in the presented order[58]. These two-dimensional defects can be represented as quantum wells leading to radiative recombination of excitons in GaN[59]. Therefore they can be characterized by luminescence spectroscopy. Furthermore, these defects can change the local stacking from wurtzite to zinc-blende which is the case of I_1 leading to a modification of the local polarization and thus affects the carrier density[60]. I_1 can be obtained by the introduction of a zinc-blende row stacking in the wurtzite sequence

along [0001]. In terms of crystal symmetry, it is obtained by removing one plane (basal plane) and then applying a shear by $\frac{1}{3}[10\bar{1}0]$ thus the final displacement vector is $\frac{1}{6}[20\bar{2}3]$. For instance along [0001] and for a $[11\bar{2}0]$ projection, the stacking is modified from …AaBbAaBbAaBb… to …AaBbAaCcAaCc… I_1 is not obtained from dissociation of dislocations, thus, this defect is a growth defect. I_2 can result from a shear in the basal plane that introduces two rows of zinc-blende or the dissociation of an "a" type dislocation into two partial Shockley dislocations thus the fault vector is $\frac{1}{3}[10\bar{1}0]$. The new stacking is then …AaBbAaBbCaAaCaAa…. E fault is obtained by the addition of a plane in the cubic position in the hexagonal stacking. Therefore, the stacking becomes …AaBbAaBbCcAaBbAaBa… and has a fault vector of $\frac{1}{2}[0001]$.

Inversion domains

A real crystal may be formed by a number of more or less disoriented grains separated by boundaries. The junction between the single crystals is called a grain boundary and the two sides of a boundary can be related by different symmetry operations such as rotation, inversion or mirror[61]. In non-centrosymmetric materials, such as the wurtzite III-Nitrides, a particular planar defect can be an inversion domain (ID) boundary (IDB), when the two sides of the crystal are related to the inversion operation which can be pure or combined with a translation.

2 Characterization techniques

This chapter describes the main characterization techniques used in this investigation of AlInN and AlGaInN layers. The first observations of all the samples were systematically carried out with atomic force microscopy (AFM). In parallel, specimens were prepared for transmission electron microscopy either by mechanical polishing or when necessary by focused ion beam (FIB). Scanning electron microscopy (SEM) observations were also made in the FIB facility. Therefore specific sites and defects identified by AFM were extracted for TEM analysis. Atom Probe Tomography (APT) was also performed.

2.1. Atomic force microscopy

Subsequent to the invention of scanning tunneling microscope (STM) by Binning and Rohrer (Nobel Prize 1983)[62]the AFM which uses forces instead of the electric tunneled signal came up to permit the investigation of non-metallic surfaces.

In the AFM, a sharp probe is attached to an oscillating cantilever. The end radius of the probe is typically between 5 nm and 15 nm. When, the probe is approached to the surface of the sample an interaction force appears, this force depends on the distance between the tip and the material surface properties.

There are three different modes in AFM. If the tip is in contact with the surface of the material, then it is operating in a repulsive regime and corresponds to a Coulomb interaction. When the tip is few nanometers far from the surface, the probe goes in an attractive regime toward the surface. In this case, a Van Der Waals interaction is observed. For the characterization of our layers, we have used the third mode which is called tapping mode. In this semi-contact mode, the cantilever is firstly set to oscillate at its free resonance frequency when the cantilever is far from the sample surface. During the approach of the oscillating cantilever towards the surface, the free amplitude decreases near the surface. Therefore, an amplitude setpoint is chosen (which is usually ~70% of the free oscillation amplitude) to define the strength of interaction between tip and sample. Under this operating condition, the topography is obtained. Figure 2.1 shows the force-distance dependence curve.

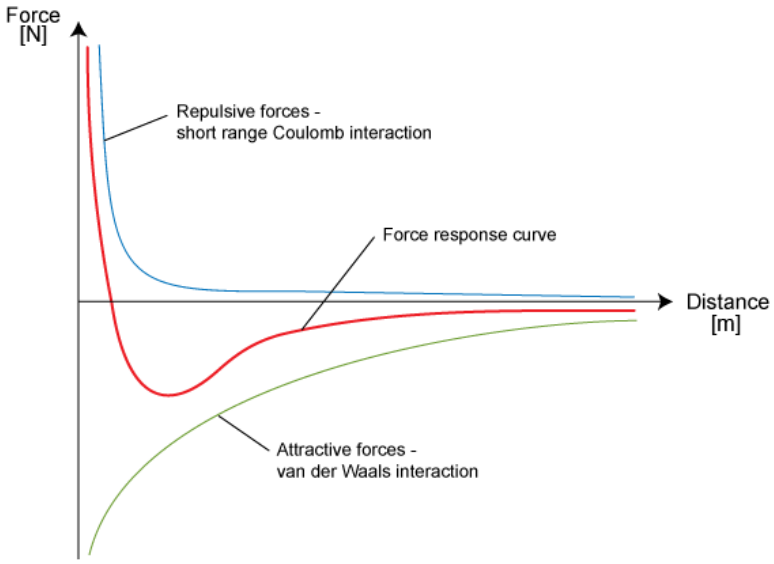

Figure 2.1: Force-distance curve dependence. In a repulsive regime, the tip is in contact with the surface. If the tip is few nanometers away from the surface Van Der Waals interaction is felt[63].

In the AFM, piezo-ceramics are controlling the fixed amplitude set point which is used as a feedback for the z-displacements. The scanning can be performed by either moving the tip or the sample with respect to each other. Any variation of the interaction force between the tip and the surface from the set point (constant amplitude) will be detected by a laser beam. This laser points to the edge of the cantilever and is reflected back to a photodiode. The plot of the laser deflection versus the position on the surface gives the topography of the probed region. From this height image, the standard deviation of the amplitude gives the average roughness of the surface.

2.2. Electron microscopy

Transmission Electron microscopy (TEM) and scanning electron microscopy (SEM) were used to investigate the specimen properties from different aspects.

2.2.1. Scanning electron microscopy

The SEM is a characterization technique that provides information on surface state, morphology, and orientation maps can be obtained by Electron Backscattered Diffraction (EBSD). The composition is measured by energy dispersive spectroscopy (EDS). In this work, we used the dual beam FEI Nanolab (SEM/FIB) for the SEM observations and mainly for specimen preparation.

2.2.2. Transmission electron microscopy

Transmission electron microscopy[64] offers a broad range of observations and analysis techniques. During this thesis, TEM was extensively used as the main characterization technique. The samples investigated in this work were prepared as cross sections and plan views. In such instruments, one can reach the atomic resolution in imaging and chemical analysis. Therefore it is possible to determine with a high accuracy the composition of a given sample, its crystallographic properties, and defects in the observed areas….

The transmission electron microscope is composed of an electron source operating at few tens to hundreds of keV. This cathode is often called a filament; it can operate at high temperature, or without heating for more coherence. Along the path of the electrons, electromagnetic lenses provide the investigator different imaging and diffraction modes for the analysis of the samples which need to be transparent to these energetic electrons. In the TEM, several diaphragms are there to select either a zone of interest or for shaping the electron beam. Diaphragms are placed in different *eigen* plans. The images and diffraction patterns are obtained in specific planes along the instrument column, they reflect the interaction of the high energy electron beam with the material under investigation.

Three JEOL TEMs have been used in this work all operating at 200 keV: 1) The JEOL-2010 conventional TEM with a stage that allows sample tilting up to +- 40° was used to investigate the microstructure of our materials using diffraction contrasts. In this microscope, the electron source is a thermionic LaB_6 crystal. 2) The second instrument is a JEOL 2010 equipped with a Field Emission Gun (FEG). This microscope was mainly used in scanning mode (STEM). In the annular dark field (ADF) mode, using small camera lengths, it allows Z-contrast images of our heterostructures, although due to the optical quality of this instrument, atomic resolution cannot be attained. Most of the EDS analysis was carried out on this instrument in STEM mode. For improved spatial and spectrometric resolution, we also had access to the ARM 200 in Caen.

Due to the limited access to the ARM in Caen, a number of experiments were also carried out either on the FEI TITAN operating at 300 keV at the Institute of Solid State

Physics, BREMEN, Germany, as well as at the Institute of Physics Warsaw, and on the ARM 200CF of the Max Planck Institute, STUTTGART, Germany.

2.2.3. Electron sources and electron guns

The electron sources (the cathode) can be classified into two types: thermionic and field effect sources. Tungsten (W) and LaB_6 crystals are usually used as electron sources.

a- Thermionic sources

Heating materials such as tungsten and LaB_6 can give to the electrons enough energy to leak from the surface of the considered crystal source. In a microscope, the gun is maintained under vacuum and at an accelerating voltage so that the extracted electron can travel to the sample at the set energy.

The extraction energy "Φ [eV]" is known as the work function of the material from which the electrons are extracted. Richardson's law gives a good approximation of the electron emission theory. The following equation gives the relationship between the current density "J [$A.m^{-2}$]" to the operating temperature "T [K]":

$$J = AT^2 e^{-\frac{\Phi}{kT}} \qquad 2.1$$

Where "k = 8.6×10^{-5} $eV.K^{-1}$" is Boltzmann constant and "A [$A.m^{-2}.K^{-2}$]" is Richardson's constant and depend on the used source. Formally speaking, in order to obtain a current density, one has to achieve the following condition: kT > Φ. The source can be tungsten (filament) for its high melting point around 3400 °C. In practice, LaB_6 (crystal) which has a lower extraction work function around 2.4 eV in comparison to tungsten (4.5 eV) with a tip radius less than 1 µm results in a higher current density and a brightness 10 times stronger than for tungsten. For this smaller source size, a more coherent beam is formed along with less scattered electron energy dispersion (1 eV – 1.5 eV). Therefore LaB_6 filaments are employed as thermionic sources. Figure 2.2 is a schematic representation of a thermionic source.

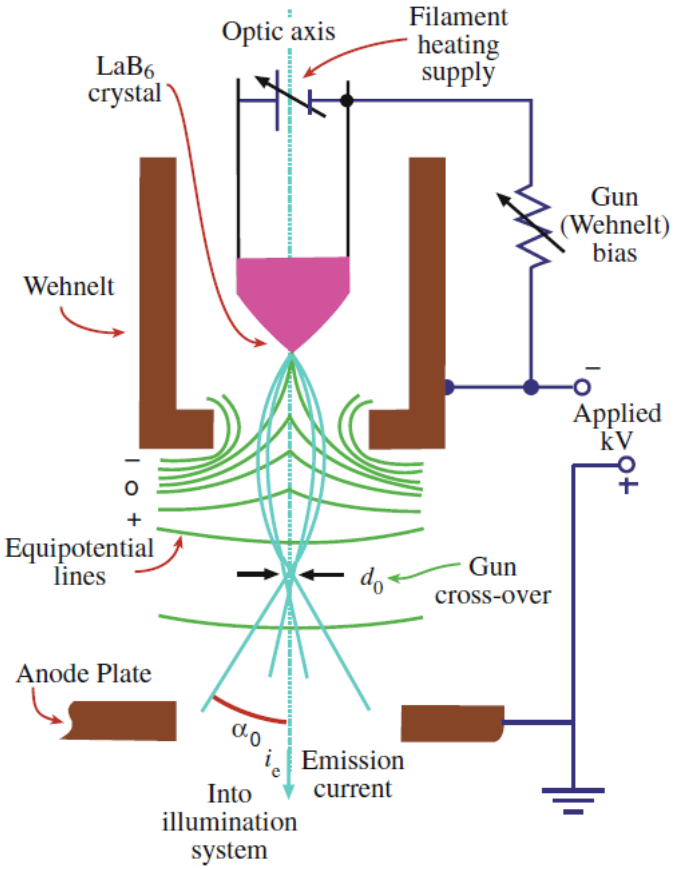

Figure 2.2: Schematic diagram of a thermionic electron gun. A high voltage is applied between the cathode and the anode. The Wehnelt is the first electrostatic lens that the electrons go through in the TEM. Its electric field focuses the electrons into a crossover "d0" with a convergence/divergence angle α0 which is the true source (object) for the lenses in the TEM illumination system[64].

b- Field effect sources

A field effect gun (FEG) emission is governed by the electron tunneling theory. In this instance, a monocrystalline material is shaped as a tip and is submitted to a high extraction potential and is under vacuum. At the apex of the tip, electrons can tunnel out following the equation (2.1):

$$E = \frac{V}{r} \qquad 2.2$$

Here "r" is the tip radius. For instance, if r = 100 nm then E= 10^{10} V/m, (for an applied voltage of 1kV). In contrast to a thermionic emission where the temperature plays an important role, in the case of the field emission the vacuum needs to be very low (10^{-10}-10^{-11} Torr) to avoid tip contamination and allow the electrons to tunnel out. Two methods are currently used in modern FEG TEMs 1) the extraction at room temperature; this type of source is called cold FEG and offers a highly coherent beam.

In such guns, the emission undergoes a slow decrease during the working time mainly due to pollution, it needs to be cleaned at intervals by submitting it to short heating times (flashing the source at several thousand of Kelvin) this is the case of the ARM. 2) For highest stability, the filament can be operated at high temperature. In this instance, the W tip is protected by a ZrO layer and continuously maintained at around 2000 °C. Therefore, the coherency of JEOL 2010 FEG is lower than for the ARM because even at a small tip, the temperature cannot be uniform, which leads to the emission of electrons with different energies. Figure 2.3 shows an example of a FEG W tip.

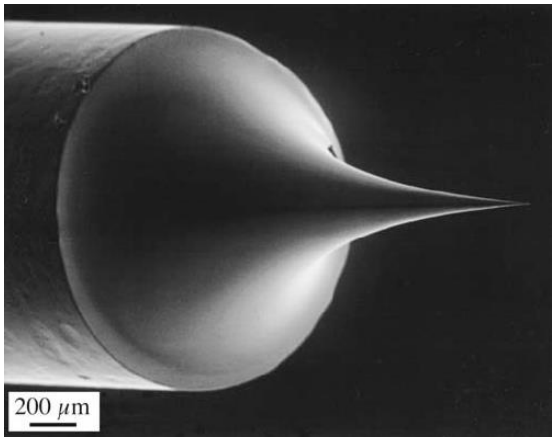

Figure 2.3: The W monocrystalline tip-shaped filament of a FEG[64].

c- Electron sources and applications

In comparison to a thermionic source, the current density of a FEG is at least 1000 times higher and provides an energy spread of the electron beam less than 1 eV at an acceleration voltage of 100 kV. Therefore a more coherent beam is obtained in a FEG. Thus a FEG is a more suitable solution for applications such as high-resolution TEM (HRTEM) or electron energy loss spectroscopy (EELS). Furthermore, the small source size and the high brightness of a FEG make it also a good choice for energy dispersive spectroscopy (EDS). On the other hand, the size of the source in a FEG makes it not suitable for routine imaging in TEM at low magnification. In comparison, a thermionic source is, indeed a bigger source and less coherent with a slightly lower brightness this can provide better images at lower magnifications without losing current density while looking at large areas. Therefore conventional investigations were preferably done on the JEOL 2010 (thermionic) whereas EDS measurements were made on both FEG sources and the HRTEM on the JEOL ARM.

2.2.3.1. Lenses, resolution

a- Controlling the electron beam

From the gun, the electrons flow through the column of the microscope which is kept under vacuum. Similarly to an optical microscope, lenses are placed along the path of the electrons. Inside the TEM column, there are three main functional parts: 1) the illumination system formed by the condenser lenses that shape the beam at the exit of the gun. 2) The objective lens constitutes the imaging system and 3) the projector lenses which can be used to project the back focal plane of the objective lens or the image plane to obtain either a diffraction pattern or an image of the sample.

In the following, we will describe briefly the objective lens which is a fundamental part of the imaging system. The objective lens is formed by a cylindrically symmetric magnetic open core where the electrons travel through. This forms the pole piece and usually, they are two and conically shaped. The two pole pieces are placed head-to-head. The diameter of the hole is typically around 3 mm letting the electron beam flow through. The outer part of the lens is surrounded by a copper coil wire that includes both pole pieces. The specimen is placed in the gap between the pole pieces. Figure 2.4 shows a cross-section of a magnetic lens.

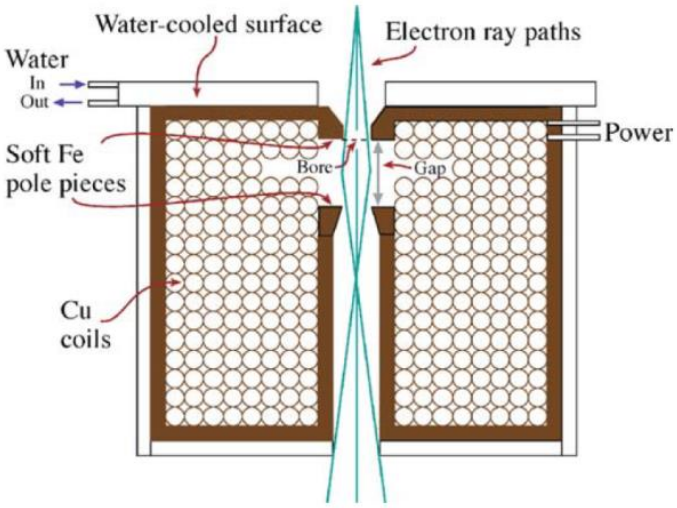

Figure 2.4: Cross-section view of a magnetic lens[64].

b- Resolution

In microscopy, the resolution is the ability to separate two closely spaced dots. The theoretical resolution can be approximated by the Rayleigh condition (2.3):

$$r_{th} = 1.22\frac{\lambda}{\beta} \qquad 2.3$$

Where λ is the wavelength of the electrons and β is the semi-angle collection of the objective lens.

In practice, several aberrations are present and they limit the performance of a microscope, they are the spherical and chromatic aberrations and astigmatism of the lenses.

The astigmatism is the most standard and easily corrected aberration, it is the fact that the magnetic field of the electromagnetic lens is never symmetric, therefore the focus in two perpendicular directions is never at the same point. The correction of astigmatism is made with "stigmators" which are additional lenses placed at the exit of the gun at the condenser lens and at the objective lens to compensate this X/Y systematic difference in focus.

The spherical aberration occurs in the objective lens when the beams away from the "optical" axis (off-axis) feel stronger magnetic field and thus they are focused at different points. The spherical of the objective lens corresponds to the deformation of the wavefront at the exit of the lens as can be seen in figure 2.5. Due to this aberration, the image of a point is a disk known as the disk of confusion where the intensity decreases radially. The size of the disk is a function of "C_s [mm]" which is called the spherical aberration coefficient of the lens. Therefore, this constitutes an important limitation for the resolving power in the TEM and defines the optical quality of each lens and it cannot be directly corrected by manipulating the magnetic field of an individual lens. In a "C_s" corrected microscope a highly complex structure of lenses is used to reshape the beam just after the condenser (probe corrector) or the objective lens (image corrector).

The other important aberration is due to the fact that electrons of different energies will travel at different velocities and imaged at different positions (C_c: chromatic aberration). Even if the energy spread in the recent sources is quite small ~ 0.3-0.4 eV for cold FEG, it is still too high for most accurate analytical or diffraction investigations. For such work, additional systems of lenses need to be attached at the exit of the gun (monochromators) and for the latest instruments, it is claimed that

energy dispersion close to 10 meV can be obtained, which should allow investigations for instance of impurities inside band gaps, or other fine interactions such as phonons.

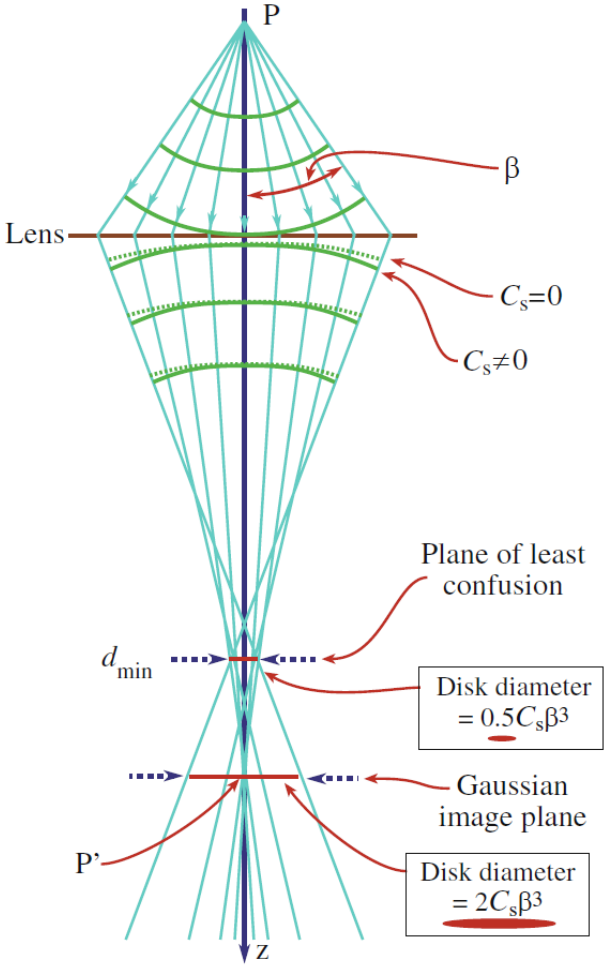

Figure 2.5: Schematic illustration of the effect of the spherical aberration and its effect on the electron wavefront at the exit of the objective lens[64].

2.2.3.2. Imaging in a TEM

One way to classify the imaging possibilities in a TEM is by the shape of the probe that reaches the specimen. The specimen is placed in the object plane of the objective lens in the gap situated between the pole pieces. The two possibilities are a parallel beam or a convergent probe.

By adjusting the intermediate lenses, one can project on the viewing screen or the digital camera either the back focal plane of the objective lens to see the diffraction pattern or the image plane to have an image the specimen.

A parallel beam is used for diffraction contrast images to produce bright and dark field images; "BF" and "DF". This is the TEM mode used for the investigation of defects in materials from the micro down to a few nanometers. The convergent beam mode is used in STEM configuration, convergent beam electron diffraction (CBED), X-ray energy dispersive spectroscopy analysis (EDS), where highly focused beams are needed for analysis of small areas.

Operating TEM with parallel beam

The interaction of the electron beam with a crystalline specimen can be described with Bragg's law. Due to the small scattering angle: "θ", one can write out:

$$2.d_{hkl}.\theta = \lambda \qquad 2.4$$

Here "d_{hkl}" is the spacing of the lattice planes and λ is the wavelength of the incident beam.

a- Bright field and dark field imaging

In the Fourier plane (back focal plane) the diffraction pattern is obtained from the entire specimen under the beam which is not usually the final purpose, thus we select a region to contribute to the diffraction pattern. In the microscope, this is done by introducing an aperture in the image plane of the objective lens. Then a selected area electron diffraction pattern (SAEDP) is obtained. This aperture acts like a virtual diaphragm in the object plane.

In contrast to X-rays where Bragg angles are large (a few tens of degrees), the electron wavelengths in the TEM are quite small (~pm), and the Bragg angles are of the order of 10 mrad, many families of planes can satisfy Bragg's law at the same time. With a parallel beam, the SAEDP is an array of spots. The central spot corresponds to the transmitted beam which is not diffracted. All other spots come from diffused beams by lattice plans satisfying the Bragg law. Using an objective aperture in the back focal plane, either the transmitted beam or a diffracted beam can be selected to form either a bright field image or dark field image. Figure 2.6 shows schematically this procedure. In a dark field image, the result is obtained from only the scattered electrons from the specimen, so the vacuum will appear dark.

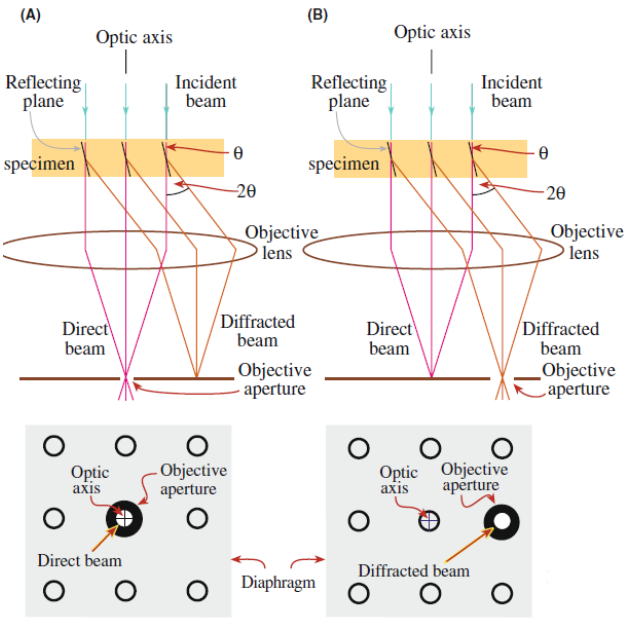

Figure 2.6: Ray diagram showing schematically the procedure to obtain a) a BF image with the transmitted beam and b) a DF image if a diffracted beam is selected with the adequate objective aperture in the back focal plane of the objective lens[64].

b- Weak beam and 2 beams conditions

As mentioned above, due to the diffraction geometry in the TEM and sample thickness, it is difficult to have only two beams in a pattern. Then for investing the defects, one can use a defined family of atomic lattice planes which appear in the diffraction as a systematic row of spots (see figure 2.7). From there, one defines strong and weak beam diffraction conditions. Indeed, when the sample is oriented so that –g and +g exhibit the same intensity, we have strong beam conditions. By selecting either of the two (+ or –g) for the image formation, we have high contrast, but, for instance, the details of a defect are not well resolved because in such image the strain around the defects is highly underlined. In order to improve the resolution of defects in such images, it is necessary to tilt the sample away from the strong beam conditions. In the textbooks on TEM[64], it can be seen that this is governed by the quantity known as “s” the excitation error. This vector is defined as the deviation from the Bragg diffraction. In practice, it can be monitored by the intersection between the Ewald sphere and the considered nod of the reciprocal space. For instance, it is empirically known that a good contrast in dark field images is obtained

for defects for characteristic g, in the conditions of (–g/+3g) meaning that –g is used for image formation, and +3g is set in Bragg position.

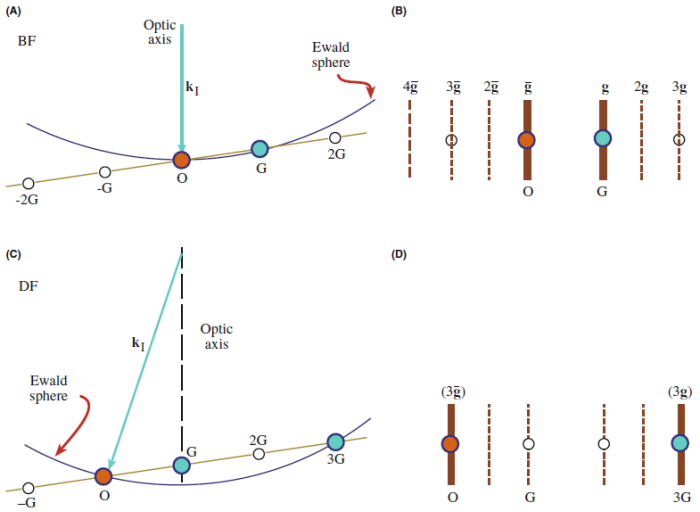

Figure 2.7: a) and b) corresponds to the 0(g) condition between the Ewald sphere and Kikuchi lines and c) and d) the g (3g) condition by tilting the beam[64].

c- Extracted information

From diffraction contrast images, information related to the crystalline quality can be obtained. For instance, in a polycrystalline specimen, the image can display moiré fringes. These result from the interaction of the electron beam with at least two superimposed monocrystals of the layer. They can be of parallel type if the superimposed crystals have only different spacing. They can be of twist type if a rotation is introduced between the lattices. The third type is a combination of the two previous. Furthermore, defects such as stacking faults can be observed under zone axis <10-10> for wurtzite crystals as well as IDBs. Moreover, in III-Nitrides, dislocations can be observed and their types identified. For this, diffraction contrast images can be used to investigate the Burgers vector "**b**" namely by using the invisibility criterion "**g.b= 0**" when the dislocations are out of contrast[65]. As an example, TDs have their line along [0001] direction. If the Burgers vector is [0001], 1/3 $[11\bar{2}0]$ or 1/3 $[11\bar{2}3]$, then the dislocation is of type screw, edge or mixed, respectively.

The following table 2.1 shows the visibility conditions for perfect dislocations in the wurtzite structure.

	g=0001	g=11-20	g=10-10
b = 1/3 [11-20]	Invisible	Visible	Visible
b = [0001]	Visible	Invisible	Invisible
b = 1/3 [11-23]	Visible	Visible	Visible

*Table 2.1: **g.b** for perfect dislocations in wurtzite structure.*

Operating TEM in convergent beam modes

In numerous cases, investigation of materials needs to access very small areas which are prone to exhibit highest crystalline quality and chemical composition and it is not anymore possible to use the parallel beam whose diameter at the sample can reach more than one µm. The solution lies in the use of specific lenses to drastically decrease the size of the electron beam. When the beam size is thus drastically decreased, it is highly convergent and the resulting diffraction pattern from a crystalline material does not exhibit spots anymore but disks whose diameter depends on the convergence angle of the probe.

***a-* CBED**

In particular, convergent beam investigation in the TEM allows accessing important crystallographic information. The wurtzite GaN crystal is non-centrosymmetric; one can assess the polarity and determine the specimen thickness at a specific region of interest.

In our case, the use of patterns along $< 10\bar{1}0 >$ zone axis is used for investigating the polarity of the layers. Moreover, the number of fringes that progressively appear in the central disk (000) allows measuring the local specimen thickness.

Indeed much work has been done in resolving the structure of crystals using CBED at higher order Laue zone (HOLZ), in combination with the zero Laue zone patterns [66]. A complete analysis of the CBED patterns in a few zone axes should be used to identify the space group of a crystal. Figure 2.8 compares the diffraction patterns for a parallel illumination and for a convergent electron beam.

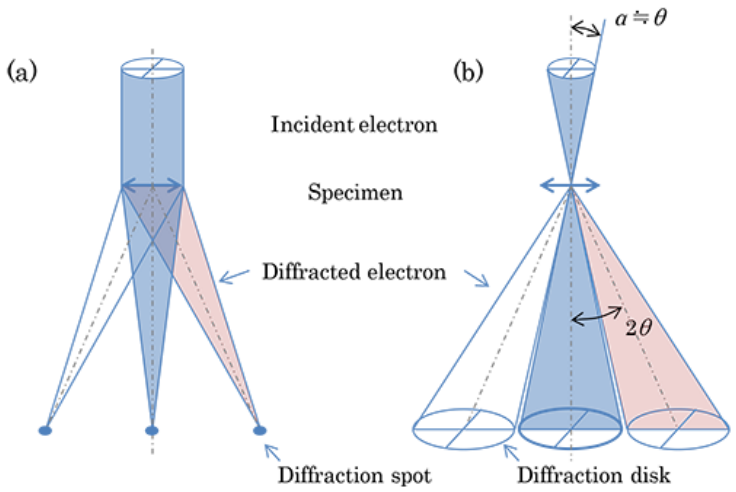

Figure 2.8: Comparison between a parallel illumination and a convergent beam resulting in diffraction disks of a CBED pattern[67].

***b*- (HR)STEM**

With the advances in corrections of the spherical aberration, it is possible to reach the atomic resolution at the highest spatial resolution thanks to small probe sizes. In a STEM, a convergent beam in the form of a probe is scanning on the specimen. The interaction between the incident electrons and the specimen atoms produces many signals, electrons, X-rays, up to visible wavelength and beyond.

The imaging system comprises annular dark and bright field (ADF/ABF) detectors collecting the transmitted electrons. Projectors are used to change the distance between the specimen and the detectors and thus the collection angle which is related to the camera length. Typically, an ADF detector has a detection range around 22 mrad and 100 mrad outside the illumination cone of the probe. Above 100 mrad it is called high angle annular dark field (HAADF). The ABF has a detection angle from around 11 mrad and 22 mrad and is within the illumination cone of the electron focused beam.

The scattered electrons in the range of an ADF detector are formed through inelastic diffusion and thus are incoherent. The use of a small camera length helps further remove any residual diffraction contrast from Bragg reflections. The contrast in ADF images is related to the chemical composition of the specimen, it is often termed as **Z**-contrast. The collected intensity can be approximated by an exponential function of the form Z^{α} ($\alpha < 2$) where Z is the atomic number of the considered atom. The heavier the atoms, the brighter contrast will be for the corresponding atomic

column. At lower magnifications, regions of phase separation can be assessed as changes in the local contrast. By contrast, using higher camera lengths allows to collect electrons from lower angles on the ADF detector, a strain contrast will be observed and it becomes possible to image at defects through their strain fields[68]. The ABF collects electrons scattered at lower angles, thus light elements such as nitrogen atomic columns can be observed which interacts weakly with the electron beam and have a weak atomic scattering.

***c*- (HR)STEM- Analytical EDS**

The EDS detector is placed above the sample and collects the emitted characteristic X-rays from the interaction of the high energy electrons with the atoms of the material under investigation. For accurate measurement, EDS is carried out during STEM-ADF at high magnification. In the spectrum, the atoms which are present will display the peaks corresponding to the excitation and relaxation of the electrons from their core levels (K, L…). The quantitative determination of the local composition takes into account not only the surface of the corresponding peaks but also needs to take into account the emission and detection efficiency and the experimental conditions. Some care has to be taken into account, such as geometrical factors inside the microscope; the position of the sample, the orientation of the interface[69],… For instance, probing close to the interface of GaN and Al(Ga)InN is challenging because gallium atoms are present in both the barrier and the buffer. Therefore an indication that the specimen is well oriented is for a maximum detection of aluminum and indium to minimize the contribution of the GaN buffer.

2.3. Atom probe tomography

Atom probe analysis is based on the evaporation of matter under a high electric field[70]. In order to achieve this field effect evaporation, the probe should satisfy some requirements such as the size of its apex. The radius should be then around 50 nm. In our case, for semiconductor materials, FIB was used to prepare probes from the epilayers.

The APT analysis requires ultra-high vacuum (~10^{-10} mbar) and low temperature (~50 K). The setup can be compared to the electron source of a FEG microscope where a high voltage is applied to the tip. In the APT, a high electric field is applied to

the apex of the tip. But instead of extracting electrons from the probe, atoms are evaporated from the tip material which is under investigation. The electric field takes the following form:

$$E = \frac{U}{\gamma \times r} \qquad 2.5$$

Where "E [V.m^{-1}]" is the electric field that forms at the apex of the tip, "U [V]" the bias applied to the sample, "r [m]" is the tip's radius and "γ (unitless)" a constant associated with the geometrical shape of the tip. For semiconductors, the APT is assisted with a femtosecond pulsed laser. The process is shown in the schematic of Figure 2.9.

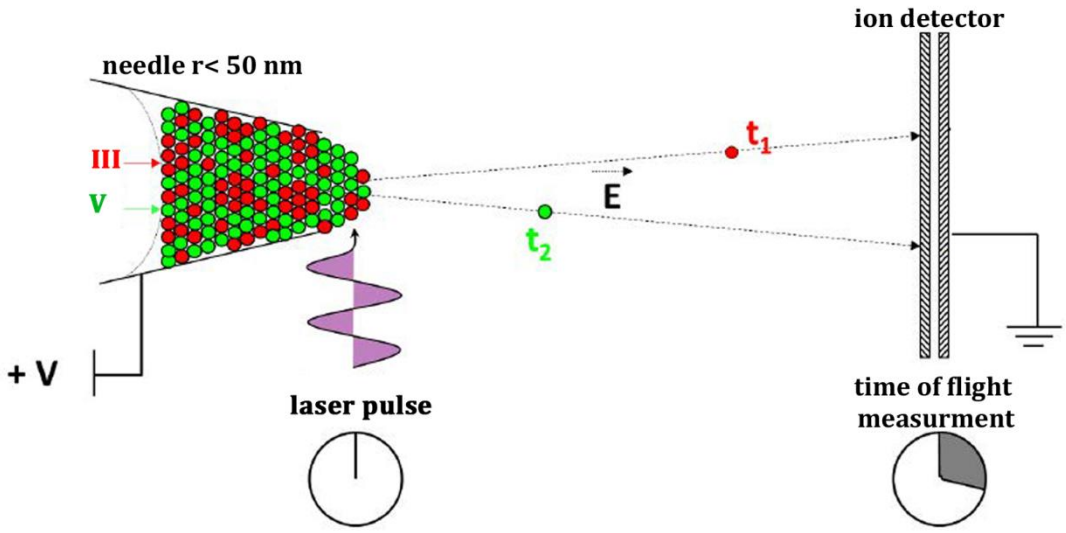

Figure 2.9: Schematic showing the principle of the APT process. With modifications from [71].

The identification of the chemical species is based on time of flight mass spectroscopy. The moment an atom leaves the probe is critical to know. In practice, the applied electric field is close to the energy required for the evaporation. Thus a laser pulse is applied to bring enough energy letting the event happening. As a result, the origin of time for each event is controlled by the laser pulse. The detector is sensitive to the place of the impact and records the electric charge of the detected ionized species. The chamber length "L [m]" is also known, so, the arrival time "Δt [s]" and coordinates.

When an atom is ionized, it acquires a potential energy as follows:

$$E_p = n \times e \times U \quad (2.6)$$

With “n” the charge state and “e” is the elemental electron charge. This energy is converted to a kinetic energy equal to; while “M [kg]” is the masse and “v [$m.s^{-1}$]” is its velocity:

$$E_c = \frac{1}{2} M v^2 \quad (2.7)$$

Thus the ratio mass/charge state can be determined as follows:

$$\frac{M}{n} = 2 \times e \times U \times \left(\frac{\Delta t}{L}\right)^2 \quad (2.8)$$

Determining this ratio and knowing the coordinates of the impact on the detector, as well as the material structure (lattice parameters, atomic position within the unit cell); one can reconstruct a 3D atomically resolved structure of the evaporated material.

3 Growth chamber history and geometry: influence on AlInN and AlGaInN

In this chapter, we present the growth technique used for the metal organic vapor phase epitaxy of (Al, Ga, In)-N layers. The growth was carried out at III-V Laboratories using two reactors 1) the Aixtron AIX200 RF and 2) the Aixtron close-coupled showerhead (CCS), which produced ternary alloys (AlInN) and quaternary alloys (AlGaInN), respectively. In the following sections, the reactors will be firstly described. Then, their geometrical and historical influence on the produced epilayers will be discussed.

3.1. Metal-organic vapor phase epitaxy (MOVPE)

Metal-organic vapor phase epitaxy (deposition)[72,73] of nitrides relies firstly on the vapor transport of metal-organic precursors via a carrier gas (H_2 and/or N_2) toward a high temperature heated substrate surface. These precursors are often trimethyl-aluminum (TMAl), trimethyl-gallium (TMGa) and trimethyl-indium (TMIn). The molecules will firstly decompose in the gas phase[74,75]. Then Group III and group V atoms will migrate at the substrate surface to contribute to the layer by layer growth[76,77], whereas the organic constituents are evacuated from the reaction area by the carrier gas which is pumped out. The atoms that are diffusing on the surface will reach an incorporation site and form new bonds and contribute to the epitaxial growth. Figure 3.1 shows a schematic diagram of the involved reactions.

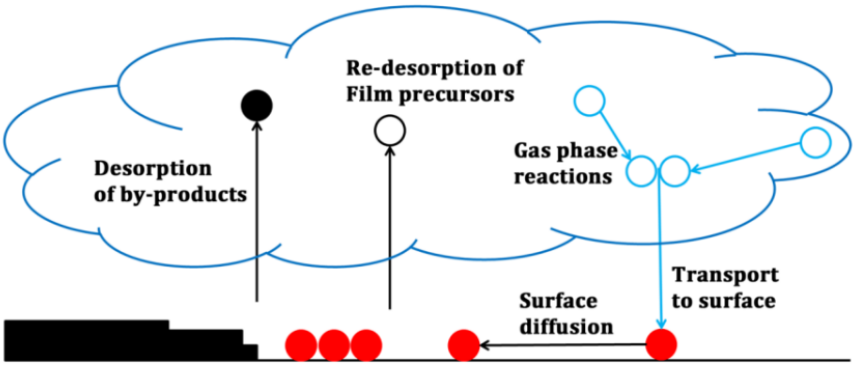

Figure 3.1: Main chemical reactions in the vapor phase during the MOVPE process

For nitride semiconductors, MOVPE has emerged as growth technique for industrial production of the light emitting diodes (LEDs) and laser diodes (LDs), in contrast to the MBE which is still dominant for conventional III-V semiconductors (GaAs based). The operating pressures go from 10^{-3} Torr to above the atmosphere which constitutes an advantage over MBE that requires ultra-high vacuum[73].

3.1.1. Aixtron AIX200 RF reactor

In this reactor, the gas flow is horizontal to the wafer holder. The chamber contains two quartz tubes. The inner tube also called the liner holds the graphite susceptor where a wafer up to 2 inches can be used**.** The outer quartz tube is water cooled. The wafer is heated through the susceptor by inductive radio frequency (RF) coils. Most of the chemical reactions would take place in the highest temperature area (around the susceptor); such a horizontal geometry may be termed as a cold wall chamber. This promotes the growth in the mass transport regime where the growth is limited by the incoming species rate and their diffusion[73]. Figure 2 shows a cross-section of the horizontal reactor. One of the main drawbacks of this configuration is the parasitic reaction that forms nanoparticles byproducts of AlN[74]. Moreover, the size up to 2 inches is a limitation for mass production.

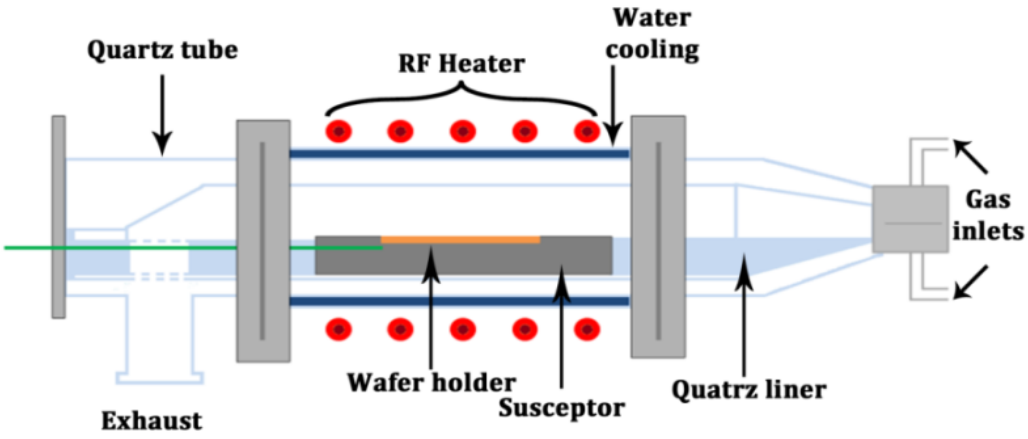

Figure 3.2: Schematic overview of the horizontal MOVPE chamber[72]

3.1.2. Aixtron close-coupled showerhead (CCS)

In this facility, the gas flow is perpendicular to the susceptor which is much larger than in the previous case and can support a larger number of substrates of different sizes: 19×2 inch, 7×3 inch, 4×4 inch, 1×6 inch. Therefore, it is suitable for mass

production. The shower head contains a high density of holes placed at around 2 cm from the susceptor. This configuration is expected to limit the parasitic reactions in the gas phase. A schematic view is shown in figure 3.2.

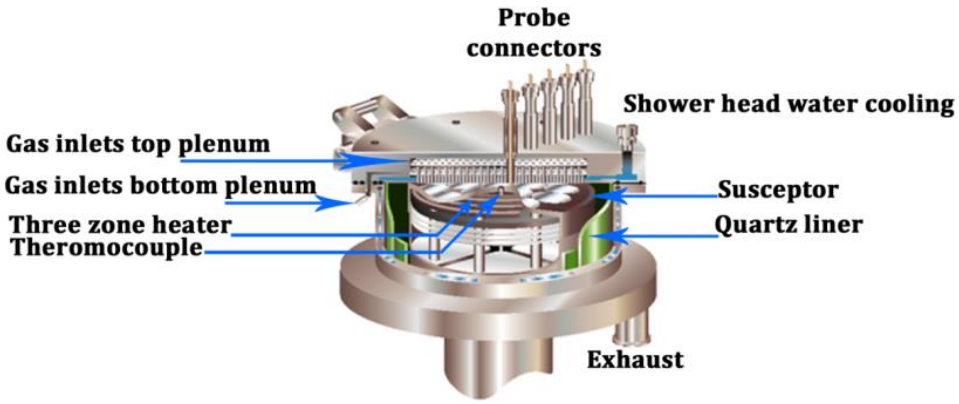

Figure 3.3: Schematic view of the close-coupled shower-head MOVPE facility[72]

As was noticed in some reports for only this geometry, the AlInN layers are found to contain several percents of gallium leading to quaternary alloys AlGaInN[26,78,79]. In the following, we assess the origin of gallium and in what extent it can be controlled with respect to the growth conditions.

3.2. Samples presentation

The samples studied in this chapter are presented in table 3.1. Sample A383 was grown in the horizontal reactor without specific cares of the growth chamber or conditioning. Whereas six samples (TS241, TS909, TS685, TS495, TS496, and TS497) were grown in the vertical chamber.

TS241 and TS909 were grown without cleaning or chamber conditioning. TS909 corresponds to a HEMT structure with a 6 nm barrier on top of which, a 13.7 nm of SiN was in-situ deposited inside the growth chamber for device passivation purposes. In this instance, the aim was to monitor the non-intentional gallium incorporation. Indeed, the presence of metallic atoms in a passivation layer is not desirable[80]. In contrast, TS685 was grown after conditioning the chamber. Samples TS495, TS496, and TS497 were grown consecutively in one run without chamber conditioning with increasing the growth pressure from 50 Torr, 80 Torr, 100 Torr, and 120 Torr, respectively.

samples	Pressure [Torr]	Temperature [°C]	Nominal barrier thickness (TEM) [nm]	Chamber design
A383	55	810	125	horizontal
TS241	50	875	100	vertical (CCS)
TS909	50		6	
TS685	50		61	
TS495	80		66	
TS496	100		60	
TS497	120		67	

Table 3.1: Samples growth parameters and corresponding chamber configuration

The stacking of all these samples is Al_2O_3/GaN/AlIn(Ga)N except for TS241 where we have 1.2 nm of AlN between the barrier and the GaN. A schematic of the heterostructure of TS909 is shown in figure 3.4.

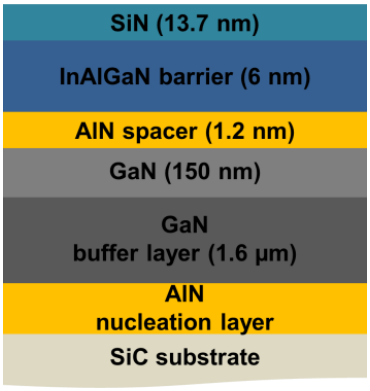

Figure 3.4: The stacking of the heterostructure of TS909

3.2.1. Investigating the origin of gallium

In the following, we assess the origin of the unintentional gallium incorporation and monitor its elimination by growth chamber conditioning.

Figure 3.5a shows the EDS results recorded on A383 at a 30 nm depth below the surface. The scans were made parallel to the AlInN/GaN interface. We did different scan lines over different depths and no significant fluctuations in the composition were observed. As can be seen, no gallium has been detected. The average indium content is 17%. This is in agreement with the nominal value as determined by XRD which gave 16%. In contrast, Figure 3.5b shows the EDS results obtained on TS241 done at four different depths. The scans were made using the same method as for A383. As can be seen, during the growth, the composition is uniform in the scanned regions. The layer contains 20% of indium and 11% of gallium. Moreover, this

composition does not depend on the depth. As a result, the aluminum content has relatively dropped by 10% in comparison to the aluminum content of A383. Therefore, it is obvious that the indium content cannot be extracted from XRD.

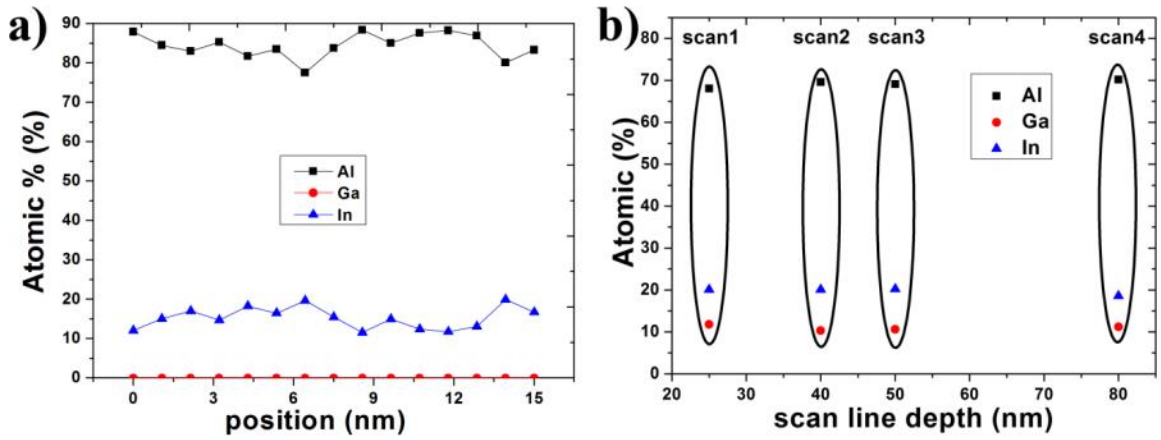

Figure 3.5: a) and b) are EDS measurements made on A383 and TS241, respectively. No gallium has been detected in A383. For TS241, higher indium content is highlighted than given by XRD, in addition, the presence of gallium is not negligible

Thus the horizontal chamber produces systematically ternary AlInN whereas the vertical configuration is more complex. In this instance, the close-coupled shower head was conditioned with specific treatments prior to the growth of TS685 barrier. For this sample, the EDS results are reported in figure 3.6.

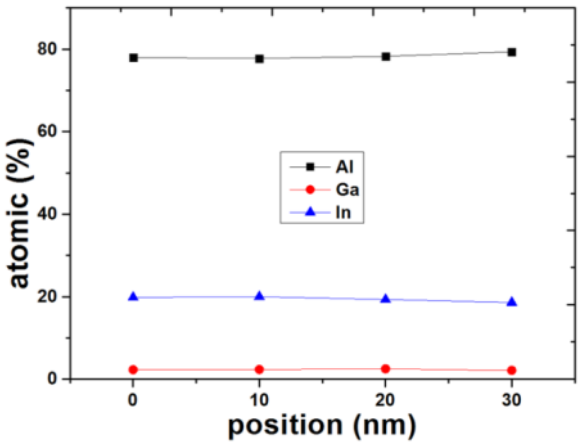

Figure 3.6: EDS results show the strong decrease of the amount of gallium in the epilayer TS685 as the chamber has been conditioned before in contrast to sample TS241

As can be seen, the gallium concentration is noticeably low in comparison to TS241. The average drops gradually when we go from the GaN template to the layer surface where the detected gallium goes to about 1%, which corresponds confidently to the accuracy of the measurement due to geometrical factors of the corresponding

position of the sample in the microscope column. It is thus clear that through this growth process, the unintentional gallium incorporation has been drastically reduced. In parallel, the measured indium content appears to gradually increase toward the surface reaching maximum values just above 20%, whereas the aluminum content stays below 80%.

Regarding the surface morphology, representative regions of A383 (125 nm), TS241 (100 nm) and TS685 (61 nm) are displayed in figure 3.7. For the three samples, the topography is dominated with hillocks. Pinholes and some trenches are also observed on samples from both chambers. Therefore, in the following analysis, the pinholes and trenches were excluded from the roughness measurements. In addition, the only presence of gallium is not the main cause of the formation of such defects.

The roughness of A383 is around 0.9 nm. The hillocks are around 100 nm in diameter and their height is similar to the surface roughness. In comparison, the thinner layer TS241 has a roughness around 1.5 nm. The hillocks on this layer are around 125 nm in diameter. Furthermore, for TS685 which is gallium free, the roughness does not exceed 0.7 nm with hillocks around 90 nm in diameter. Therefore, at similar thicknesses, the quaternary layers tend to have higher roughness than the ternary barriers.

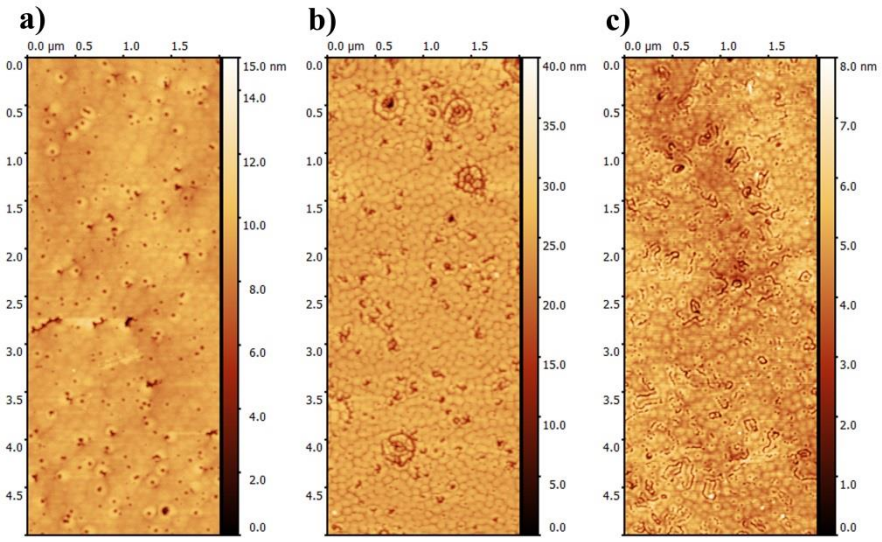

Figure 3.7: Surface topography of a) A383, b) TS241 and c) TS685. For these three samples, the only presence of gallium cannot explain the formation of defects such as pinholes or hillocks. The retained result is that quaternary layers have a higher roughness.

Zhu et al.[81] grew layers between 760 °C and 830 °C with thicknesses ranging from 225 to 400 nm. Without supplying gallium precursor, its unintentional content reaches 45%. By avoiding GaN templates and using a layer sequence of AlN/AlInN, they reported a decrease in the amount of gallium to 2% in the AlInN layer, which led them to conclude that the main source of this parasitic gallium could be due to the diffusion from the GaN template during the subsequent growth. For our samples, the situation is significantly different. A383 (GaN/AlInN) was grown at 810 °C and no gallium has been detected by EDS. In Addition, TS241 has a layer sequence of GaN/AlN/ AlInN, although with an AlN ultrathin layer (2 nm), in comparison to the 100 nm thick AlN of Ref.[81]. The EDS measured indium composition is around 20%, whereas gallium is 11% for TS241.

The next observation of this effect was reported later by Smith et al.[82] who carried out the growth of the alloy at 790 °C in a close coupled shower head also from Aixtron. They pointed out that the gallium incorporation could be decreased subsequently by making a growth interruption during which the chamber was cleaned and the susceptor changed, they report a gallium incorporation of about 1%, with the conclusion that the source of the contamination was most probably gallium from reactor walls. We obtained similar results for sample TS685 which was grown after thermal cleaning, the incorporated gallium dropped to 1%.

Therefore, as also reported in Ref.[82], the source of gallium unintentional incorporation is due to the reactor and the proposed blocking role of an intermediate AlN layer[81] is probably small. A detailed analysis of this gallium incorporation was made by the same group and reported in Refs.[83,84], taking into account that all the steel parts of the CCS reactor are refrigerated, it was concluded that the source of the residual gallium should be the quartz elements such as the susceptor and that the geometry would not be an important factor. The dominant effect was proposed to be the residual vapor pressure due to Ga/In eutectic inside the reactor. However, our observations as reported above for A383 and TS241, in two different reactors, and TS685 from the optimized process in our CCS reactor, show that the reactor geometry is playing a critical role in the process. It was also verified that no leakage was present in the gas lines for the separated organometallics precursors.

3.2.2. Gallium content and growth conditions

In this section, a mechanism explaining the unintentional incorporation of gallium is proposed. To do so, analysis of SiN in-situ passivation layer and layers grown under different pressures were characterized. For instance, the content of the gas phase has been changed in both experiments.

The extent of non-intentional gallium incorporation in in-situ passivation layers has been investigated through TS909. The topography is shown in figure 3.8. The color scale bar goes from -4 nm to +3 nm but the surface is smooth. This is due to the terraces growth steps from the underlying GaN/AlGaInN. The roughness does not exceed 0.6 nm and defects are barely visible.

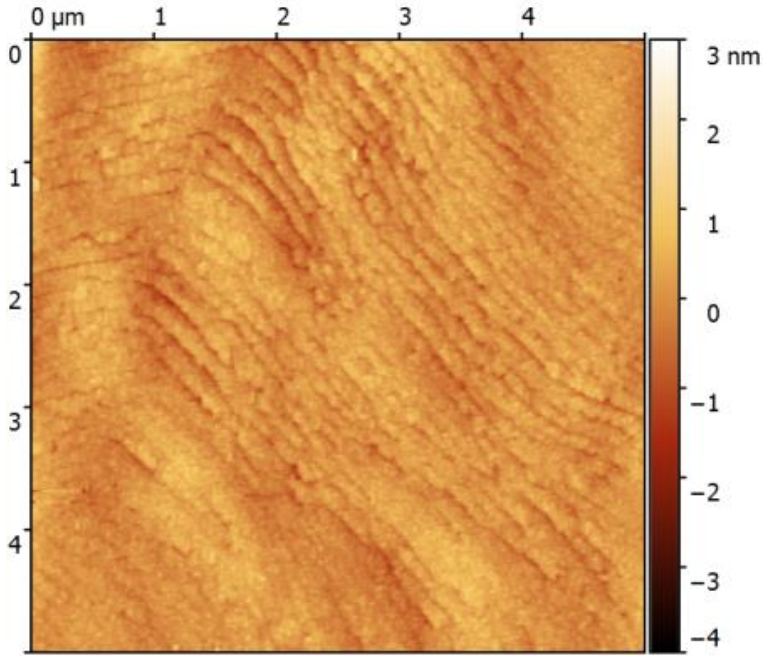

Figure 3.8: Topography of TS909 showing growth steps

As can be seen in figure 3.9, time of flight secondary ion mass spectroscopy (TOF-SIMS), no gallium was observed in the SiN passivation layer. This is further confirmed by our EDS measurements. The composition of the barrier is 66% aluminum, 16% indium, and 18% gallium. As the growth conditions were the same for TS241, the composition is close and indicates the repeatability of the process for different growth runs. Probing the optimized SiN passivation layer indicated 0% of gallium by EDS. Note that this layer has been grown after a re-growth of 150 nm of GaN.

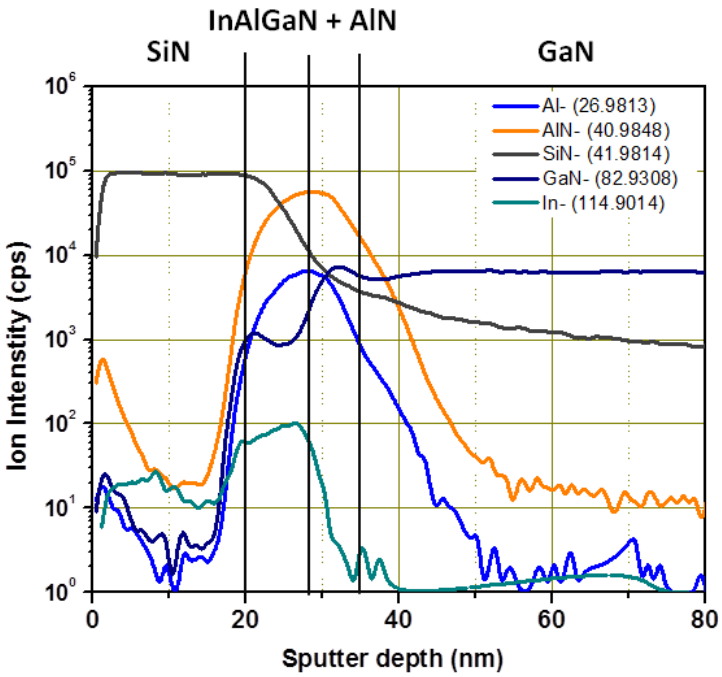

Figure 3.9: TOF-SIMS depth profile on TS909. As can be seen, no gallium was detected in SiN in-situ passivation layer. (Courtesy of Dr. P. Gamarra from III-V Laboratories)

In the scope of looking for a mechanism for the presence of parasitic gallium, we shall now focus on samples TS495–TS497 where the total deposition pressure in the vertical chamber has been stepped from 80 to 120 Torr (Table 3.1), keeping the other parameters constant such as the temperature, time, fluxes, etc. The EDS results for these samples are depicted in figure 3.10. At 50 Torr, the layer composition is 20% and 11% of indium and gallium, respectively. The amount of aluminum is close to 70%. At 80 Torr, for TS495, the amount of gallium has been lowered by twice to 6%. The indium content measured is around 15% and the aluminum is close to 80%. The gap observed here between the amounts of indium and gallium is maintained when the pressure was increased to 100 Torr and then to 120 Torr. The indium content was increased respectively to 19 and 20% and the gallium content was increased to 12% for both the samples. Consequently, the aluminum content was decreased by 10% for both TS496 and TS497.

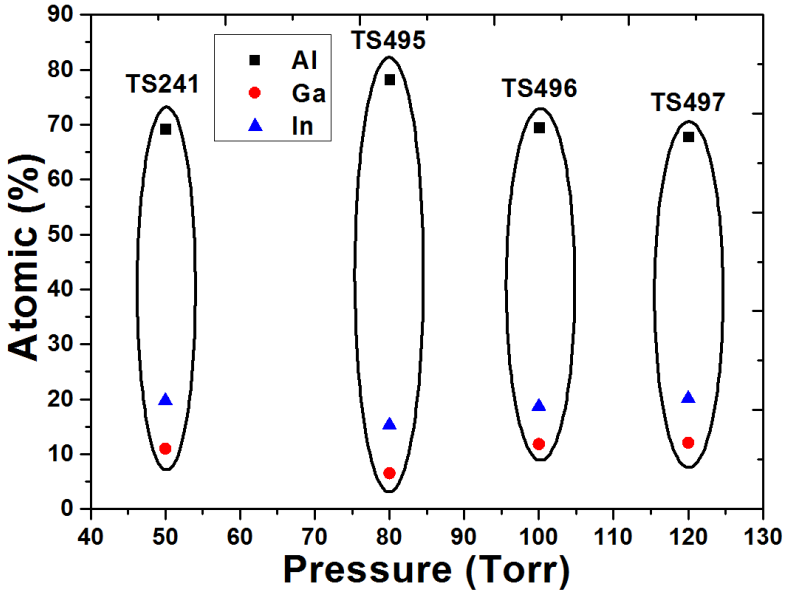

Figure 3.10: EDS results obtained on samples grown with different growth pressures monitoring the evolution of gallium unintentionally incorporated in the barrier.

From the above observation, we assess that the amount of parasitic gallium in the barrier depends highly on the growth conditions such as the pressure. Smith et al.[82] changed the total gas flow rate in the reactor from 8000 to 24 000 sccm, they pointed out that the gallium incorporation could be decreased by half from 24% to 12% using a deposition pressure of 70mbar (52.5 Torr). Hiroki et al. investigated the flow of metallic precursors and showed that supplying TMIn leads to a proportional incorporation of gallium. In contrast, increasing the flow of TMAl has no effect on the amount of incorporated gallium at constant TMIn flow. This may be explained by the higher electronegativity of Al (1.61) in comparison to In (1.78) and Ga (1.81) and the strength of the carbon-metal bond which is higher for C-Al (75kcal/mol) in comparison to C-Ga (60 kcal/mol) and C-In (45 kcal/mol). Therefore, we propose that in the gas phase TMIn can react easily with residual gallium and form gallium-by-products which participate in the growth. Thus as soon as the indium source is turned off, the in-situ SiN passivation layer contains no gallium.

Following these results, our investigation shows that the total pressure is playing an important role as well. Comparing the elemental compositions of TS241, TS909, and TS685 at 50 Torr, one can notice that they have the same amount of indium (20%). Therefore, the incorporation of gallium systematically modified only the aluminum content. This is in agreement with the work reported by Zhu et al.[81],

where the amount of indium was the same (see their sample set III) and only the Ga/Al ratio was affected. Similarly, Reuters et al. [85] showed that increasing the growth pressure induced a simultaneous increase of In and Ga and a decrease of the Al content by half. Most interestingly, the intermediate pressure of 80 Torr leads to a strongly decreased gallium content of 6%. For higher growth pressures, 100 and 120 Torr for TS496 and TS497, respectively, we obtain higher indium content and as well as an increased content of the unexpected gallium. Increasing the pressure, subsequently, leads the decrease of the mean free path of the species in the gas phase. Therefore the chemical reaction rate between TMIn and residual gallium is increased. The incorporation of aluminum is therefore decreased.

3.3. Conclusions

From this analysis of samples grown in a horizontal and a close coupled showerhead reactor, we have observed that the unintentional Ga incorporation is predominantly due to the reactor geometry. We demonstrate that the gallium source is neither the susceptor because the incorporation was uniform along a wafer, nor the GaN buffer. Therefore the remaining source is the shower head and the interior walls during the same run. We subsequently report the evolution of the metals (In, Al, and Ga) in the epitaxial layers as measured by EDS. The aluminum concentration is decreased by some 10% from the expected value at lattice match of the AlInN ternary alloy to GaN. The EDS analysis shows that the indium concentration is not modified; the ratio Ga/In appears to change in a correlated way. Still, the presence of gallium can be avoided by adopting a cleaner growth procedure dropping its content to 1%, but also the total chamber pressure is shown to have a non-negligible influence on this effect. Indeed, a moderate pressure of 80 Torr is shown to lead to an incorporation of a decreased content of gallium from 12% to 6% for other pressure values.

4 MOVPE of AlInN and AlGaInN: Effects of TDs and IDs

During this research, we noticed that the microstructure of the epitaxial layers, not only depends on the growth conditions but also critically relies on the structural quality of the substrate. The investigated alloys were grown on top of GaN templates which contain crystallographic defects. Therefore, our observations point out the typical role of such defects on the quality of the active AlInN and AlGaInN barriers. In the following, we discuss the effects of 1) threading dislocations (TDs) 2) inversion domains (ID) originating from the underlying GaN and 3) the interaction of these defects with the thin AlN layer at the interface GaN/AlGaInN. The subsequent degradations observed on the barrier are called extrinsic. In a first section, we shall discuss briefly the available substrates for III-Nitrides. In the subsequent sections, we shall present 1) the investigated materials and 2) our results on the microstructures generated by the presence of these defects.

4.1. Substrates

The nitrides layers are mainly grown on foreign substrates such as sapphire, silicon and silicon carbide. For specific applications, high-quality freestanding GaN (FS-GaN) is used as the substrate.

This type of hetero-epitaxy leads to the introduction of a high density of defects due to the different physical properties [86]. For the choice of a substrate some parameters need to be examined carefully for the success of the epitaxy: 1) the symmetry between the two materials, 2) the lattice mismatch, 3) the thermal expansion coefficients and 4) the thermal conductivity.

In the search for a surface where to carry out the epitaxy, the first condition is to have a similar surface as that of the layer, indeed, the epitaxy of wurtzite GaN will take place more easily on top of hexagonal symmetry (SiC) or pseudo-hexagonal ones (0001)-sapphire, (111)-Si. Then, the next property for good epitaxy will be to take care of the lattice mismatch which governs the different positioning of the atoms in the two lattices, leading to strain and formation of defects at the interface depending on its amount. Table 4.1 shows that SiC/GaN heterostructure has the smallest in-plane lattice mismatch.

In addition, the growth is carried out at high temperatures, and during the subsequent cooling down to room temperature, the behavior of the layer and the substrate are governed by their own thermal expansion coefficients. The associated mismatches may lead to the formation of additional defects.

	GaN	Si	SiC	Al2O3
In-plane lattice mismatch to GaN (%)	0	-17	3.1	+16
Linear thermal expansion coefficient [.10^{-6} K^{-1}]	5.6	2.6	4.4	7.5
Thermal conductivity [.$W.cm^{-1}K^{-1}$]	2.3	1.6	4.9	0.25
Price ($)	3000	20	1500	50

Table 4.1: Available substrate properties for hetero-epitaxy of nitrides[1].

For specific applications such as high power devices, the thermal conductivity of the substrate is an important parameter. Indeed, heat needs to be rapidly evacuated from the active areas of the device in order to avoid overheating and device failure. As can be seen in table 4.1, for this field, SiC is the substrate of choice.

4.1.1. Al_2O_3

The growth of GaN on sapphire have been conducted on several orientations as summarized by Liu et al.[86]. The most common orientation remains [0001] and results in a 30° rotation of the GaN in-plane direction with respect to in-plane sapphire, therefore, the epitaxial relationship is $[11\bar{2}0]_{GaN}||[10\bar{1}0]_{Sapphire}$ and the mismatch is reduced from 30% to +16%. The low thermal conductivity of sapphire makes it poor at heat dissipation and may cause device failures[1]. Furthermore, the large mismatch between both thermal expansions coefficients lead to film cracking during the cooling phase from the growth temperature. This effect is more observed in thick layers due to higher induced biaxial compressive stress generated in GaN and both substrate and layer would crack as exposed in the work of Etzkorn and Clarke[87]. Moreover, the insulating behavior of sapphire imposes electrical contacts to be at the top of the devices which elaboration is not straight forward. Despite all these drawbacks sapphire remains the most used substrate for the growth of GaN based devices. It is attractive because of the low cost and large area available substrates.

In order to reduce the effects of the above problems, a technique known as two-step growth produces the smooth high crystalline quality of GaN. This method was developed by Amano et al.[88]. The authors deposited a thin layer of AlN at low temperature (LT) around 500 °C on sapphire before the high temperature (HT) growth of GaN. The LT growth produces island like structures with different crystallite orientations. During temperature ramping phase the islands will grow laterally and will coalesce forming a smooth GaN surface when the final growth temperature is reached. This process traps dislocations in the first step in the regions between the early formed islands. Only a few of them cross the buffer layer leading to a dislocation density of around 10^8 cm^{-2}. Using this two-step growth, high-quality AlGaN/GaN HEMTs have been obtained on a sapphire substrate having mobility around 1410 $cm^2.V^{-1}.s^{-1}$ and density carrier concentration near 10^{13} cm^{-2} at 295 K[89].

4.1.2. Si

To lower the cost of GaN-based devices, the growth of III-nitrides on Si is by far the most interesting choice because it can be achieved on wafers up to 12" ensuring device fabrication on large areas. For instance, blue LEDs[90] have been demonstrated in 1998.

For transistor applications, Si remains attractive due to its intermediate thermal conductivity in comparison to other substrates. For instance, its thermal conductivity is 6 times higher than sapphire. Unfortunately, GaN cannot be grown directly on Si due to the low-temperature reaction between the two materials. Prior to GaN epitaxy, a nucleation layer should be grown first. In this instance, AlN is nowadays widely employed as a nucleation layer. Yang et al.[91], studied the effect of the AlN thickness and found that few nanometers of AlN will result in the formation of pinholes due to dislocations at the surface of GaN, and around 100 nm thick AlN, GaN will crack as a strain relaxation mechanism. Lahrèche et al.[92] deposited AlN by MOVPE at 1060 °C, with a dislocation density in the GaN around 10^{10} cm^{-2}. Despite this amount of TDs, the electron mobility of their AlGaN/GaN HEMT was not less than 813 $V^{-1}.cm^2.s^{-1}$ at 300 K.

4.1.3. SiC

Even with a low thermal expansion mismatch between SiC and GaN, the density of defects can be high because GaN does not wet well SiC[93]. The nucleation

temperature of GaN on SiC is less than 800 °C leading to a three-dimensional growth and high surface roughness due to the 3.1% lattice mismatch. Therefore, the use of an AlN nucleation layer is also commonly adopted[94]. Indeed AlN can nucleate in a two-dimensional mode at more than 1100 °C leading to a good epitaxial layer of SiC/AlN/GaN.

In fact, silicon carbide is the most suitable substrate for GaN nitride based high power transistors. It has the smallest mismatch with GaN regarding thermal expansion coefficient. SiC is attractive due to its highest thermal conductivity which is for instance almost 10 times higher than sapphire. Recently, Dogmus et al.[95] reported an electron mobility of 1800 $V^{-1}.cm^2.s^{-1}$ at room temperature for HEMTs devices.

4.1.4. GaN

The growth of GaN by homo-epitaxy on bulk GaN was demonstrated by Kirchner et al. in 1999[96]. However, small areas typically less than 10 mm^2 were obtained[97]. The alternative is the growth of the so-called freestanding GaN (FS-GaN). Hybrid vapor phase epitaxy (HVPE) techniques can be used which is basically the growth of thick GaN typically up to few millimeters on sapphire. Sapphire seed will be removed then by mechanical polishing or laser ablation[98,99]. This kind of complex process makes FS-GaN the most expensive substrate for III-Nitrides, however, the density of defects such as the density of dislocations in FS-GaN can be reduced to 10^6 cm^2. In 2009, Dwilinski et al. [100,101], by means of ammonothermal growth of bulk GaN, the authors reported a lower density of dislocations typically 10^3 cm^2. Nowadays, FS-GaN substrates are around 4" and are the most adequate for high power applications for nitrides. In this instance, hall mobility around 1920 $V^{-1}.cm^2.s^{-1}$ with a dislocation density lower than 10^7 cm^{-2} have been obtained by Storm et al.[98,102] on AlGaN/GaN HEMTs.

4.2. Extrinsic degradations of AlGaInN and AlInN

In the following, we designate extrinsic degradations of the barrier defects having their origin the GaN template where TDs or IDs can be found or due to any interaction of these defects with the AlN spacer between the barrier and the GaN.

In this instance, Northrup et al.[103] estimated theoretically the formation energy of pinholes in InGaN connected to a screw type threading dislocation. In addition, and by assuming that the theoretical behavior of AlInN and InGaN can be similar,

Kehagias et al. [104] observed that pinholes were only due to dislocations with screw components in AlInN. This was confirmed later by Miao et al. [30] who reported that pure edge dislocations do not generate pinholes in AlInN and that only dislocations with a screw component lead to the formation of pinholes. In contrast, Minj et al. [105] observed that for AlInN also edge dislocations can be connected to pinholes.

On the other hand, the presence of an ID can change the growth kinetics at its immediate surroundings. It has been demonstrated that Ga-face terminated surface is smoother than N-face terminated surface[106–109].The co-existence of both polarities also induces pyramidal growth around the inversion domains in GaN[109,110] as well as in AlN[111] while the surface morphology is more complex for InN[112]. For ternary alloys, such as super-lattices alloys AlGaN[113] and InGaN[114], it has been reported that IDs terminate with v-pit defects at the surface.

Usually, the introduction of a thin AlN layer at the hetero-interface AlGaInN/GaN heterostructures for HEMTs applications improves the 2DEG density by reducing the alloy scattering effect. In addition, it provides a better confinement of the electrons in the 2DEG region. However, its thickness has to be carefully controlled and optimized. Song et al.[115] reported that a thick AlN induces cracks of few microns to appear at the AlGaN surface. The electron mobility was equal 1590 $V^{-1}.cm^2.s^{-1}$ and decreases for higher growth times. Xun et al.[116] obtained best results with 1.3 nm for InAlN HEMTs at 1051 $V^{-1}.cm^2.s^{-1}$.

TDs and IDs originating in the GaN buffer lead to the appearance of pinholes as shown from the above literature. In this instance, the effect of each type of TD remains unclear. In addition, we assess the effect of IDs on our AlGaInN barriers which have a thin AlN spacer. Indeed, determining the exact origin and effect of each defect may help to produce higher quality layers by MOVPE through the only optimization of the growth conditions.

4.2.1. Samples

In the previous chapter, we showed that the surface morphology of AlGaInN barriers exhibits pinholes, hillocks, and trenches. We now attempt to establish the relationship between defects observed on the surface and defects originating from the GaN.

The samples, discussed in this section, are presented in table 4.1. One MD3156 ternary barrier was grown on Si substrate with an AlN nucleation layer prior to the

growth of GaN buffer layer. All other samples were grown on a sapphire substrate with GaN as nucleation layer prior to the GaN buffer layer. In table 4.1 only one sample has a thin AlN interlayer at the interface of GaN and AlGaInN.

samples	pressure [Torr]	temperature [°C]	content (EDS) [Al/Ga/In] %	Barrier nominal thickness (TEM) [nm]	AlN interlayer thickness [nm]	GaN thickness [µm]
MD3156	52.5	780	65/0/35	100	0	1.5
TS652	50	875	72/11/17	96	0	1.1
TS654			73/12/15	20	0	1
TS684			69/16/15	60	0	2
TTS241			70/11/19	100	1.8	1.2

Table 4.2: Main properties of samples discussed in this chapter

4.2.2. Effects of sapphire and silicon substrate on the quality of GaN

In the scope of determining the effects of defects originating from the GaN template on the barrier, we firstly observed samples where sapphire and silicon were used as substrates. The two samples in this section are MD3156 (AlInN) and TS652 (AlGaInN). These samples were grown on silicon and sapphire substrates, respectively. Their thicknesses are 100 nm and 96 nm, respectively. For MD3156[19], a ~30 nm AlN nucleation layer was used prior to the 1.5 µm GaN buffer layer. In this sample, GaN was grown in two steps (1 µm + 570 nm) with a strain engineering low-temperature AlN interlayer. For TS652, 70 nm of LT-GaN was used as a nucleation layer prior to the growth of 1.1 µm GaN buffer layer. Figure 4.1 shows diffraction contrast images of both samples under g= 10-10. The dislocation density of MD3156 and TS652 is 3×10^{9} cm^{-2} and 10^{9} cm^{-2}, respectively. As can be seen in figure 4.1a for TS652, only a few TDs reach the barrier. For MD3156, the dislocation density is clearly higher in the first 1 µm GaN as can be seen in figure 4.1b and only a few reach the surface.

As can be seen from diffraction contrast images, only a few dislocations reach the barriers in both cases. Furthermore, the crystalline quality of TS652 is better in comparison to MD3156. For MD3156, the roughness of the layer is already visible and the contrast of the barrier is brighter and less homogeneous than for TS652.

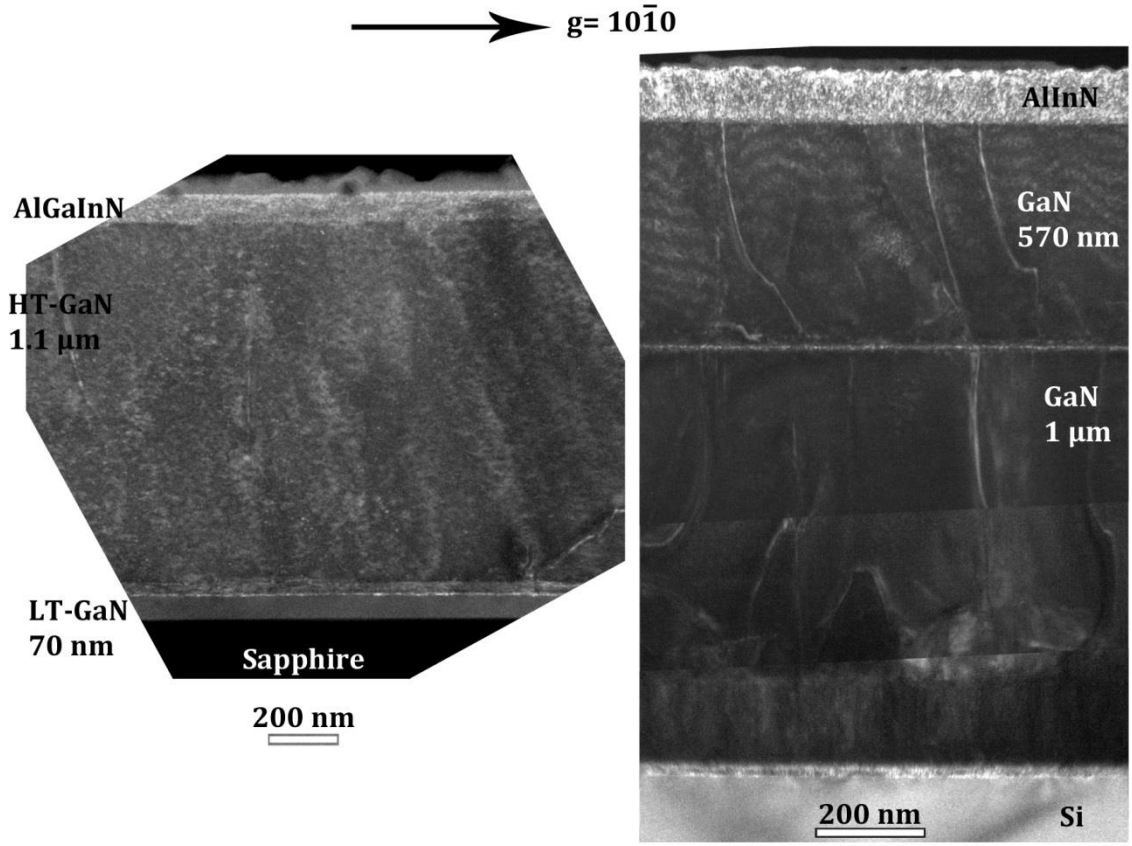

Figure 4.1: Weak beam dark field diffraction images cross sections of a) TS652 and b) MD3156. In both samples, the TDs are confined far from the barrier.

For the latter, the contrast is more uniform and the roughness of the layer is not visible. The strain related contrast is not directly connected to TDs as can be seen for both samples. Therefore, in this case, the quality of the layer does not depend directly on the substrate nature or quality (sapphire or silicon). From EDS, the indium composition of MD3156 was close to 35%, thus the layer is under compressive strain. Also from EDS, the composition of TS652 is around 72% Al, 11% Ga, and 17% In. The average mismatch is 0.17% with respect to GaN, so the layer is nearly lattice matched. Therefore, using specific growth steps as described by Amano et al.[88], the TDs in GaN can be lowered around 10^{-8} cm^{-2} leading to a high-quality GaN buffer layers. Therefore the observed degradations of the barrier do not depend only on the TDs or the use of a specific substrate, but here, on the strain state of the barrier.

4.2.3. Sub-grain boundaries

To determine the effect of TDs on the crystalline quality and surface morphology of AlGaInN, we carried out systematic SEM observations and noticed characteristic morphological features which are not randomly distributed. The micrograph of Figure 4.2 depicts alignments formed by separated pinholes at TS654 surface. Two of

these are highlighted with blue hexagonal-shapes placed at their "centers". The pinholes are aligned along short distances and the alignment change direction by $n\frac{\pi}{6}$, $n \in \mathbb{N}$ as shown with the red V marks.

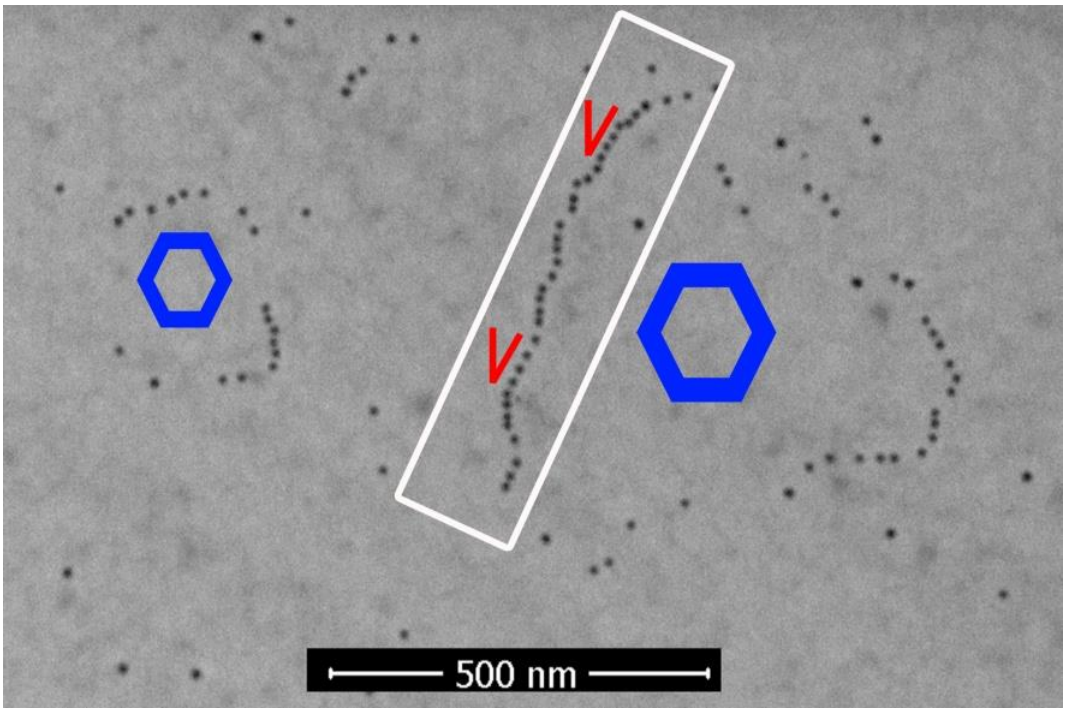

Figure 4.2: TS654 surface shown with SEM. Pinhole not randomly distributed are highlighted with blue hexagonal-shapes. The white rectangle shows the array of pinholes where a FIB-specimen was prepared for TEM investigation. Possible changes in the propagation of pinholes arrays are highlighted with red V-marks.

Using a FIB, a TEM specimen has been prepared around the area marked with a white rectangle. The area was then observed in TEM. Figure 4.3a-c show respectively weak beam images with g= 11-20, g=10-10 and g= 0002. The stars point to the same area in the 3 micrographs. From visibility criterion (g.b), one can assess that all dislocations seen with g= 0002 are mixed type threading dislocations as they are in contrast with other diffraction vectors. However, the majority of TDs in this area are **a**-edge type threading dislocations.

In particular, two groups of dislocations are pointed out in Figure 4.3b with "**X**" marks. These two groups indicate the presence of sub-grain boundaries in GaN originating from the interface GaN (nucleation layer) / GaN (buffer layer). These dislocations open up into pinholes at the surface of the sample.

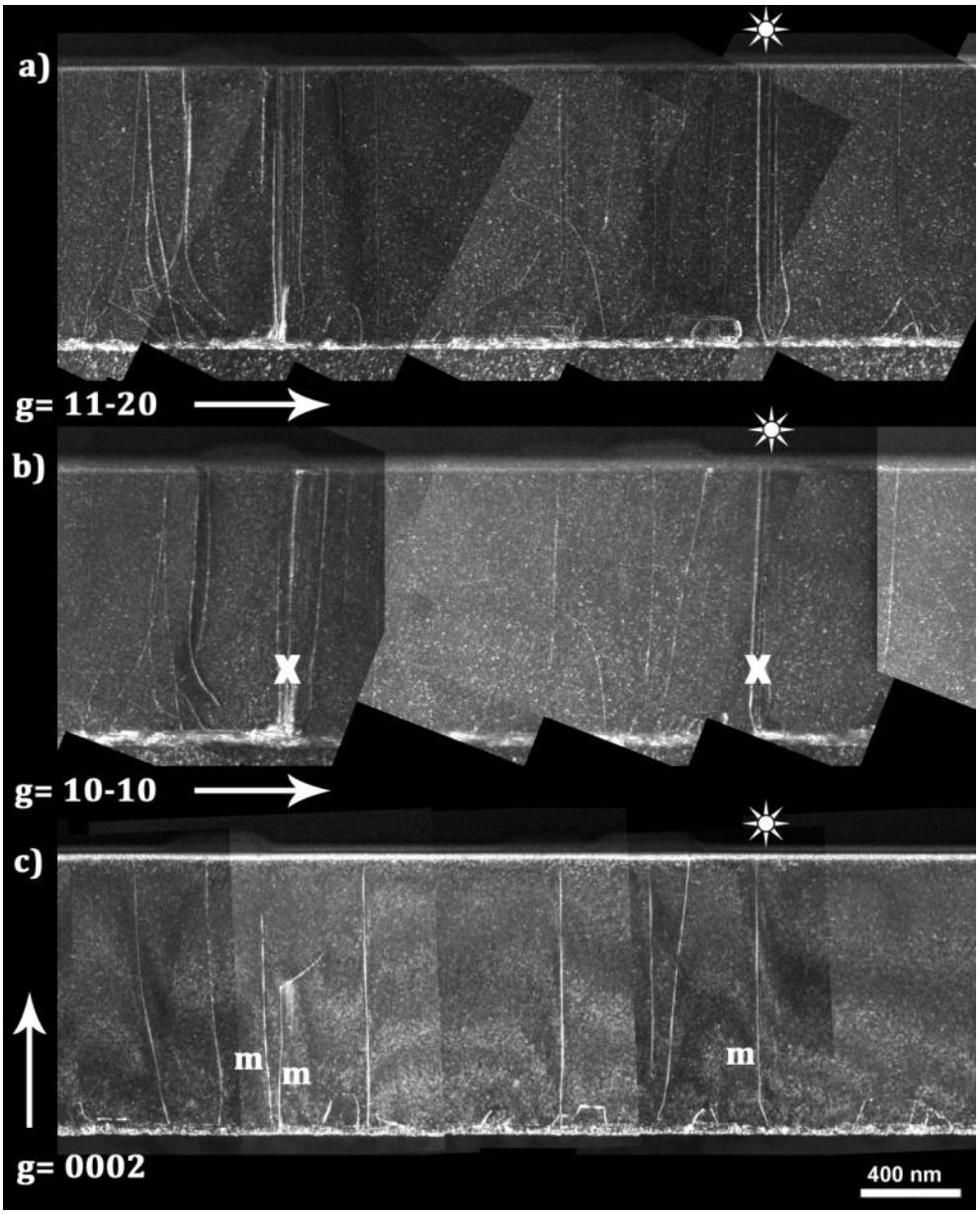

Figure 4.3: TS654: Weak beam dark field cross-section micrographs of the FIB lamella recorded with a) g= 11-20 b) g= 10-10 and c) g= 0002

The thinned FIB specimen contains thus 2 ends of the array of pinholes shown inside the white rectangle of the SEM of Figure 4.2. Similar defects were observed by Rhode et al. [117] for InGaN layers grown on GaN where bent TDs at the interface open in pinholes to finally coalesce and form trenches at the surface of the epilayers.

For InGaN multi-quantum wells (MQWs), Massabuau et al.[118] observed similar defects where the area within the trench can have a height lower or higher or at the same thickness than the surrounding matrix. For MQWs, thicker areas within the trenches indicate higher indium incorporation rate[119] as part of strain relaxation mechanism[117]. In our case, for the quaternary TS654, one can notice the uniform

contrast all over the observed area from SEM analysis meaning a uniform barrier thickness (20 nm) that was confirmed later by TEM observation. This means that the areas within the pinholes array have the same growth rate as the surrounding matrix. In fact, the quaternary barrier TS654 contains an average 73% Al, 12% Ga and 15% In, indicating a mismatch of -0.02% thus the layer is nearly lattice matched. Therefore a mechanism of strain relaxation of the barrier as that reported above for InGaN multi-quantum well does not appear to be operating in our case.

Furthermore, for each of the two groups of dislocations, one can notice that the threading dislocations at their extremity are mixed type TDs. They are marked "**m**" in Figure 4.3c. On the other hand, we have observed from the SEM of Figure 4.2 that there is a change in the direction of propagation of pinholes by $n\frac{\pi}{6}$, $n \in \mathbb{N}$. Rhode et al.[117] and Massabuau et el. [118] suggested that pinholes are generated along <11$\bar{2}$0> directions in the InGaN epilayers leading to trench formation. Based on their assumption, directions with higher number of pinholes in Figure 4.2 are <11$\bar{2}$0>.

Therefore, the sub-grains were found to form at the interface between the LT-GaN and HT-GaN leading to TDs in the buffer layer. These TDs open up into pinholes forming a network with average propagation directions <11$\bar{2}$0>.

4.2.4. Individual TDs and pinholes

The surface morphology of TS654 is shown in the AFM of Figure 4.4. The white hexagonal shape indicates a subgrain boundary formed by an array of pinholes similarly to Figure 4.2. In addition, the surface contains individual hillocks with pinholes at their centers. The white arrows point toward the first type of pinholes on top of large hillocks 85 ± 4 nm in diameter than the second type of pinholes which are connected to hillocks whose diameter is 32 ± 4 nm. In Figure 4.4, all pinholes have the same diameter of around 25 ± 3 nm.

In order to assess if the observation of pinholes having the same diameter and that hillocks have different dimensions is limited to this sample, TS684 and TS241 were also investigated. In comparison to TS654 (barrier thickness 20 nm), the AlGaInN barrier of sample TS684 is 60 nm thick and it is 100 nm for TS241 as reported in table 4.1.

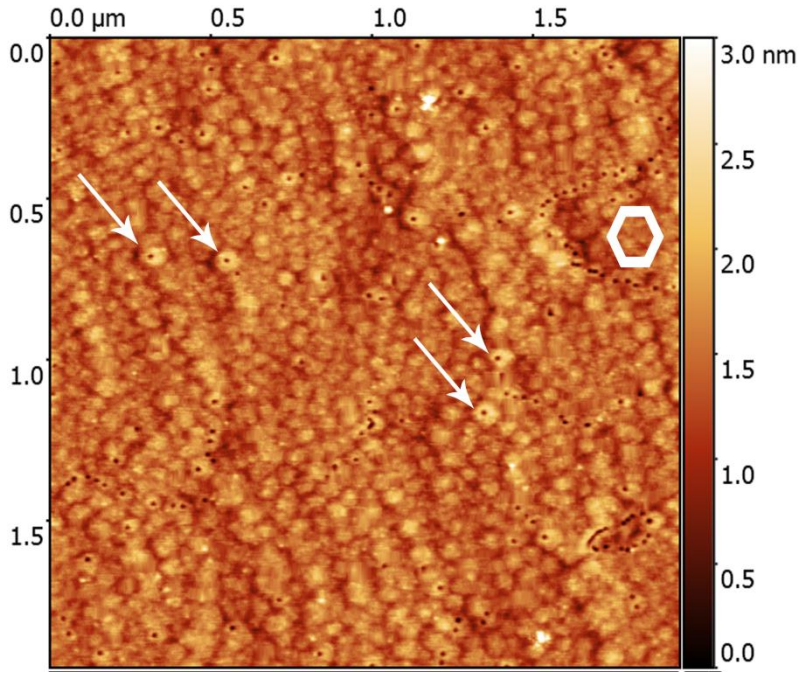

Figure 4.4: Topography of TS654 shown with AFM. The morphologies of individual pinholes are different; they are all on the top of hillocks but these latter have different sizes.

The AFM micrograph of Figure 4.5a represents a typical region showing morphological defects on TS684. Similarly to TS654, the layer surface is covered with hillocks, pinholes and even coalescing pinholes into trenches of different sizes are highlighted in a white square. The average density of pinholes is 4.3×10^{9} cm^{-2} as determined from 6 μm^2 areas. In the following, a population of 110 pinholes was characterized. They were selected as being sufficiently apart so that no close defects were interfering with the measurements of the characteristics of the associated hillocks diameters and heights.

Figure 4.5b shows the bar chart of the pinholes population distribution according to their diameters. In contrast to TS654, regarding the diameter of pinholes, two distinct families can be observed. On the left side of the graph, the first family is sharing an average diameter of 32 ± 1 nm. Letter "v" is assigned to 3 pinholes as examples in Figure 4.5a. They are the smallest pits. One can see that they can be located between hillocks; as it is the case for v_1 and v_2, or at an edge of a hillock; which is the case of v_3. Therefore a connection between hillocks and v-pinholes may not be straightforward. This observation holds also for ternary alloys as we can see for sample A383 (125 nm thick) in figure 3.7a (chapter 3).

The right side of Figure 4.5b shows pinholes with an average diameter of 46 ± 4 nm. These pinholes are always on the top center of hillocks. For these pinholes, we

have measured the diameters of their hillocks as shown in Figure 4.5c. As can be seen, the pinholes that we have observed can be further separated into two categories depending on the hillocks diameter. 59 % have a diameter of 79 ± 7 nm (left side of figure 1c) and 41% have a diameter of 111 ± 7 nm (right side of figure 1c). Thus, letters "e" and "m" were assigned to examples in Figure 4.5a, respectively. Note the larger number of e-pinholes in the selected population. In addition, the hillocks of e-pinholes and m-pinholes have their heights at 1 ± 0.2 nm and 2 ± 0.3 nm, respectively.

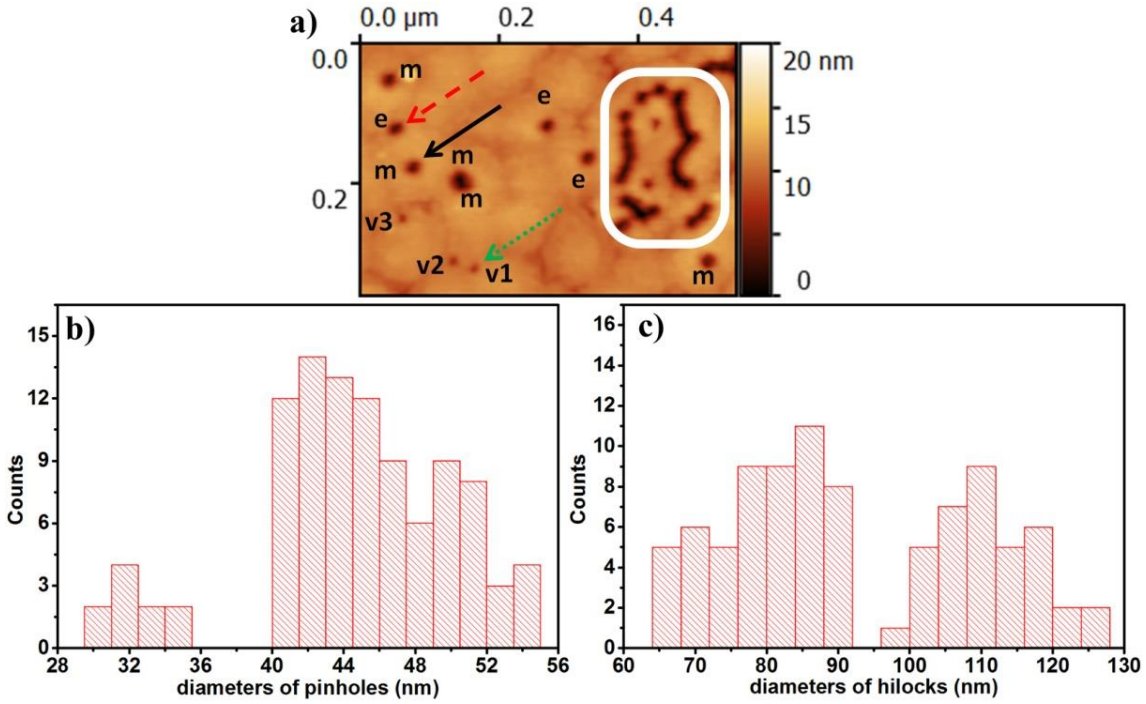

Figure 4.5: a) Representative AFM surface morphology of TS684 b) distribution of pinholes population regarding their diameters that shows two distinct distributions and c) hillocks diameters of pinholes with two distinct distributions indicating two different origins

The same approach has been used for sample TS241. The pinholes density for TS241 is 0.9×10^{9} cm^{-2}. They were also classified similarly into two families regarding their diameter. Interestingly, the first family (v-pinholes) is the same as for TS684. But, for the pinholes of the second family, the average diameter of the pits is increased by ~66%. Note that the thickness of sample TS241 has been also increased by ~66%.

In order to investigate the relationships between the type of TDs and the pinholes, TEM observations were carried out in cross section and plan-view.

For cross-section, SEM was used to locate the features of interest and corresponding zones were prepared by FIB. A typical zone for sample TS684 is

displayed in figure 4.6a where the white rectangle corresponds to the estimated TEM lamella. As can be seen, the observed zone contains some nine large pinholes and a small one as indicated by the black arrow.

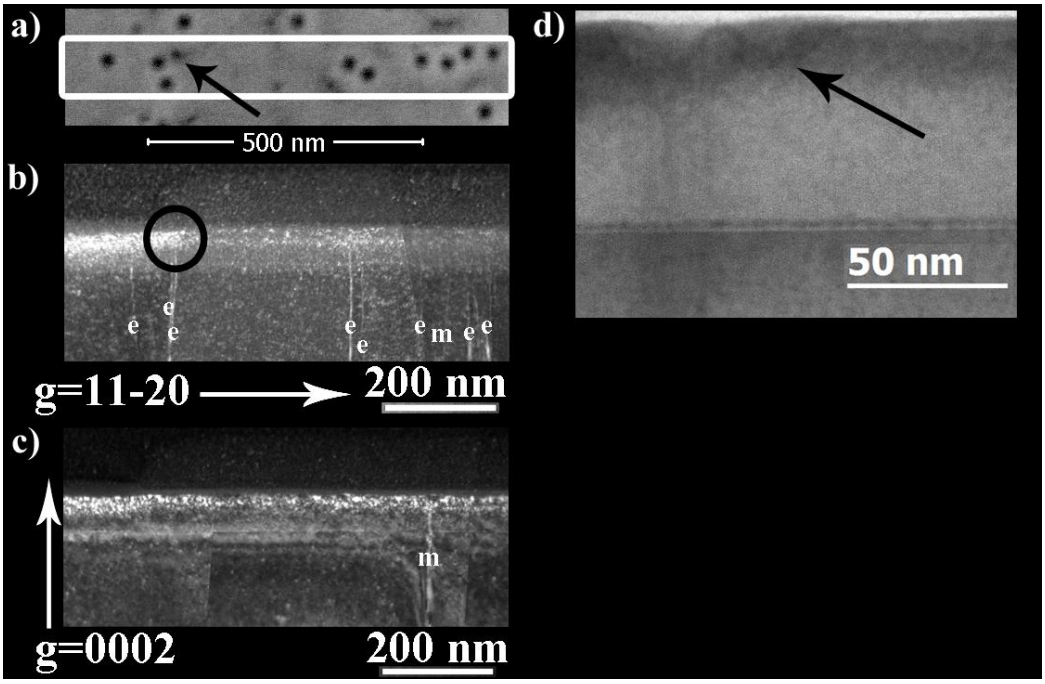

Figure 4.6: TS684 a) SEM of the investigated region. The arrow points to a small diameter pinhole, b) and c) are weak beam TEM images using g= 11-20 and g=0002, respectively for identifying "e" edge type threading dislocations and "m" mixed type threading dislocations. The black circle shows the region magnified in d) the ADF micrograph showing a pinhole not connected to a dislocation. This pinhole is indicated with black arrows.

The corresponding area has been analyzed by TEM using diffraction contrast images with both g= 11-20 and g= 0002 as shown respectively in figure 4.6b and figure 4.6c. Through visibility criterion (**g.b**), one mixed type dislocation is designated by "m" whereas the other TDs are identified as edge type dislocations and are designated by "e". The number of dislocations in this region does not exceed nine. Figure 4.6d is an annular dark (ADF) field image at a higher magnification of the region in a black circle from figure 2b using 6 cm camera length. In this region, one counts 3 pinholes and 2 dislocations. The pinhole to the right (black arrow) in both figure 4.6a and fig 4.6d is not connected to any dislocation. Its diameter is 25 nm whereas the two pinholes at its left are larger (40 nm). Therefore this smallest pinhole should correspond to a v-pinhole and its neighbors should be either "e" or "m" pinholes.

On the two samples, additional TEM specimens were prepared for plan view observations (not shown here) and the TDs densities were calculated for each

sample[120]. In each case, the investigated regions extended to more than 6 μm^2 areas in order to be consistent with AFM observations. The measured TDs densities were 2.7×10^9 cm^{-2} and 0.4×10^9 cm^{-2} for TS684 and TS241, respectively. In both cases, these densities are lower than the pinholes densities. Therefore, additional pinholes are formed into the alloy during the growth and have different formation mechanisms. These pinholes should be the v-pinholes identified by AFM and SEM as the smallest and they are not connected to TDs.

In particular for TS684, 68% are "a" type TDs and 32% are "a+c" type TDs. No pure screw type TDs were observed, meaning that their density is probably very small. Therefore the majority of TDs are edge type.

In comparison with AFM trend of the size of the hillocks, the edge type TDs should correspond to what we have designated as e-pinholes so that the remaining mixed type TDs should be connected to m-pinholes.

Indeed, the ratio given by the AFM corresponds to the population of isolated pinholes and this may not reflect the exact density of pinholes. However, as can be seen, the AFM data follows the trend of TEM observations in which all the present dislocations have been counted. Therefore, it can be concluded that all dislocations terminate as pinholes at the AlGaInN layer surface. Then if we take the e- and m-pinholes of the AFM data as the edge and mixed type dislocations from the TEM observation, we can state that the largest hillocks correspond to mixed type dislocations.

From the above observations, it can be pointed that pinholes can be related to hillocks, they are mainly located at their top, and may also form in the coalescence areas in agreement with the work by Perillat-Merceroz[121] carried out in InAlN layers grown using low TDs density freestanding GaN templates. Moreover as clearly shown for the 9 edge TDs in figure 2a and figure 2b, probably depending on the growth conditions, all the types of dislocations can generate pinholes at the layer surface[105], this is in contrast to reports which stated that only screw and mixed type dislocations open up as pinholes[30,104].

Finally, we can propose an identification method of pinholes and dislocations from AFM analysis of the pinhole and its environment for the investigated layers. For a 60 nm layer, when the pinhole has a diameter less than 30 nm, it should be not connected to a dislocation and is due to inherent degradation of the quaternary alloy.

This kind of pinholes can be located between or on top of hillocks. When the pinhole is above 40 nm in diameter, it is systematically in the center of a hillock and always connected to a dislocation. Moreover, the diameter and height of the associated hillock can be used to identify the underlying dislocation type. We have pointed out that the associated hillock's diameter and height of e-pinholes are smaller than for m-pinhole. The e-pinholes are connected to edge type dislocations whereas m-pinholes should be connected to mixed type dislocations.

4.2.5. The IDBs and interaction with a thin AlN interlayer

In addition to TDs, defects in GaN such as IDs can be present, therefore, when present, we investigated their effects on AlGaInN barriers. In this section, we also discuss the noticed strong interaction of the IDs with the AlN interlayer between GaN and AlGaInN.

Two typical samples were chosen, in figure 4.7a the surface morphology of TS652 (96 nm) has a roughness of 1 nm, whereas in figure 4.7b that of TS241 (100 nm) which contains an AlN interlayer is twofold. As can be noticed, in addition to the defects discussed in the previous paragraphs, elongated and concentric trenches are present on the surface of TS241. Similarly to TS241, the surface morphology of TS684 exhibits complex defects as highlighted in Figure 4.5a with a white square

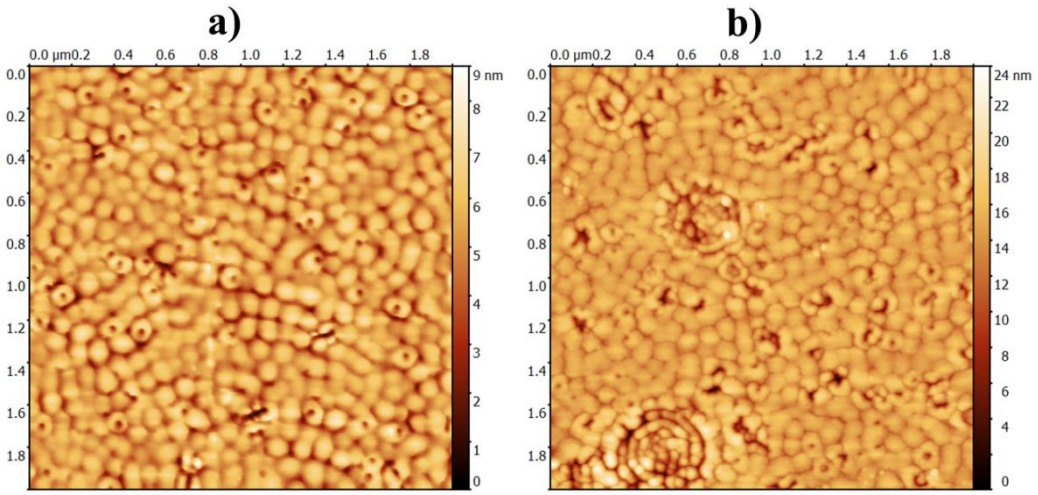

Figure 4.7: AFM topography of a) TS652 and b) TS241

Figure 4.8a-b displays scanning electron microscopy (SEM) micrographs of these structures respectively on TS684 and TS241. The feature on TS684 has a highly elongated central part (Figure 4.8a) which is surrounded by separated pinholes. The morphology is very different on the features at the TS241 surface, in this case, the

nucleus is also elongated but is larger (Figure 4.8b) and it is surrounded by trenches which may or not be closed. In the two samples, the average distance between each nucleus and the first trench/pinholes is around 15 nm (TS684) to 25 nm (TS241).

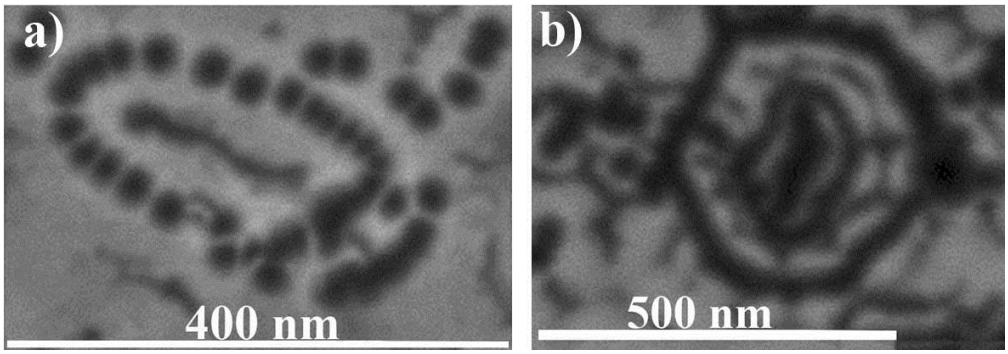

Figure 4.8: SEM micrographs showing surface features on samples a) TS684 b) TS241 linked to inversion domains from the underplaying GaN.

On TS241 TEM specimen has been prepared by FIB across the short length of the core of the feature shown in Figure 4.8b.

The dark field micrograph of the area of interest of Figure 4.9a was recorded with g= 0002. It shows the core elongated parallel to a <10-10> direction.

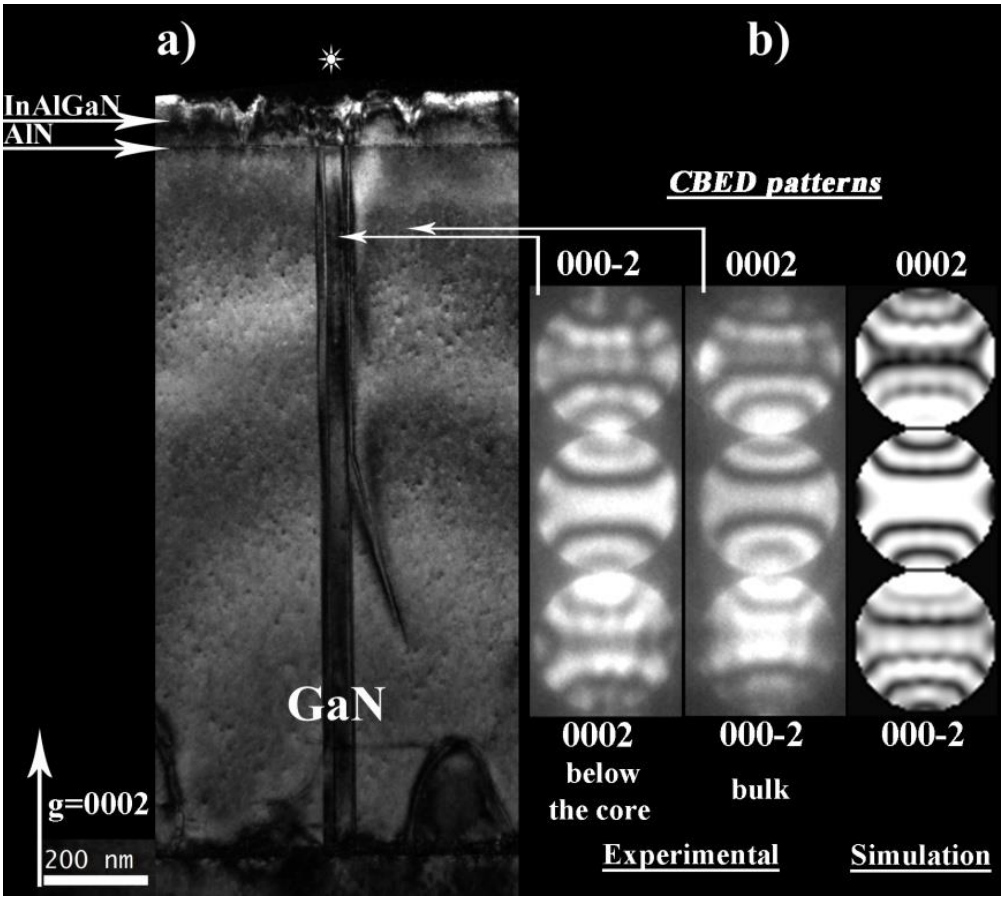

Figure 4.9: a) Cross section dark field micrograph with g =0002 showing ID boundaries b) from left to right CBED patterns: inside the ID, outside the ID, and simulated pattern for Ga-polar matrix at a thickness of 123 nm

In this figure, the white star marks the position of the core in the AlGaInN barrier. In the underlying GaN, one can see a well-defined domain of ~ 40 nm width which exhibits a dark contrast all the way down to the substrate. This contrast indicates the presence of an ID[122]. The convergent beam electron diffraction (CBED) in this area is shown in Figure 4.9b as recorded at 250 nm below the GaN surface. From simulations of convergent diffraction patterns along a <10-10> zone axis, it comes out that we have an agreement at 123 nm with a Ga-polar matrix and the domain has an N-polarity in agreement with previous work[122].

ADF micrographs of Figure 4.10 were recorded at <11$\bar{2}$0> zone axis. The used camera lengths were 8 cm and 20 cm respectively for figure 5a and 5b. The position of the inversion domain boundaries in GaN are indicated by the two arrows “IDBs”. For comparison with the SEM observation, the two trenches have been marked as #1 and #2 (in Figure 4.10a). The asymmetry of the feature is visible with three dips on the right side, whereas only two are present on the left side. On top of the ID, the dip is more pronounced in agreement with earlier observations which showed that the growth of a thin layer above N polar domains should exhibit slower growth rate than the surrounding matrix[107]. In Figure 4.10a, a close examination shows that the AlN interlayer does not have a uniform thickness in this area. It does even disappear at the top of the inversion domain. With a large camera length, the strain contrast is enhanced as can be seen in Figure 4.10b. The boundaries of the inversion domain in GaN region are quite extended, meaning that none of them is viewed completely edge on along the sample thickness. It should also be noticed that on top of the ID, the strain has built up inside the AlGaInN layer.

In the small area of homogeneous contrast just above the ID, EDS measurements show Al enrichment with an atomic composition of 77%, 16%, and 7% respectively for Al, In, and Ga. This composition gives an in-plane lattice parameter 3.184 Å which is very close to that of GaN as calculated from Vegard's law[22]. Away from the defects, the same measurements lead to an average composition of 65%, 22%, and 13% for Al, In, and Ga respectively. The composition inside the external trenches showed significant variation. However, an interesting trend should be pointed out: the aluminum content is changing from 69% up to 76%, and the indium from 12% to

18%; but the gallium composition remains stable and is measured at 12% - 13%, within the EDS error of 1%. Therefore, inside this particular area, there appears to be an interplay between the Al and In along the probed zone.

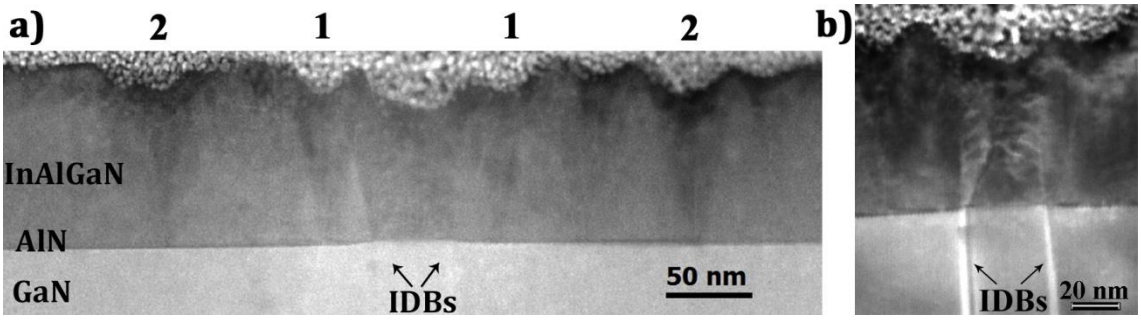

Figure 4.10: The material that is grown on top of an N-polar GaN. a) ADF low magnification cross section showing the whole trench structure along a <112¯0> zone axis. b) Magnified ADF image of the inner part of the ID recorded using a large camera length in order to display the local strain

The high angle annular dark field image (HAADF) of Figure 4.11 shows the left side of the core. It points out the detail of the layer structure and chemical composition from the left IDB to the first trench.

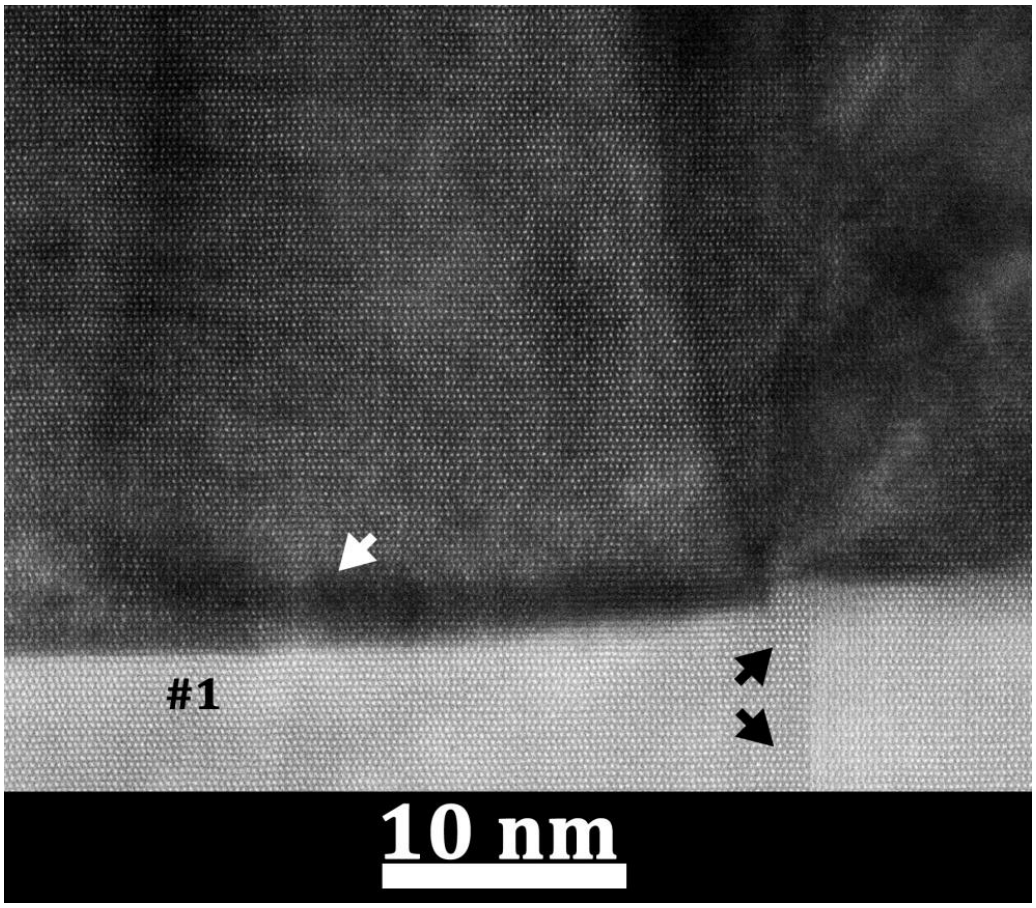

Figure 4.11: HAADF image at the left side of the ID: the changes in AlN thickness (white arrow) at the apex of the trench #1and the growth step (black arrows) at the domain boundary.

Complex atomic configurations occur where the ID boundary meets the GaN surface. The geometry of the ID is reflected in this image where the boundaries are not edge on (black arrows). The strain contrast shows that the defects close to the interface are only localized on the top of the ID. From the IDB to the first step feature (the position is marked with a white arrow), the AlN thickness increases from 1 nm to 1.2 nm. At position #1 from where the apex of the first trench has initiated the thickness of the AlN reaches 3 nm. Past this point, the thickness of the interlayer decreases again until the location of the second trench is reached.

In Figure 4.12, the starting point of the second trench is marked with #2. One can notice that the AlN layer thickness attains its largest value and decreases to the nominal value as shown by the vertical arrows at the interface from the right to the left side of the image. As also can be seen in Figure 4.12 (horizontal white arrows), compositional fluctuations take place along the growth direction below the forming trench.

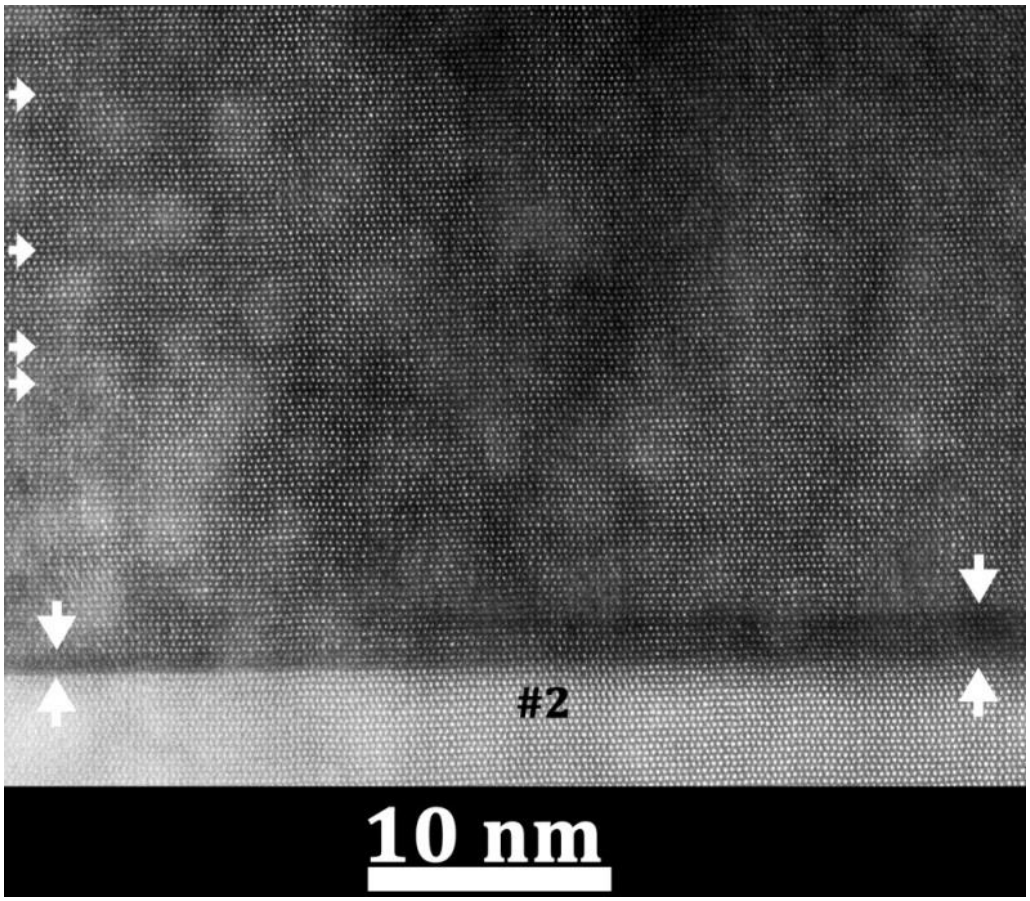

Figure 4.12: The structure of the interfacial area at position #2. Horizontal arrows point to compositional fluctuations and vertical arrows show the changes in the AlN layer

From these observations, such defects appear to form due to the growth dynamic changes on top of the N polar ID and around its immediate surroundings. The growth conditions of TS684, TS652 and TS241 are almost the same, with two notable differences between them, 1) the growth time (TS684: 60 nm, TS652: 96 nm and TS241: 100 nm) and 2) AlN interlayer (only TS241 has a 1.8 nm AlN interlayer between GaN and AlGaInN). Therefore, in a first step, it may be assumed that the trenches started from separate pinholes, these trenches are few hundreds of nanometers long when AlN is present and are closed arrays when IDs are also present. As seen in TS684, the elongated core is surrounded by pinholes, among some of them have already coalesced. In a second step, when the thickness was increased from 60 nm to 100 nm the coalescence of the pinholes led to the formation of the trenches. In addition, only one pinhole circular row was formed around all the IDs observed on the TS684 surface, whereas up to three trenches were observed on TS241 suggesting that their number may be related to the noticed interplay between the Al and In. This interplay leads probably to segregation of adatoms in preferential incorporation sites. For instance, positions #1 (Figure 4.11) and #2 (Figure 4.12) at the apex of the trenches are Al-rich regions. The increase of the layer thickness results in the coalescence of pinholes assisted by different growth rates and probably different velocities for metallic atoms diffusion.

On top of the ID, the growth kinetics is obviously different from the immediate surrounding which is Ga polar. The AlGaInN barrier that is growing on top of N-polar exhibits compositional fluctuation as well as different strain states (contrast changes observed in Figure 4.11). Moreover, it appears to be limited by growth steps. This is dramatically influencing the growth kinetics in the basal plane. As observed in figure 4.12, the AlN layer thickness increases until the point where fluctuations are initiated; this point corresponds to the apex of the trench.

4.3. Summary

Silicon and sapphire substrates which have several kinds of mismatches with GaN can be used while keeping low TDs density around 10^{+8} cm^{-2} thanks to the use of the so-called two-step growth technique. Nevertheless, subgrain boundaries can be generated between the LT-GaN and HT-GaN to accommodate the strain. The few TDs reaching the surface generate pinholes. The correlation between the shapes of pinholes on hillocks and the associated dislocation type has been established. Pure

edge-type threading dislocations open up as pinholes on the top of hillocks. Mixed-type threading dislocations form pinholes on their top but with larger hillocks. Moreover, smaller pinholes (twice as small) not connected to threading dislocations were systematically observed; they form during the growth of the AlGaInN alloy.

Besides pits, additional trenches related to inversion domains were also observed. Their formation could be understood considering the change in growth rate in local N-polar ID and the surrounding Ga-polar region and the build-up of the highly strained local region due to 1) the composition fluctuations, mainly through 2) In and Al interplay and 3) altering the AlN interlayer. This leads to the formation of multiple ring trenches instead of separated pinholes as the barrier thickness has been increased.

5 Growth parameters and quality of barrier layers

The samples that we are discussing in this thesis were grown by the III-V Laboratories. The growth conditions for nearly lattice-matched epilayers in the close-coupled shower head have been under continuous optimization since 2009 when the facility has been installed and for the horizontal chamber the growth has been standard for a long time. In this chapter we report on the effects of 1) pressure, 2) the temperature and 3) the V/III ratio on the surface morphology and crystalline quality of AlInN and AlGaInN, the investigated barrier layers. For each parameter, our results are discussed in the scope of what is available in the literature.

5.1. Introduction

The growth temperatures by MOVPE for InN, GaN, and AlN are around 600°C, 1000 °C and above 1100°C, respectively. The growth temperatures for which the lattice match condition (LM) for each of AlInN/GaN and AlGaInN/GaN is achieved appear to depend on the proper growth conditions as optimized by each group. As we have discussed in chapter 1, the reported values range between 18% and 19.5% of indium content for $Al_{1-x}In_xN$. Moreover, due to the mismatch in thermal expansion coefficients of GaN and the barrier, the LM cannot be maintained from the growth temperature down to room temperature[80].

5.2. Results and discussion

5.2.1. The Samples

In the following, we shall begin by describing simultaneously the effects of the temperature and the V/III ratio on ternary and quaternary alloys. Both surface morphology and crystalline quality are discussed. In a second part, the effect of the growth pressure on quaternary layers AlGaInN is discussed.

As we already mentioned, ternary and quaternary layers were provided by III-V Laboratories who already optimized the growth conditions. Through this thesis, additional ternary layers from Magdeburg [123,124] were also characterized. Table 5.1 displays the samples that are being used in this analysis. The letters “T” and “Q” indicate ternary and quaternary layers, respectively. For these layers, the growth

temperature was varied from 840 °C to 875 °C and the V/III ratio was goes from 787 to 8900. The growth pressure also varied in the range of 50 Torr to 120 Torr.

Samples	Temperature [°C]	V/III	P [Torr]	Barrier Thickness [nm]	AlN interlayer thickness [nm]	Composition: **Al/Ga/In (Method/mismatch)**
MD3317 "T"	840	6500	52.5	43	0	16.6% In (RBS[123])
A1583 "T"	850	787	56.25	30	0	18% (EDS)
TS237 "Q"	850	6950	50	75	1.8	65/11/24 (EDS/+1%)
TS240 "Q"	875	5000	50	75	1.8	(70/11/19) (EDS/+0.4%)
TS241 "Q"	875	6950	50	100	1.8	70/11/19 (EDS/+0.4%)
TS239 "Q"	875	8900	50	74	1.8	(69/14/17) (EDS/+0.2%)
TS684 "Q"	875	-	50	60	0	69/15/16 (EDS/-0.02%)
TS495 "Q"	875	-	80	63	0	79/7/15 (EDS/-0.2%)
TS496 "Q"	875	-	100	55	0	70/12/18 (EDS/0.4%)
TS497 "Q"	875	-	120	50	0	68/12/20 (EDS/0.6%)

Table 5.1: growth conditions of samples in this chapter

5.2.2. Temperature and V/III ratio

In this section, we firstly focus on ternary layers MD3317 and A1583 for which only the V/III ratio and temperature were changed. The surface morphology of the nearly lattice-matched ternary MD3317[123] is shown in figure 5.1a. The roughness is around 1.5 nm. Dips and hills are clearly visible with a $\Delta z \approx 15$ nm as can be seen from the color scale. MD3317 was grown at 840 °C under a nitrogen-rich atmosphere (V/III= 6500). In this case, pinholes are not observed. In contrast, the surface of the ternary layer A1583 exhibits a small roughness around 0.5 nm with hillocks as can be seen in figure 5.1b. The pinholes density is 7×10^{9} cm^{-2}. This ternary alloy was grown at a lower V/III= 787 ratio but higher temperature 850 °C. The average indium content was 18%.

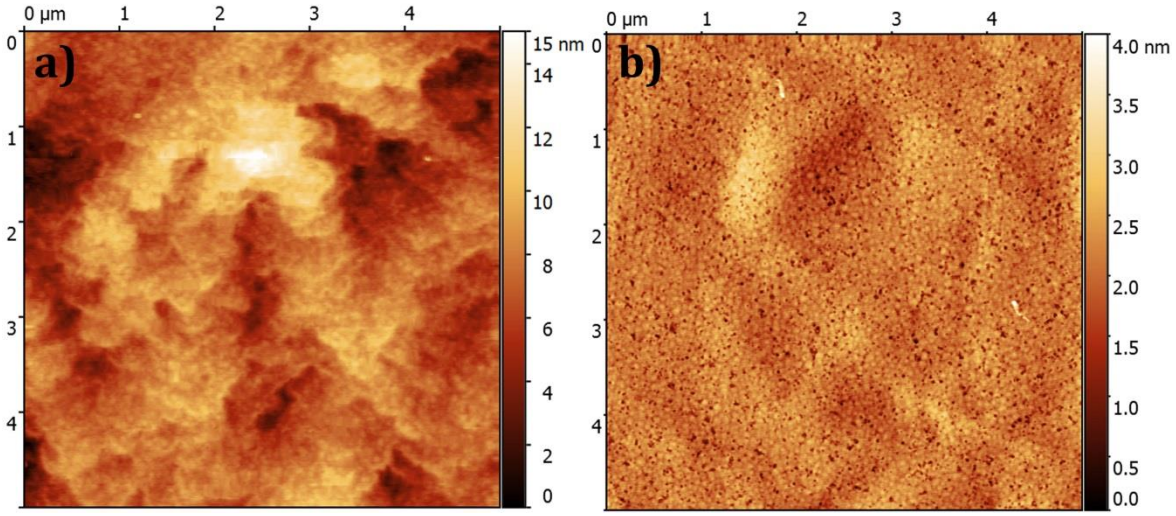

Figure 5.1: Surface morphology of a) MD3317 (840 °C and V/III= 6500 b) A1583 (850 °C and V/III= 787).

The microstructures of the two samples are displayed in the dark field micrographs of figure 5.2 both with $g = 11\bar{2}0$. The two samples share a comparable crystalline quality. The bright contrast can indicate small disorientations or local composition fluctuation leading to different strain states. The TDs densities are in the range of 10^8 cm^{-2} for both samples. Meaning that for A1583, all pinholes are not systematically connected to TDs which density is lower than that of pinholes.

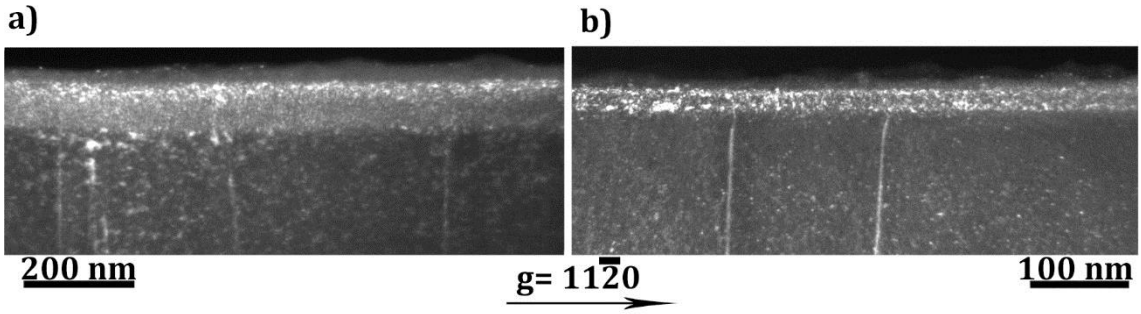

Figure 5.2: Diffraction contrast images in weak beam dark field mode representative regions of a) MD3317 b) A1583

EDS measurements were performed on both samples at different depths. For MD3317 the average composition was 17% with a fluctuation of 8%. This sample was also investigated by Hums et al.[123] with RBS who showed a single crystalline layer. The differences in the results are due to the local aspect of the EDS measurements which are more sensitive to local fluctuations. For A1583, the EDS results show local fluctuations in the indium composition from 17% to 26%.

A similar investigation is now made on quaternary layers. Here, we focus on Sample TS237 which was grown at 850 °C in a nitrogen-rich atmosphere with a V/III ratio of 6950. The surface topography is depicted in figure 5.3a. The roughness is around 2 nm. As can be seen, the surface exhibits a granular structure. In this case, the grains have no specific shape and no pinholes are observed. Interestingly, the region inside the circle has an average height lower than its surroundings around 7 ± 2 nm the diameter is around 500 ± 10 nm. The morphology of this region resembles the morphology induced by an ID originating from the GaN on which a slower growth rate has been observed as described in the previous chapter. In this case, the trenches are not visible.

Adopting the same approach we took for ternary layers, we can now consider TS240. This sample was grown at a higher temperature 875 °C and lower V/III equal to 5000. The corresponding surface morphology is depicted in figure 5.3b. The roughness is lowered to 1.4 nm. In this case, pinholes are visible. In addition, hillocks have mostly hexagonal shapes and their coalescence edges are abrupt. As can be seen, the pinholes are not necessarily centered on the hillocks. Furthermore, hillocks without pinholes have a flat surface. In addition, it is worth noting that this layer contains a thin AlN interlayer, as we already discussed in the previous chapter, the formation of small trenches are due to the crystalline quality and local thickness changes of the AlN.

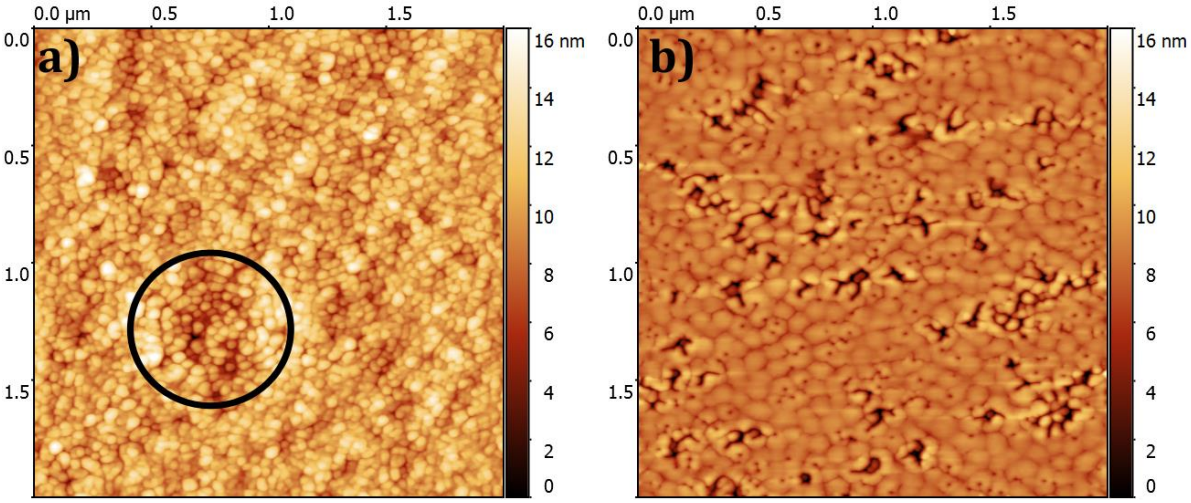

Figure 5.3: AFM topography of images: a) TS237, where one may note the grain-covered surface; b) TS240, grown at higher temperature and lower V/III defects where pinholes and hillocks are still visible.

Figure 5.4a-b shows weak beam dark field images of TS237 and TS240 recorded with $g = 11\bar{2}0$. For TS237 the roughness is clearly visible in figure 5.5a. However, few TDs can be seen to reach the surface, thus the observed degradations in the barrier are not all connected to these TDs. In contrast, TS240 exhibits a flat surface at this scale (fig 5.4b), and only dislocations can be seen to terminate in the form of pinholes at the surface.

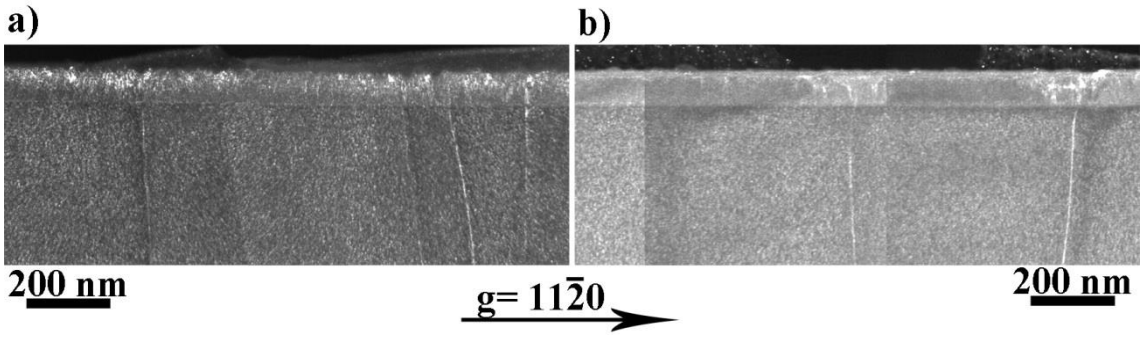

Figure 5.4: images in weak beam dark field mode of representative regions of a) TS237 b) TS240

The chemical compositions of the two layers were investigated by EDS. The average values are shown in table 5.1. For TS237, a lower temperature (850 °C) led to the incorporation of an average higher indium amount (65% Al, 11% Ga, 24% In) than for TS240 (70% Al, 11% Ga, 19% In) which was grown at higher temperature (875 °C). A fluctuation up to 9% in the indium content is observed for TS237 from 20% to 29%. In contrast, the fluctuation of indium content on TS240 was limited to 2%. The gallium fluctuation was around 2% for the two samples but, interestingly, the fluctuation of aluminum follows that of indium. Therefore, there appears to be some interplay between aluminum and indium during the growth of these layers.

Subsequently, the growth temperature was kept constant at 875°C and the V/III ratio was varied from to 6950 to 8900. At 6950 for TS 241, the roughness is close to 2 nm and the morphology resembles that of sample TS240 with flat hillocks of hexagonal shape. Pinholes are observed, on top of the hillocks and not necessarily at the coalescence regions. Moreover, this is similar to higher V/III ratio of 8900 (TS239). Therefore, the variation of this V/III which is almost doubled does not lead to a noticeable modification of the surface morphology at the same growth

temperature; however, the layer quality is best at 875 °C where the roughness and defects have their origin only from defects coming from the underlying GaN template.

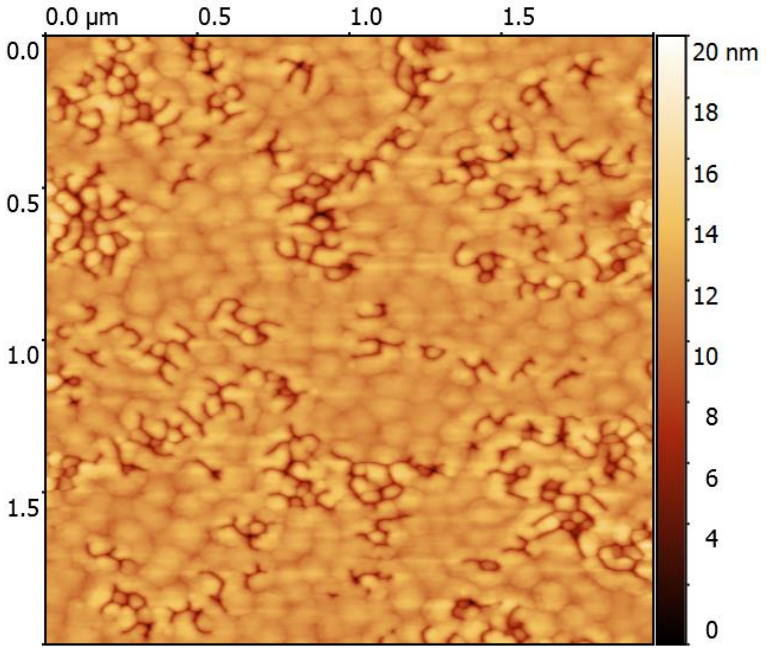

Figure 5.5: Surface morphology of TS239 grown at 875 °C and V/III = 8950. This sample shares the close topography as TS240 and TS241 which were grown a lower V/III.

Discussion

To obtain the lattice match condition, several growth conditions were investigated in the literature. In this instance, Butté et al.[125] reported the growth of AlInN layers with an indium content of 17% at 825 °C. The 100 nm thick layer had a roughness of 0.7 nm. The surface was covered with mostly hexagonal hillocks and no pinholes were present. The absence of pinholes was observed in our both ternary and quaternary layers when the temperature was 840 °C and 850 °C, respectively. In our case, only the quaternary layer presented clear granular features on its surface. From the same group, Perillat-Merceroz et al.[3] reported that a decrease of 1% in the indium content can be obtained by an increase of 5 °C. In addition as Sakai et al.[126] suggested, the lattice match condition can be kept by simultaneously increasing the temperature from 750 °C to 800 °C and reducing the V/III ratio from 24100 to 8100. This was achieved, with the lowest roughness, on the ternary A1583 and the quaternary TS240 for which the growth temperature was increased to 850 °C and 875 °C. Following this approach, we have noticed that the TDs and IDs generate extrinsic degradations meaning that the surface morphology depends strongly on the

growth condition with a combined effect of the extrinsic origins (TDs and IDs). The kinetic roughening can be explained by a reduced surface mobility of adatoms at lower temperatures as suggested by Johnson et al.[127] and Vézian et al.[128] e.g.: The roughening is due to an energy barrier preventing atoms to jumps from a terrace to its bottom. Thus we have observed dips and hills with a $\Delta z \approx 15$ nm for the ternary MD3317 grown at 840 °C and grains for the quaternary TS237 grown at 850 °C.

By increasing the growth temperature and decreasing the V/III ratio, not only the surface morphologies were affected but also the layers compositions. For the ternary layers, the composition fluctuation is reaching 10%. The case of quaternary layers is quite different; the fluctuation of indium/aluminum decreased from 9% to 2% whereas the gallium content fluctuation remained around 2% while increasing the temperature from 850 °C to 875 °C. Furthermore, the average mismatch was reduced from +1% to less than +0.5%. It is also noticed that an interplay between aluminum and indium was observed, whereas, the gallium content was unchanged in the case of the quaternary layers. This reflects the fact that InN grows better at lower temperature[129] and AlN at higher temperature[92], whereas GaN has an intermediate growth temperature[92,93]. In addition, increasing the V/III up to 8900 did not affect the magnitude of the fluctuation in quaternary layers while maintaining the temperature at 875 °C. Also, the surface topography is unchanged.

5.2.3. Pressure

For the growth pressure, four samples were selected for which the pressure was varied. The quaternary layers are TS684, TS495, TS496, and TS497 which were grown at 50 Torr, 80 Torr, 100 Torr and 120 Torr, respectively.

The two first samples (TS684, TS495) are exhibited in figure 5.6a and Figure 5.6b hillocks and pinholes are observed. Here again, the pinholes are not necessary between the coalescence regions but they are also topping hillocks. The roughness of the former is 1.4 nm and whereas for the latter it is 0.6 nm. For these samples, the height of hillocks without pinholes as a function of their diameter is shown in figure 5.6c. As can be seen, on the former, the hillocks have a larger radius and their tops are flatter than on the latter which indicates a lower density of individual hillocks with a

larger height on TS684 than on TS495. Thus, growth steps are still better visible on TS495.

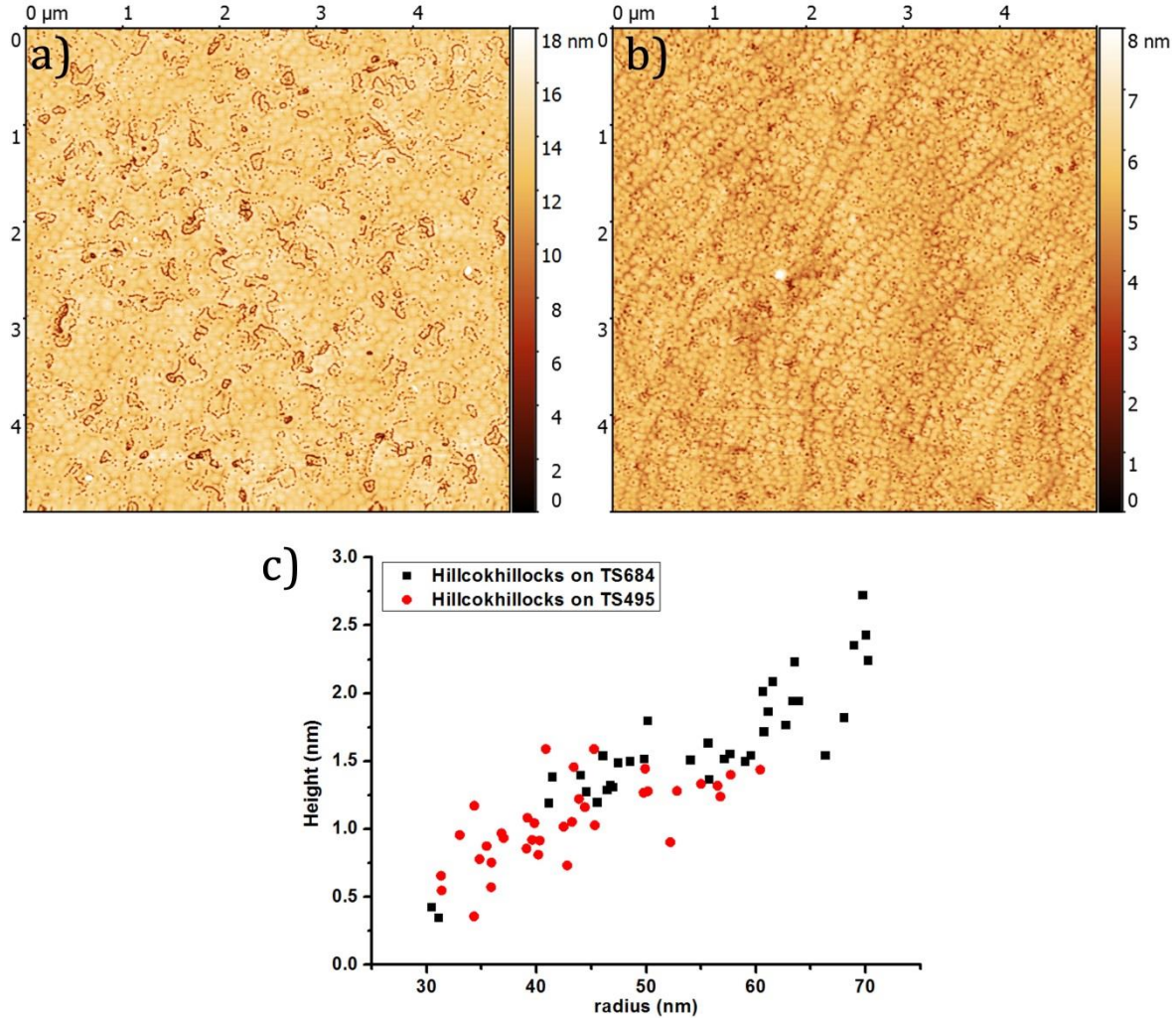

Figure 5.6: AFM of a) TS684 b) TS495 c) comparison between the geometrical extent of hillocks without pinholes for these two samples.

Figure 5.7 shows the surface morphologies of TS496 and TS497 for which the growth pressure was 100 Torr and 120 Torr, respectively. The roughness is 1.5 nm and 1.2 nm, respectively. As can be seen, the trend of forming smaller hillocks is maintained as the pressure goes higher until the surface shows only grains. On TS497, the radius of individual grains are less scattered, they have an average radius of 30 ± 2 nm.

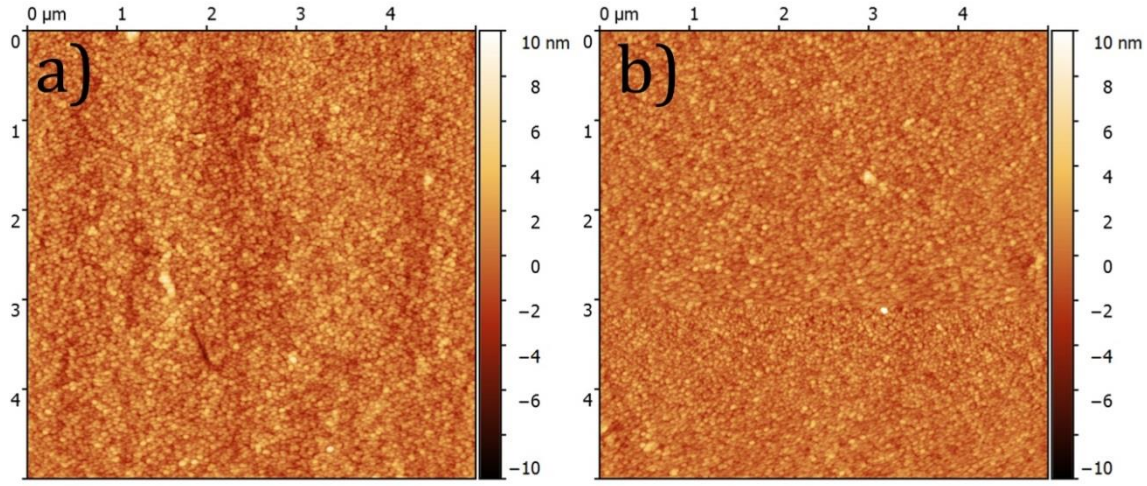

Figure 5.7: AFM showing the surface morphology of a) TS496 b) TS497.

The weak beam dark field images recorded with $g = 11\bar{2}0$ of figures 5.8a to 5.8d show representative regions from TS684, TS495, TS496 and TS497, respectively. All the TDs terminate as pinholes at the layer surface. Sample TS684 exhibits the highest dislocation density, with associated pinholes. In comparison to other layers, sample TS495 exhibits much less contrast between the GaN template and the quaternary layer, meaning that it is the least strained.

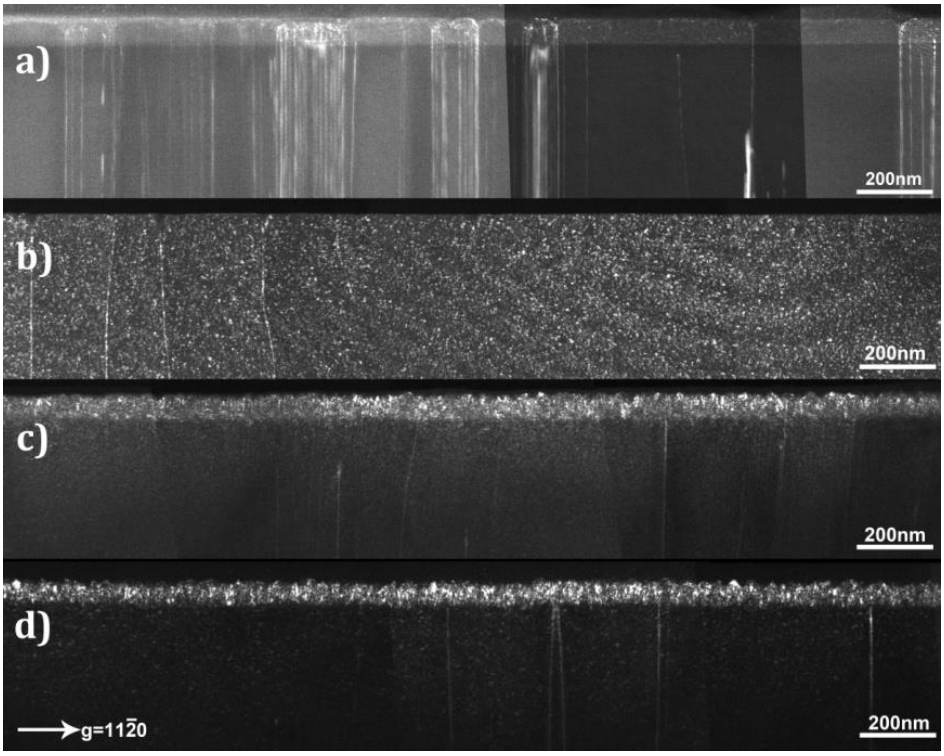

Figure 5.8: weak beam dark field micrographs of a) TS684 b) TS495 c) TS496 and d) TS497. The effect of increasing the growth pressure from 50 Torr to 120 Torr is reflected. At 80 Torr the layer is least strained. Higher growth pressure leads to an increase in the contrast indicating higher strain states.

For higher growth pressure, weak beam images exhibit high contrast features in these diffraction contrast images. As can be noticed, this effect increases considerably when going from 100 Torr to 120 Torr. Indeed, the surface roughness difference is also notable for these two samples. The abrupt changes in contrast in these images indicate local strain states. With the average measure composition, the calculated mismatch was the largest for these two samples TS496 and TS497, +0.4% and +0.6% respectively. They are thus under compressive strain, whereas, TS684 (-0.02%) and TS495 (-0.2%) are under tensile strain.

The first two samples share the same thickness (60 nm). They have both 15 % of indium content but not the same amount of gallium. TS684 contains more than twice gallium in comparison to TS495. With increasing the growth pressure, the indium content increases from 16% to 20%. Similar results were obtained by Reuters et al.[85] from 52.5 Torr to 200 Torr at 750 °C. For our samples, the gallium content increases but reaches a maximum of 12%. Therefore the incorporation of indium is easier at higher pressure which can be the cause of locally increasing the compressive strain in quaternary AlGaInN layers. Changing the strain state, by increasing the pressure was also reported by Cho et al.[130] who showed that from 100 Torr to 150 Torr, at 870 °C for quaternary layers, one can move from high compressive strain to tensile strain. In contrast, their layers were indium and gallium rich; the aluminum content was very small. The HRXRD measurement showed a pic shift from -436 arcsec to +108 arcsec and then at 300 Torr it was +210 arcsec for the same growth temperature.

Furthermore, we have observed that the surface morphology evolves from hillocks and visible pinholes toward grain features. This kind of roughening can be explained by the reduction of the diffusion length of atoms for higher values of growth pressure. This mechanism is also suggested by Cho et al.[130]. From the size and density of hillocks, we assess that an optimized growth pressure is around 50 Torr where individual hillocks are flat and terraces are larger

5.3. Summary

With optimized growth conditions, the TDs and IDs still generate extrinsic degradations. In this instance, surface morphology showing hillocks, pinholes and trenches was observed for 850 °C and a V/III ratio of 787 for ternary alloys. In quaternary alloys, the growth conditions are 875°C and V/III from 5000 and higher, up to 8900. The observed roughness is due to the low mobility of atoms at a low growth temperature. However, a very high pinholes density was observed on the ternary alloy comparing to the TDs density, meaning that the growth conditions are close to the best. As a further indication the composition fluctuation is still high around 10%, whereas for the growth conditions of the quaternary, it was dropped to 2% for all aluminum, indium and gallium contents. Further investigation of higher V/III ratio at the growth temperature of 875 °C showed almost no changes in the surface morphology. But increasing the growth pressure to 80 Torr and higher 120 Torr, led to significant reduction of the diffusion length of adatoms and thus grain features were dominating the surface morphology. Considering the size and shape of hillocks, they are largest in diameter and have flat tops at 50 Torr, thus, this pressure is considered as suitable for the growth of AlGaInN.

6 Inherent defects in AlInN & AlGaInN

In the following, we continue studying degradations of AlInN and AlGaInN. We focus on defects that form systematically in those alloys but that have other origins than TDs or IDs. Firstly, we will describe the explanations given by some groups who observed these intrinsic defects while studying AlInN and AlGaInN nearly lattice-matched. Secondly, our results will be presented. Finally, we will discuss the origins and the mechanisms of the inherent degradations.

6.1. Introduction

For HEMTs based on AlInN[131] or AlGaInN[27], up to 10 nm thickness is needed to obtain highest performances. And for heterostructures, such as Bragg mirrors, thicknesses exceeding 100 nm are needed[132]. While using optimized growth conditions, in order to achieve LMc, the thickness can be increased by such as extending the growth time. Nevertheless, it appears through the following literature, that keeping good quality thick layer is challenging. These alloys present rapidly a hillock surface morphology, as well as pinholes. Multiple mechanisms are proposed by several groups.

6.2. Results and discussion

6.2.1. Samples

In the following, ternary and quaternary layers are investigated for determining the origins of inherent defects on the layers while the thickness is increased. The ternary layers are under tensile strain, compressive strain and lattice matched. The thicknesses of these layers are between 100 nm and 336 nm. In chapter 5, we have observed that the growth conditions induce strong modifications on the surface morphology of nearly lattice-matched layers. In the following, the layers have different strain states with growth conditions optimized for the desired indium content thus our observations are not biased. The quaternary layers are nearly lattice matched with various compositions. The latter can be classified in 3 sets where the thickness of AlGaInN was changed from 5 nm to 200 nm. The atomic composition was varied by controlling the In/Al ratio. All other growth parameters were kept unchanged. For the following classification, we choose arbitrarily the aluminum

content as a reference. The first set has high aluminum content, typically above 72%. The aluminum content of the second set is around 67%-70%. For the third set, low aluminum content was measured below 65%. Table 6.1 gives the name of each sample along with the thickness and indicates the indium content for the ternaries and the Al/Ga/In compositions for the quaternaries.

	Samples	Barrier Thickness [nm]	Composition: Al/Ga/In % (mismatch %)
Ternary layers	A383	125	16 (-0.2%)
	A1363	336	19 (-0.1%)
	MD3156	125	32 (+1.6%)
SET 1	TS655	5	-
	TS654	20	**73**/12/15 (-0.1%)
	TS653	50	**79**/09/12 (-0.6%)
	TS652	100	**72**/11/17 (0.09%)
	TS742	150	**85**/07/08 (-1.3%)
	TS744	200	**79**/11/10 (-0.8%)
SET 2	TS238	75	**67**/12/21 (0.7%)
	TS241	100	**70**/11/19 (0.4%)
	TS242	150	**68**/12/20 (0.6%)
	TS243	200	**69**/12/19 (0.5%)
SET 3	TS571	8	**58**/20/22 (0.01%)
	TS572	20	**55**/22/23 (1.2)
	TS573	50	**62**/19/19 (0.6)

Table 6.1: Ternary and quaternary layers under investigation in this study. The thickness and the content of each barrier are reported

6.2.2. Effect of the layer thickness

In this first section, we are going to observe ternary and quaternary layers with different thicknesses. The evolution of the morphology and the microstructure are assessed for each alloy. The results are discussed at the end of this section.

a- AlInN

We can begin by looking back at A1583 (chapter 5 figure 5.1b). This ternary layer is 30 nm thick with 18% of indium. It is single crystalline and has a smooth surface topped with hillocks and pinholes. In this section, thicker ternary AlInN alloys A383, A1363 and MD3156 with indium content 16%, 19% and 32%, respectively are investigated. A383 and MD3156 are 125 nm thick. They are under tensile and compressive strain, respectively. A1363 is 336 nm and is under compressive strain.

In Figure 6.2a-c, topographies of A383, A1363, and MD3156 are displayed respectively. As can be seen in Figure 6.2a, for A383 while compared to A1583 the hillocks and pinholes morphology can be maintained with a roughness of 0.5 nm for the 125 nm thick layer. We notice clearly pinholes with different sizes. Based on our study from chapter 4, these are not connected to dislocations. Figure 5.1b shows the surface morphology of the thickest barrier but nearly lattice matched A1363. In this case, the roughness is equal to 3 nm. In this case, grains are observed without observable pinholes or hillocks. Similarly, figure 5.1c shows the case of MD3156 for which the thickness is similar to A383 but with higher indium content. The roughness is equal to 6 nm.

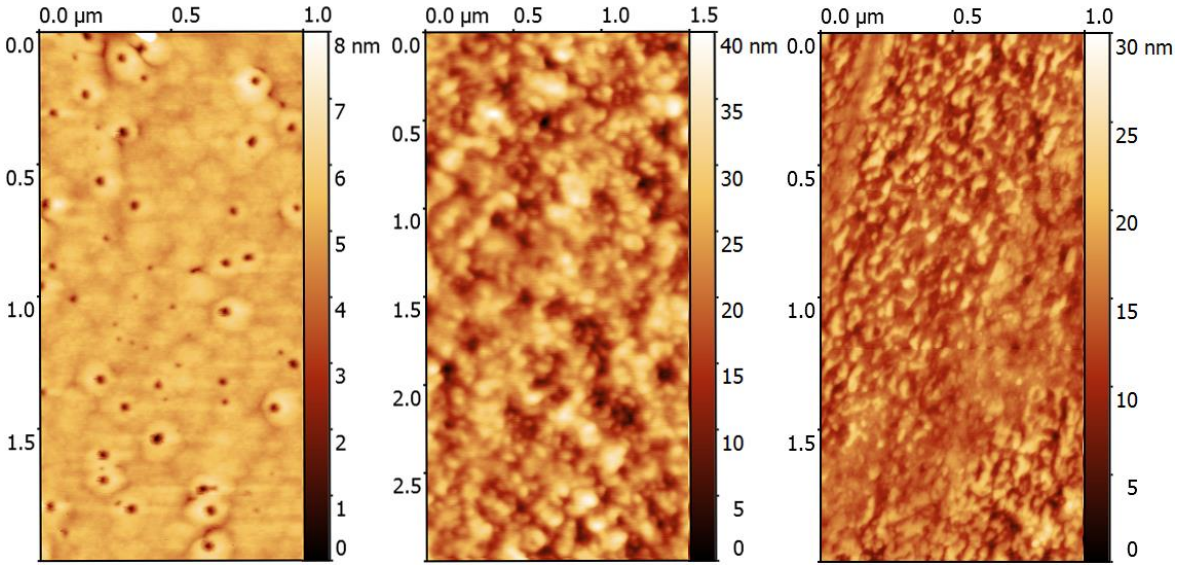

Figure 6.2: Evolution of the surface morphology for layers with different strain state and thicknesses. Shown here are a) A383 b) A1363 c) MD3156

Figure 6.3a-c shows the microstructure of each A383, A1363, and MD3156, respectively. All micrographs were recorded with the same g = 11-20. For A383, at this scale, uniform contrast is observed indicating a good crystalline quality. One TD is at hand that opens in a pinhole. The slight change in the contrast inside this pinhole can indicate an average different orientation or a different local composition leading to a different strain state. It is worth noting that the doubled contrast at the interface AlInN/GaN and near the vacuum is due to the tilt in the microscope.

Figure 6.3b shows that for A1363, the diffraction contrast is not uniform. This contrast can be decomposed as follows. Uniform regions mostly close to the interface are randomly distributed. Not uniform regions that can start at any depth along the

growth direction without any visible connection with TDs or other defects. The contrast changes can indicate local composition changes or different orientations and thus different strain states. For this sample, we do not observe a uniform thickness after which degradations are initiated.

In comparison, MD3156 presents a visible polycrystalline microstructure as can be seen from the various moiré fringes in figure 6.3c. We have already observed this layer and stated that the GaN has a low TDs density. In this case, with the highest indium content, the layer is defective from the beginning at the interface.

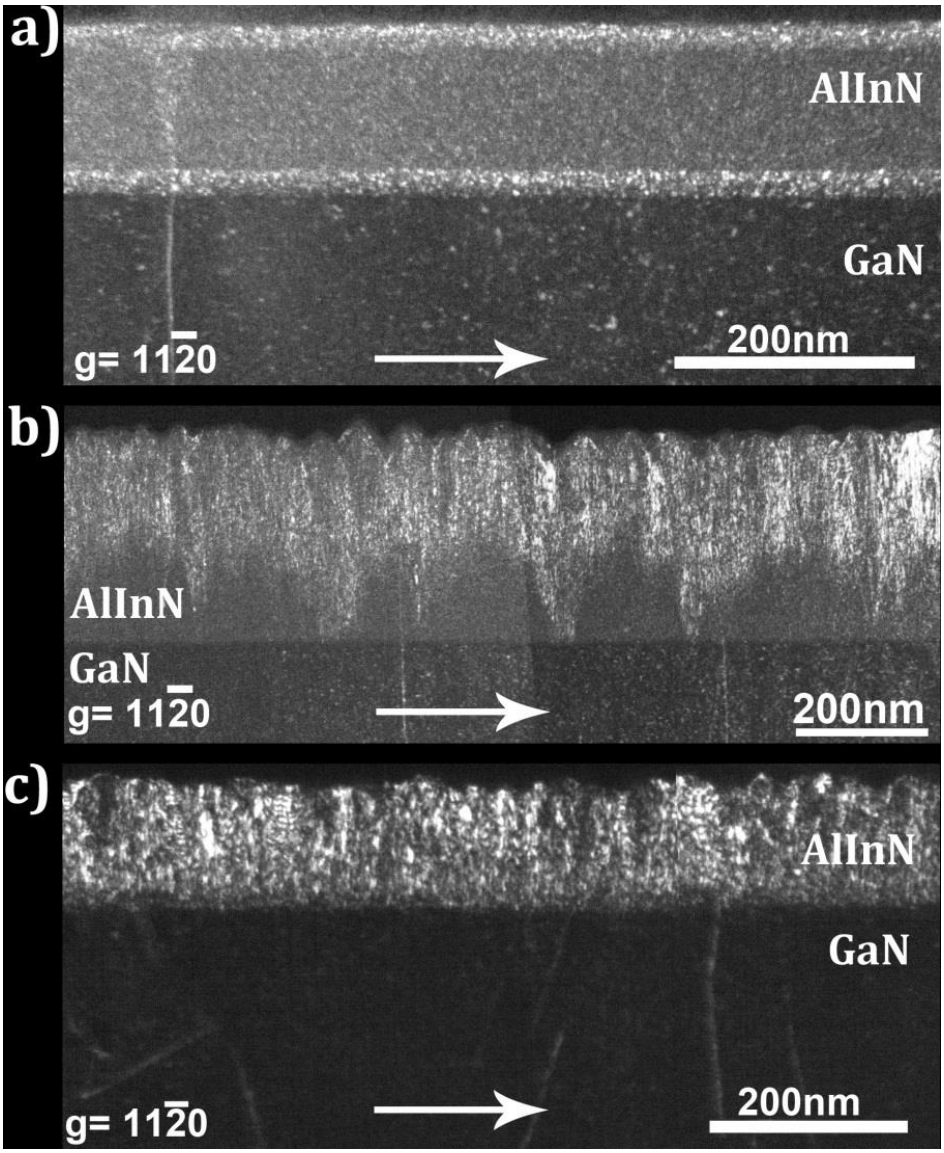

Figure 6.3: Weak beam dark field micrographs were recorded with g= 11-20 for a) A383, b) 1363 and c) MD3156. Clearly, the microstructure does not only depend on the TDs but also on the thickness and the strain state.

In order to investigate strain relaxation mechanisms in AlInN with different strain states (A383 125 nm thick 16% In) MD3156 (125 nm 32% In) were prepared for plan view investigations. The results are displayed in figure 6.4a-b, respectively. The investigated regions are at the interface between the layers and the GaN buffer. In contrast to other nitride alloys, namely AlGaN and InGaN misfit dislocations are formed at the hetero-interface to relax the inherent compressive and tensile strain while grown on GaN. For AlInN, we did not observe misfit dislocations at the hetero-interfaces. The diffraction contrast plan views near <11-23> zone axis of figure 6.3 show only TDs going through the layers thickness.

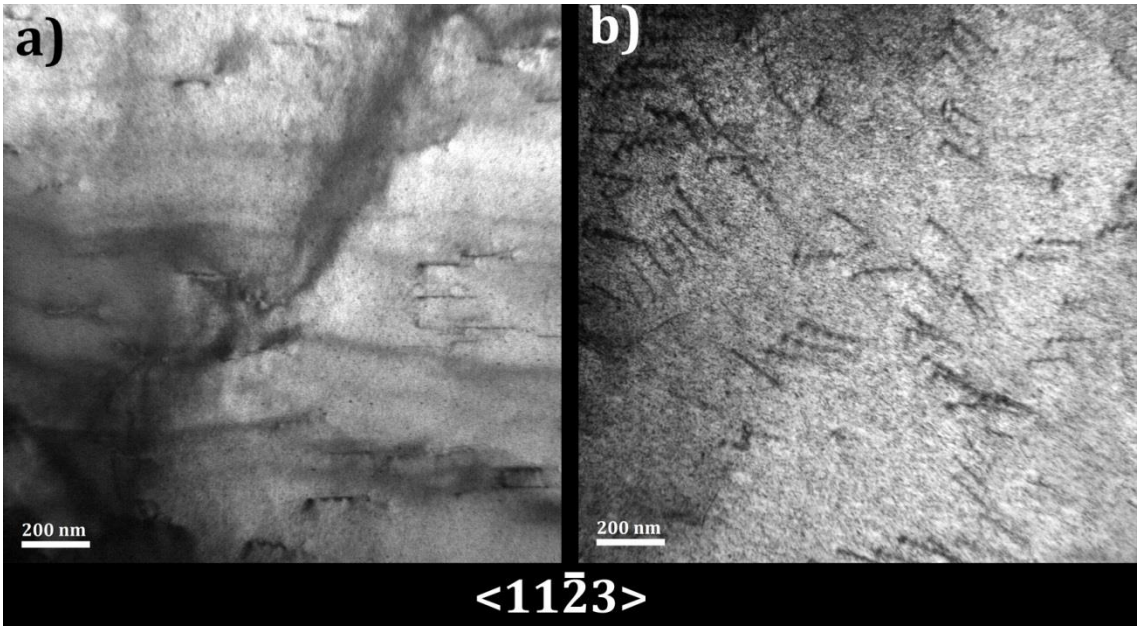

Figure 6.4: Plan view micrographs of a) A383 and b) MD3156. No misfit dislocations are observed

b- <u>AlGaInN</u>

Quaternary layers have been classified into three groups depending on their average composition that we have measured by EDS as reported already from table 6.1. Figure 6.5 shows the EDS measurements that we performed. The dotted red line shows the lattice match condition to GaN. This line expresses the possible compositions that are lattice matched to GaN given by Vegard's law without bowing. On the left of the red line, samples are under compressive strain and samples to its right are under tensile strain. As shown in table 6.1, all the layers are nearly lattice matched in the range of ±1%.

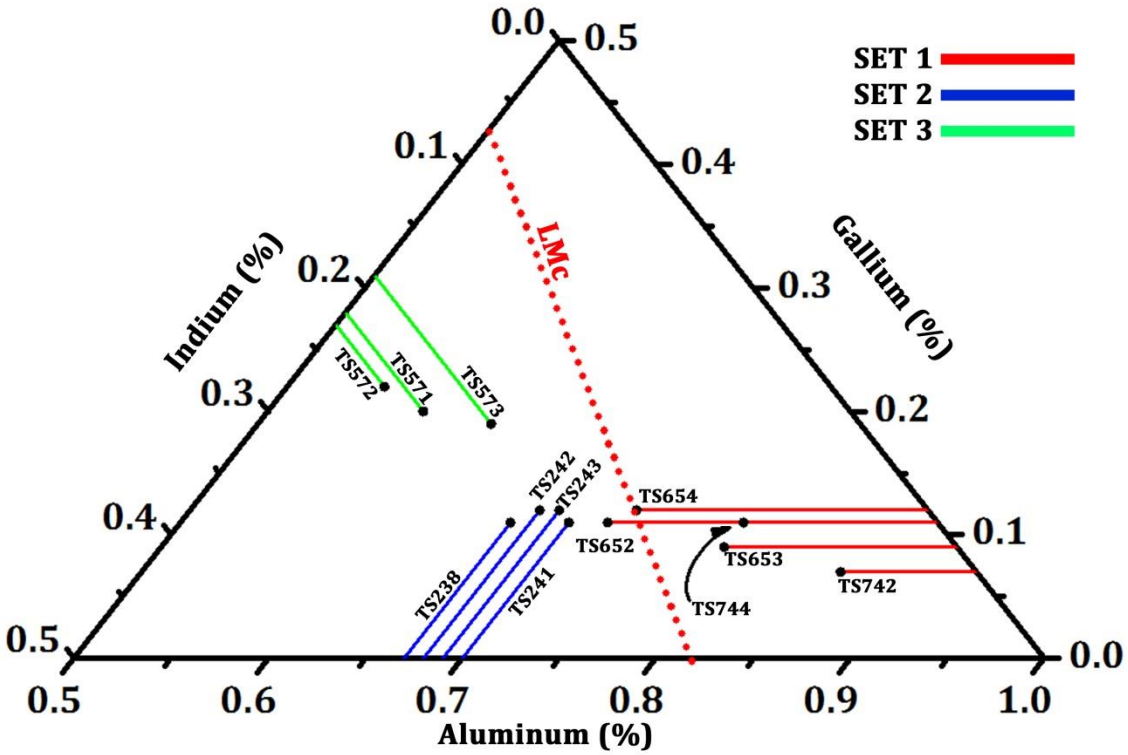

Figure 6.5: Classification of the quaternary layers regarding their average atomic composition retrieved from EDS. The red line shows the possible compositions for obtaining lattice-matched layer to GaN.

The average roughness of each layer was investigated and the result is plotted in figure 6.6 with respect to the barriers thicknesses.

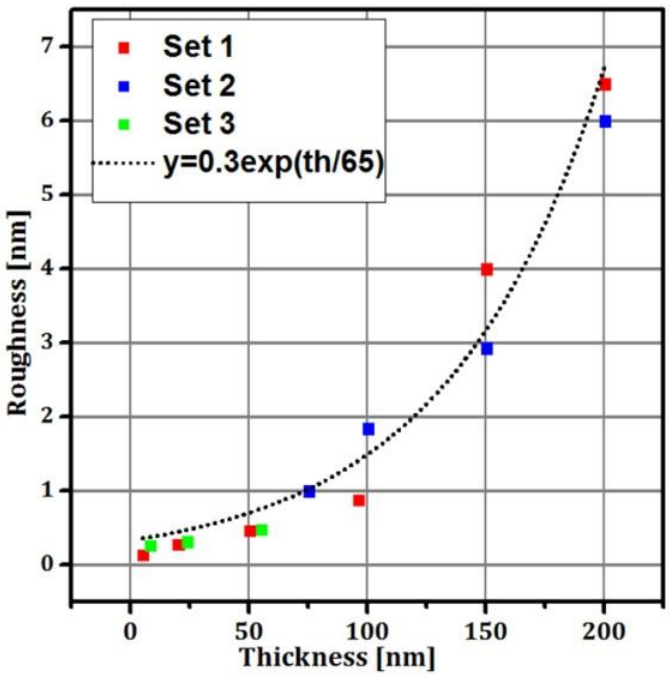

Figure 6.6: Average roughness of quaternary layers. This quantity increases rapidly while the thickness is increased.

As can be seen, when the thickness increases, the roughness increases exponentially. Let "Rq" and "th" be the roughness and the thickness both in [nm], respectively. The following equation was used to fit the obtained data: $Rq = 0.3 \times e^{\frac{th}{65}}$. 0.3 nm is in fact, the average roughness of the GaN template[72]. The surface morphology of the thinnest layers TS655 (5 nm) and TS571 (7.8 nm) are displayed in figure 6.7a-b respectively. We still see the growth steps generated by GaN. In addition, small grains are already covering the surfaces and following the growth steps. The roughness is 0.15 nm for TS655 and 0.25 nm for TS571. The latter shows fewer pinholes than on TS655 but all have the same size around 15 nm in diameter. Therefore, it is hard to tell from AFM only if they are connected or not to TDs. The two morphologies are very close but in addition, there are probably indium droplets visible on the surface of TS571 (20% of indium content). This is probably due to the higher TMIn flux. For these two layers, the roughness is very close to the roughness of the used GaN.

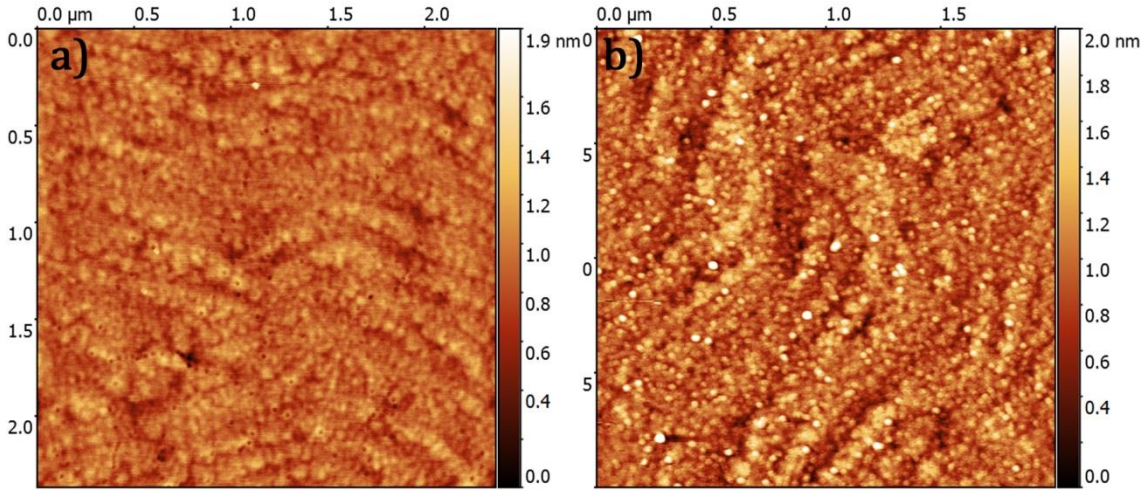

Figure 6.7: Surface morphology of the thinnest quaternary layers a) TS655 from set 1 and b) TS571 from set 3.

The surface morphology of TS654 (20 nm) and TS572 (25 nm) are displayed in figure 6.8a-b, respectively. Close morphologies are observed. For both samples, the roughness is around 0.3 nm. In addition, the two layers have pinholes with an average diameter around 20 nm is measured. These pinholes are not connected to TDs. All other pinholes are 30 nm in diameter and based on our previous analysis these are connected to TDs. In addition, we see clearly hillocks 2 times bigger on TS572 than on TS654. They are around 120 nm in diameter.

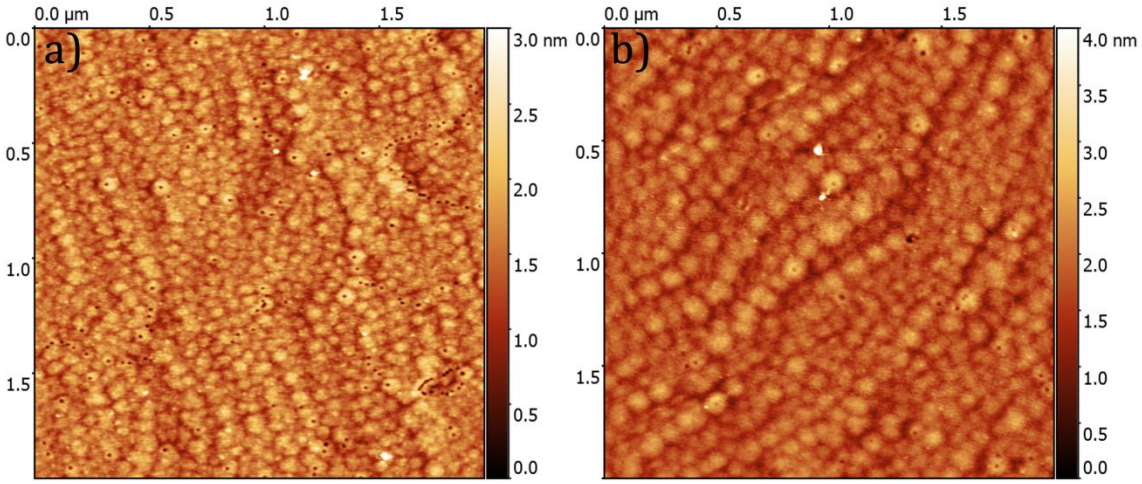

Figure 6.8: Surface morphology of the 20 nm thick quaternary layers a) TS654 from set 1 and b) TS572 from set 3.

The morphology of TS653 (50 nm) and TS573 (55 nm) are displayed in figure 6.9a-b, respectively. The roughness is the same 0.6 nm but the density of hillocks is higher for TS653 thus they are smaller. The shapes of the hillocks begin to have facets and a flat surface for both samples with no pinholes in the coalescence regions.

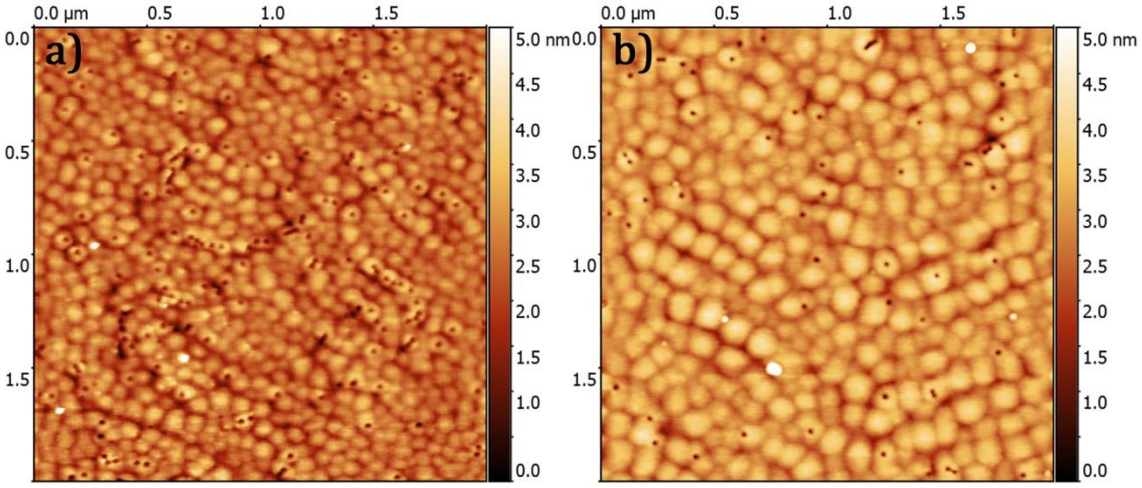

Figure 6.9: Surface morphology of the 50 nm thick quaternary layers a) TS653 from set 1 and b) TS573 from set 3.

Increasing the thickness until 150 nm shows the same features on the layers as displayed on figure 6.10a-b for TS742 and TS242, respectively. The roughness of the former is 4 nm and the latter is 3 nm. The hillocks on both samples have a flattened top with very clear facets. Some of them are almost hexagonal. As usual, pinholes are not systematically on their tops. The diameter of hillocks is around 94±2 nm for TS742 whereas it is around 111±3 nm for TS242.

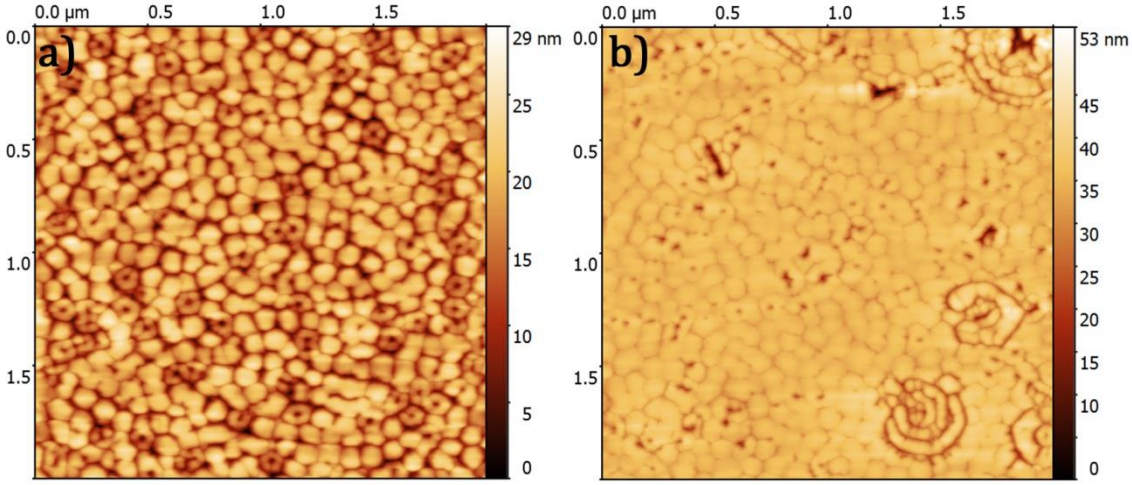

Figure 6.10: Surface morphology of the 150 nm thick quaternary layers a) TS742 from set 1 and b) TS242 from set 2. The usual surface morphology with hillocks (note the facets and smooth tops) and pinholes is still visible. The hillocks have facets and almost hexagonal shapes.

In the two thickest samples (200 nm – figure 6.11), there is a clear transition toward a grain-like surface morphology for both TS744 and TS243. Nevertheless, some pinholes are still visible only on TS744. The second layer is completely covered with grains. The average diameter of these grains is 109±3 nm for TS744 whereas it is 125±4 nm for the second layer. The average roughness is 6.5 nm and 6 nm, respectively.

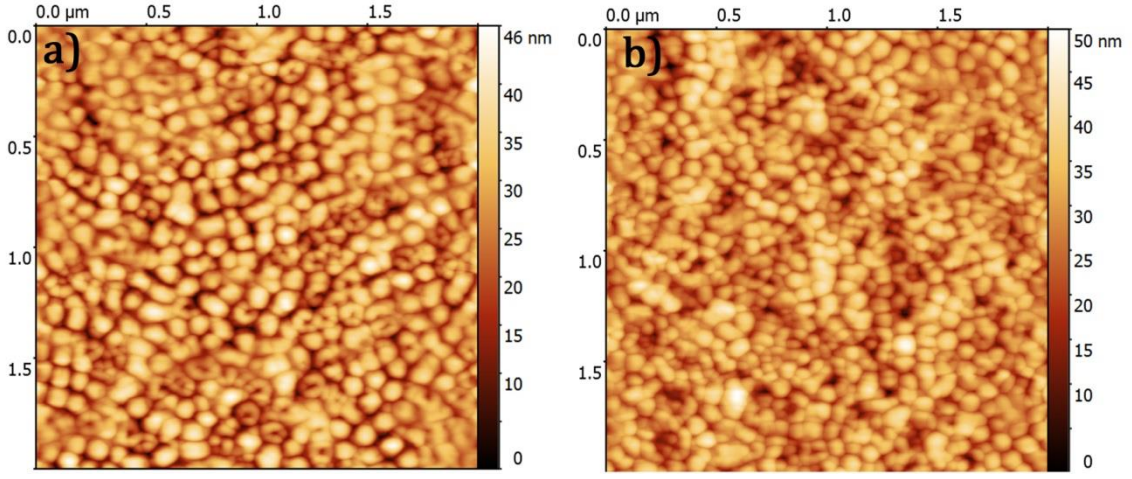

Figure 6.11: surface morphology of the 200 nm thick quaternary layers a) TS744 from set 1 and b) TS243 from set 2. A transition from hillocks (with facets and smooth tops) to grains has occurred when the thickness was increased from 15 nm to 200 nm.

As we have observed a transition in the surface morphology between 150 nm and 200 nm, in the following we restrict our TEM observation to the last four samples. Figure 6.12a-d show representative regions of TS742 (150 nm), TS242 (150 nm),

TS744 (200 nm) and TS243 (200 nm), respectively. In all of the four samples, the only dislocations are TDs which open in pinholes, whatever the diffractions conditions. There are no misfit dislocations or stacking faults in quaternary layers. The roughness can be observed from these small regions. Similarly to the contrast observed in ternary layers, the defective regions do not start at a fixed depth. The bright contrast can indicate small disorientations or indicate local composition and thus different strain states.

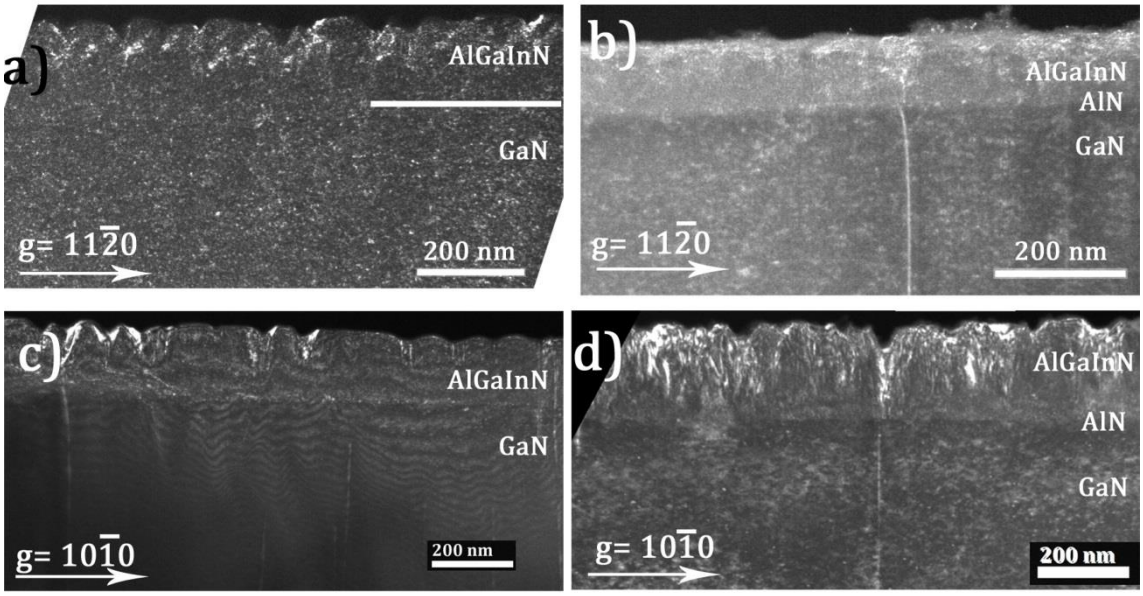

Figure 6.12: Weak beam dark field micrographs taken with g= 11-20 for a) TS742 and b) TS242 and with g= 10-10 for c) TS744 d) TS243. No misfit dislocations or stacking fault are present in quaternary layers.

c- ***Discussion***

In the case of nearly lattice-matched ternary AlInN layers; the surface quality can be maintained for thicker layers from 30 nm to 100 nm with optimized growth conditions. In such layers, pinholes not connected to TDs and hillocks remain visible. In contrast, Miao et al.[30] observed pinholes not connected to TDs only for 200 nm thick $Al_{0.77}In_{0.23}N$ under compressive strain and used stacking faults inducing stacking mismatch boundaries at their apex as one possible mechanism for their formation. In our case, such mechanism was not observed in compressively strained layers. Furthermore, we observed that the surface morphology cannot be maintained as soon as the thickness is increased from 100 nm to 336 nm or the strain state is strongly changed. The topography evolves from pinholes and hillocks toward grain features. In addition, from our TEM observations, there is no critical thickness beyond which

degradations are observed. In contrast to this, Chen et al.[29] reported that for nearly LM AlInN by increasing the layer thickness from 136 nm to 610 nm a critical thickness of 250 nm - 300 nm beyond which dislocations open in pinholes.

Furthermore, Perillat-Merceroz[121] proposed that the degradation mechanism leading to the formation of pinholes is triggered by the anisotropic growth on the facets generated during the coalescence of the hillocks as no TDs were present in such FS-GaN substrates. Thus all pinholes are found in the coalescence regions of hillocks. And these characteristic features have been observed not only in LM ternary layers but also for alloys with 13% and 20% of indium composition, the authors concluded that they are probably intrinsic to the alloy and do not depend on the strain state. For both ternary and quaternary layers nearly lattice matched, the increase of the thickness leads to strong degradations with the appearance of pinholes not connected to dislocations. On our case, these intrinsic defects are not systematically found in the coalescence regions of hillocks.

Thinner layers have already small hillocks with a 5 nm in diameter approximately. This indicates a 3-dimensional growth (3D) mode from the early stages of the growth (5 nm thick layers). In the literature such as the work of Liu et al.[133] and Reuters et al.[85], a 2D growth is observed for quaternary layers with low indium and/or aluminum content. In our study, for the layers with higher indium/aluminum contents a 3D growth is systematically observed.

Then, as soon as the thickness reaches 50 nm, the individual hillocks begin to have clear facets. We have observed that the hillocks of set 1 have the smallest grains, these layers have the highest aluminum content (>75%). This can be explained by the fact that a growth temperature of 875 °C is not enough to achieve good aluminum incorporation at these high concentrations. Here the mobility of aluminum atoms is not enough to obtain flattered hillocks.

More visible, the hillocks present facets and platelets between 100 nm and 150 nm. The pinholes are still smaller than 100 nm in diameter. The shape is almost hexagonal. From the TEM observations, also for these quaternary layers, there is no critical thickness beyond which the layers begin to deteriorate as previously reported[29,134]. Moreover, we did not observe such as stacking faults or misfit

dislocations as suggested by other groups[30,135]. In our case, other mechanisms are clearly involved in order to explain the strain relaxation and the degradation of nearly lattice-matched ternary and quaternary layers.

6.2.3. Origins of the inherent degradations

In the previous chapter, we saw that there is a fluctuation of the aluminum and indium content which can be reduced to 2% with optimized growth conditions. For the gallium content, the average fluctuation is always around 2% as measured by EDS. In this section, we investigate more carefully these fluctuations in order to determine their origin and its effect on the alloy. We focus now on sample A1363 for which the average indium content is 19%. The following HAADF micrographs are recorded with 6 cm camera length near a $< 10\bar{1}0 >$ zone axis.

Figure 6.13 shows a high angle annular dark field image of the AlInN/GaN interface area. As can be seen, the black arrows point to a number of areas which are probably spherical and exhibit a brighter contrast than their surroundings. They have dimensions of 5 nm - 10 nm and some.

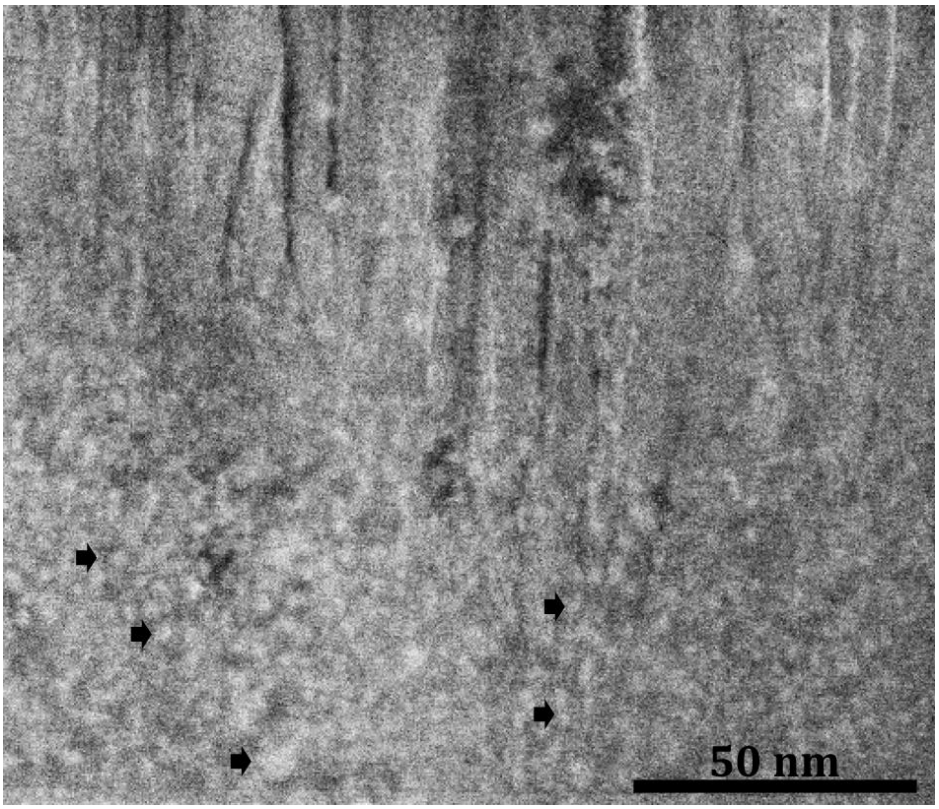

*Figure6.13: HAADF micrograph recorded with 6 cm camera length showing different **Z**-contrast near $< 10\bar{1}0 >$ zone axis. This region is taken near the interface AlInN/GaN.*

These spots show an average composition of 35% of indium whereas; the darkest areas can exhibit indium content as low as 11%.

Moreover, as can be seen in figure 6.14, columnar features also start to form and some are in connection with the bright spots (#1).

In such narrow dark columns, we measure the minimum indium composition below 11%, however due to the detection geometry of EDS analysis higher values can also be obtained. As clearly seen, they may originate from highly indium-rich spots (38%). Indeed, it can also be noticed that the indium-rich regions are surrounded by aluminum-rich columns.

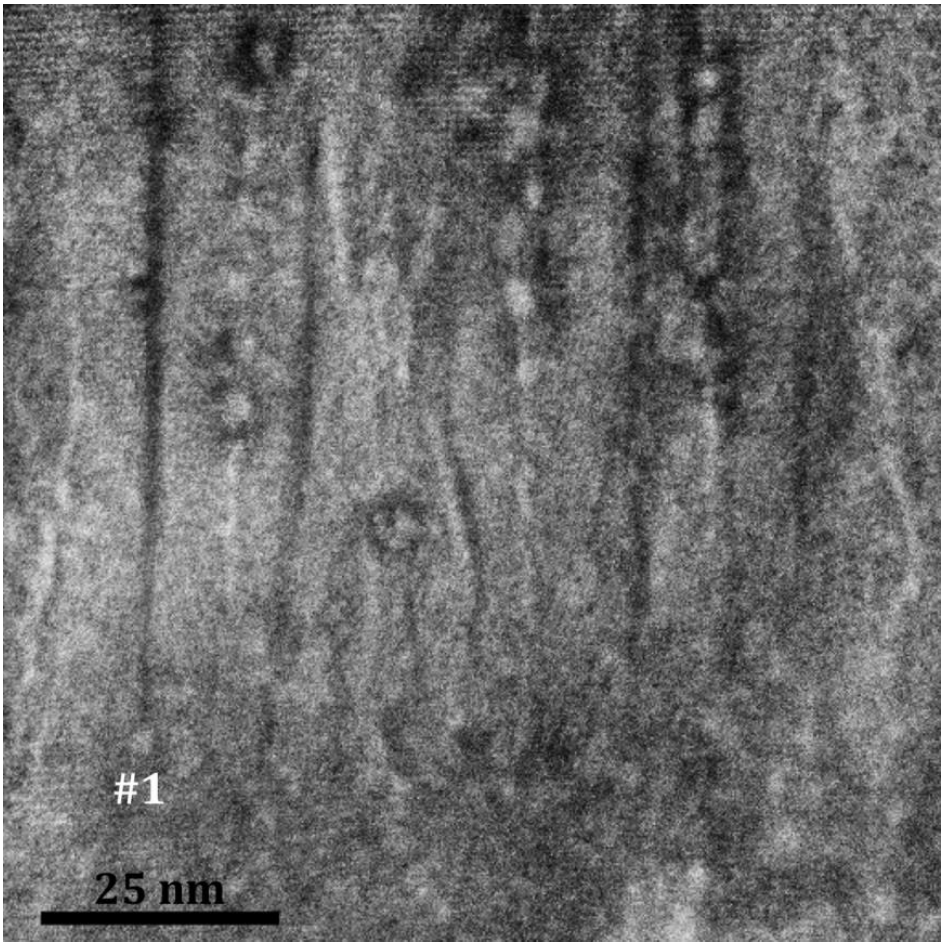

Figure6.14: HAADF micrograph recorded with 6 cm camera length showing different z-contrast near $< 10\bar{1}0 >$ zone axis. This region is taken near the top surface.

For the same purpose, thinner layers were investigated. EDS measurements were performed on TS571 near <0001> (from a plan view sample preparation). The spectra were recorded in the thinnest parts of the layer in order to minimize the GaN contribution. As can be seen, the gallium content stays within 2%, whereas the

average Al/In ratio may be around 2.4. This is taking place even inside layers (fig. 6.15)

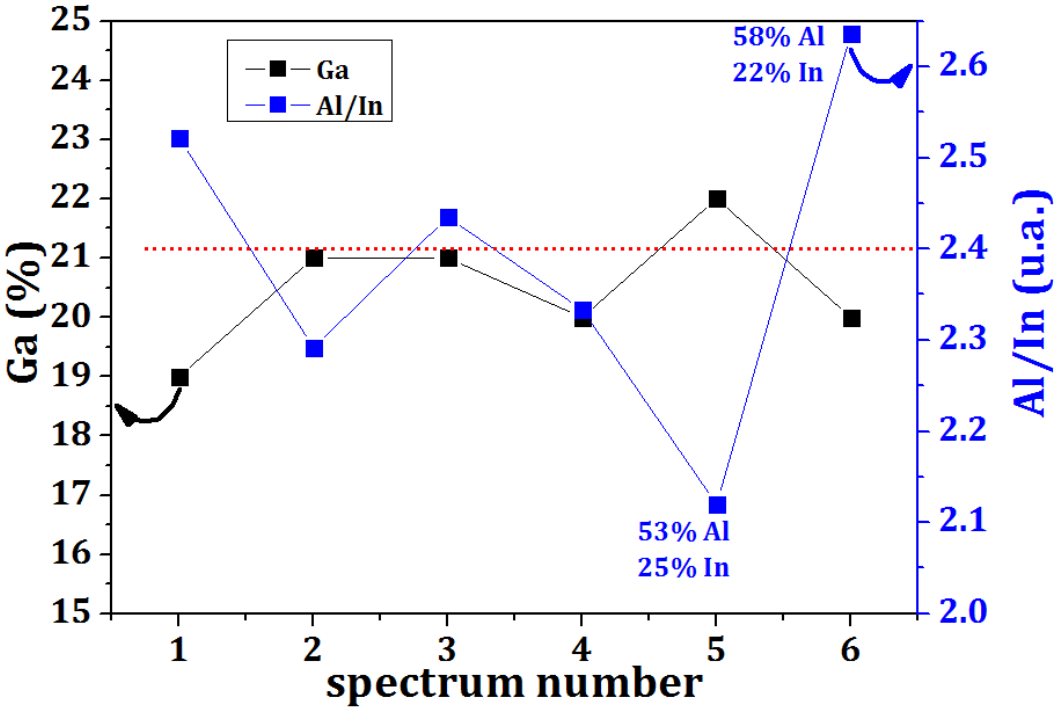

Figure 6.15: EDS obtained for TS571. The gallium content is constant. The interplay is observed between Al and In.

To complement these results, atom probe tomography was performed on TS241 (100 nm) on a large scale. Figure 6.16a shows the sum of the projected slices across 90 nm thickness. The radius of the investigated tip was 28 nm. Figure 6.16c-d shows the aluminum, gallium and indium concentrations respectively projected in a (x, y) plane of the same volume. The nominal composition given by the analysis is 82% Al, 7% Ga, 11% In. Whereas the EDS result is 70% Al, 11% Ga, 19% In. The deviation can be explained by the local aspect of the EDS measurement and indicates that the alloy composition is not uniform. The gallium map is less scattered across the investigated region. Some spots show 3% of gallium content, so, these are AlInN like regions. The indium distribution in Figure 6.16d shows a depleted column (3%). In this same region, the aluminum content is almost 90 % as shown in Figure 6.16b. This columnar region is AlGaN like.

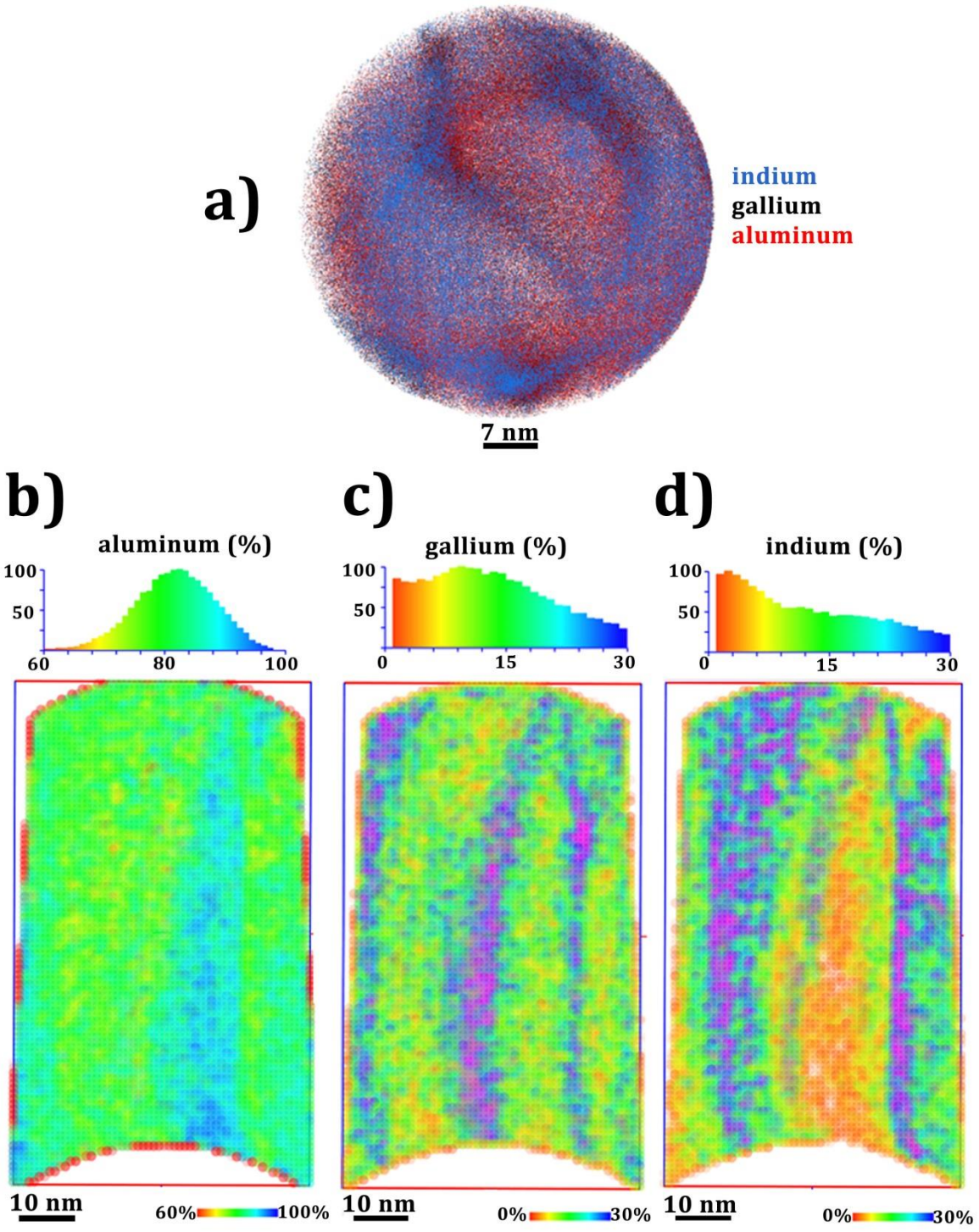

Figure 6.16: Atom probe tomography obtained on TS241 a) distribution of the metallic atoms in the investigated needle. b)-d) the projected distributions of each species: Al, Ga and In, respectively across the needle (Courtesy to Dr. Rigutti, L. GPM, University of Rouen).

Discussion

For an MOVPE process, atomic scaled composition fluctuation is rarely assessed in the literature. In this instance, XRD measurement by Yamaguchi et al.[136] concluded

that increasing the indium content in AlInN from 10% to 51% leads to a broad peak and low intensity peak. They finally concluded that AlInN in the investigated range of indium content is subject to phase separation with indium content fluctuations. In this instance, the phase diagram of AlN-InN mixing regions was theoretically investigated by several groups[137,138]. It shows that the LMc at 18%-19% of indium content in the ternary is at the edge of the spinodal decomposition slope. Therefore, the LMc is between metastable and unstable region at typical growth temperature. In comparison to AlInN, quaternary layer AlGaInN have also immiscibility gaps but these regions are narrow[139–141]. From the phase diagram, it exists regions of compositions where the quaternary can be lattice matched in the stable/meta-stable region. An example of a phase diagram is given in the following Figure 6.17. The cross shows the lattice match condition at 875 °C located within the unstable region below the spinodal decomposition curve (dashed curve)

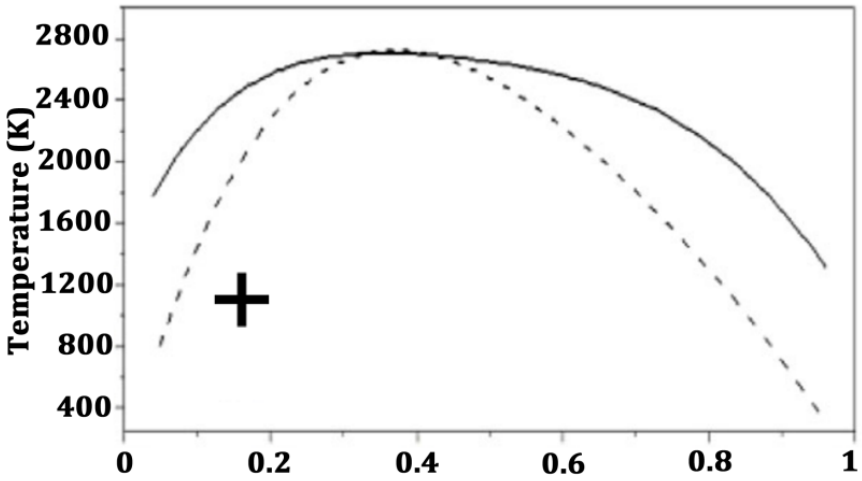

Figure 6.17: typical phase diagram showing the mixing regions of AlInN in the whole composition range of indium[142]. The critical temperature for AlInN is 2717 K, e.g.: The maximum of the spinodal curve stable mixing region is above the binodal curve (continuous line). Below the spinodal curve (dashed curve) the alloy is subject to phase separation. Between the two curves is the metastable region.

In the case of the work by Hums et al.[19] from XRD, only above 50% of indium in AlInN grown at 550 °C showed phase separation. In addition, Wei et al.[134] studied $Al_{0.82}In_{0.18}N$ layers grown at 800 °C with 140 nm - 500 nm thickness and concluded that the phase separation and the formation of pinholes responsible for layers degradations are triggered by the presence of screw TDs from the GaN buffer layer. In our case, the phase separation is observed even for nearly lattice matched ternary

and quaternary layers without connection to dislocations. Furthermore, we demonstrate local fluctuations for these nearly lattice-matched layers from the early stages of the epitaxial growth. These fluctuations begin with an accumulation of indium in 5 nm to 10 nm scaled cluster at the interface. We have observed that the amount of the fluctuation increases from a minimum of 2% to higher than 10% if the thickness is increased (from 75 nm and higher) or the alloy is intended to contain high indium content even for optimized growth conditions. As suggested by first principle calculation by Kandalam et al.[143], the mismatch between the bond lengths and their binding energies are encouraging the clustering of indium in a lateral and/or a vertical direction. For AlN, GaN, and InN the estimated bond lengths are 1.82 Å, 2.06 Å and 2.28 Å, respectively. For the binding energies, the latter author estimated the values to 2.74 eV, 2.45 eV and 2.08 eV.

As we saw in figure 6.13-6.14, indium or aluminum-rich columns start at various depths and propagate toward the layer surface. Some of these columns start with an indium-rich cluster and the column above is aluminum rich. In contrast to the formation of columns, the formation of individual pinholes not connected to dislocations can be explained as follows. Local clustering of aluminum atoms, such as we saw for the generation of pinholes rows around ID in chapter 3, lead to a region under tensile strain. In order to accommodate the strain, a pinhole is formed where the growth on the inclined facets requires less energy. Moreover, the accumulation of a certain kind of atoms will locally change the strain state; therefore the relaxation of the strain comes with balancing the local composition or accommodating the local crystal orientation or the formation of pinholes leading to phase separation and polycrystalline layers whenever the thickness is increased.

The phase separation is clearly observed by APT. As was predicted, by Marques et al.[144], AlGaInN, at the growth temperature of 800 °C, should present phase separation and InGaN and AlGaN like regions would coexist. From the phase diagram[145,146] of a ternary layer, the LM is at the limit between the metastable and unstable regions at the usual growth temperatures. Therefore, during the cooling down to room temperature, the alloy evolves in the unstable region. The observed degradations are connected to the possible phase separation. For the quaternary layer AlGaInN the immiscibility gaps regions are narrow[139–141]. From the phase

diagram, regions exist where the alloy can be grown in a stable composition. Typically, near the AlGaN phase because it has the lowest critical temperature. Mohamad et al.[142] obtained theoretically these values 177 K for AlGaN, 1718 K for InGaN and 2717 K the highest for AlInN. Therefore, AlGaN is stable in the whole range of aluminum composition and only AlInN and InGaN are subject to spinodal decomposition at typical growth temperatures[147]. In our case, we saw that the distribution of the metallic atoms is not random. In our case, the ternary shows almost AlN and InN regions and columns. On the other hand, the quaternary shows nearly AlGaN and InGaN columns. These columns are around 10 nm to 20 nm width. Our experiment is in agreement with the observations of the recent work of Rigutti et al.[148] in 2017 who used APT on AlInN LM to gallium with a nominal composition of 18% of indium. The result showed 3D atomic distribution that consisted of columnar cells of 10 nm lateral dimension.

6.3. Summary

In this analysis, we have pointed out that inherent defects appear for nearly lattice layers probably due to an intrinsic 3D growth mode from the early stages of the epitaxy. This is most certainly due to phase separation as an intrinsic mechanism to relax the strain. This occurs at the expanse of the final layers quality that generates grain features at higher thicknesses. The surface morphology and the crystalline quality rapidly degrade as the thickness is increased.

7 Characterizations of HEMTs

In this chapter, we summarize the contribution of TEM characterization of several parts of the HEMT devices carried out within the LHOM ANR-project. They concern our follow up of 1) the optimization of the SiN passivation layer, 2) investigations carried out on the first devices of the project which were micron size gate HEMTs, the aim was to monitor the uniformity of this most sensitive part of the HEMT (gate), 3) the progress toward the objectives of the project by reducing of the gate dimensions and optimizing of the ohmic contacts.

7.1. Introduction

In the last two decades, significant efforts have been devoted in the world to the research and development of AlGaN/GaN High Electron Mobility Transistor (HEMT) technology[149]. Key application demonstrators based on AlGaN/GaN materials showed a breakthrough in the field of RF emission/reception functions[150,151].

In the telecommunication market, GaN-based HEMTs are now ready to challenge Si and GaAs based devices showing significant power performance improvements, and allowing the simplification of power amplifier system architecture[1].

HEMTs based on quaternary AlGaInN/GaN [152] can have an electron mobility up to 1800 $cm^2.V^{-1}.s^{-1}$ at 300 K with a 2DEG density around 2×10^{13} cm^{-2}. Such outstanding performances are attained by optimizing the AlN spacer introduced at the barrier-GaN interface which helps the 2DEG confinement[116].Thus, performances of AlGaInN/GaN are predicted to achieve better characteristics than AlInN and AlGaN[24,27] with a low leakage current[28]. In this frame, lattice matched and low defect density AlInN and even more importantly AlGaInN are very attractive material, as compared to the conventional AlGaN, for electronics devices.

However, next improvements in GaN-based High-Electron Mobility Transistors (HEMTs) are limited by the physics of already established AlGaN/GaN heterostructure system. The AlInN and AlGaInN materials are foreseen as a promising approach for such high-frequency applications on SiC substrate. Indeed, the way to improve the GaN device frequency performance consists in reducing the gate length "Lg" while keeping a high aspect ratio between Lg and the gate to channel distance

“a”; which should be well beyond a factor of 5[131]. However, reducing the barrier thickness which is related to “a”[24,153] or performing a gate recess[131] lead generally to a strong degradation of the two dimensional electron gas (2DEG) carrier concentration resulting in poor device performance due to the surface charge effects and/or high gate leakage current[154]. If the gate leakage current is controlled, this would allow taking advantage from deeply sub-200 nm gate length “Lg” and therefore operate the device at higher frequencies.

Notwithstanding the extensive on-going research efforts, AlInN/GaN HEMTs still suffer from high leakage current under high bias, which is attributed to a surface parasitic conduction under high electric field[155]. The physical origin of the leakage in such heterostructures needs to be understood to overcome this major limitation and allow a new generation of high power mm-wave devices. Furthermore, the determination of surface properties will also be a key for optimum device operation and proper passivation is certainly needed to avoid a surface parasitic conduction. The deposition of a passivation layer can reduce the effect of this kind of degradations. Typically, the passivation layer is a thin layer of SiN.

In HEMTs, several parts are critical to achieving highest performances. During our work, we have contributed to the characterization of the AlN interlayer, the different contacts and the SiN passivation layer.

7.2. Results and discussion

The general structure of the devices that we have contributed to characterize is depicted in figure 7.1a. In this example, the gate length is L_g= 3µm. In a final device, the number of gates can be as many as needed for a particular application[156] and sources are connected by bridging over the gates[157]. Figure 7.1b shows a typical cross section of a HEMT structure. While seeking for the best performances, SiC substrates were used for several reasons such as its high thermal conductivity as previously discussed. SiC is then followed by an AlN nucleation layer. The GaN buffer layer thickness is typically around 2 µm and an optimized AlN layer is inserted at the interface AlInGaN/GaN. After the growth of the heterostructure, comes few nanometers of SiN passivation layer and the contacts are processed. The main parts that were optimized during the project are highlighted as well.

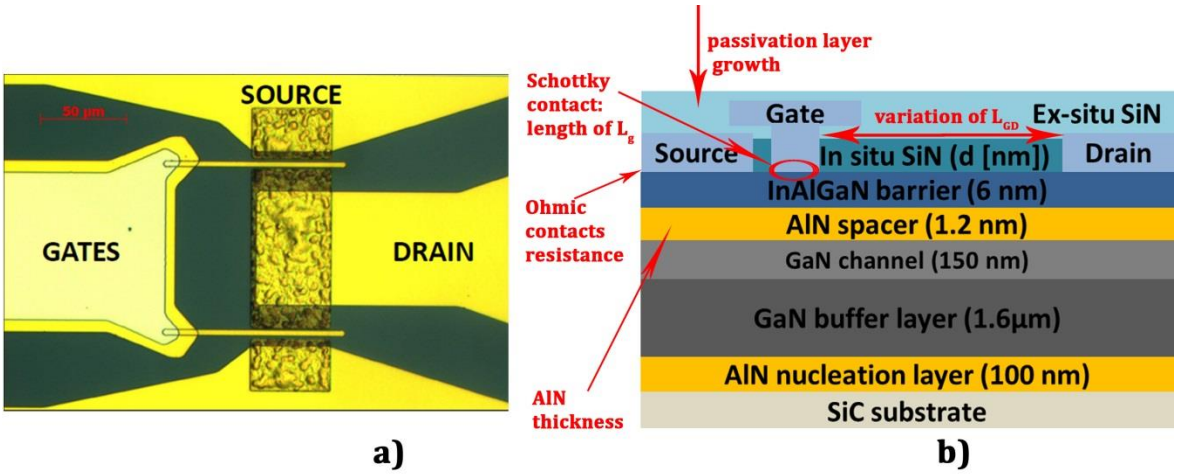

Figure 7.1: a) Top view of a HEMT structure with two gates (colored optical micrograph) b) Cross-section representation showing the stacking *with typical thicknesses. The main device optimization areas are shown.*

7.2.1. Contacts optimization

The metallic stack that has been used was Ti/Al/Ni/Au for the drain and source. The diffusion of these metals toward the barrier has to reach the 2DEG forming a good ohmic contact. Thus, in HEMTs, also called field effect transistors, the source and drain are electrically connected via the 2DEG. These metallic contacts are ohmic in nature and should have the lowest resistance. To attain this property, a rapid thermal annealing was achieved at 875 °C.

The transistor behavior is achieved by the control of the current that flows between the source and the drain via the gate. The gate is a Schottky diode structure where a Ni/Au stacking is deposited. In order to avoid damaging the 2DEG, the annealing of this contact is not possible. Therefore, the ohmic contacts are processed prior to the gate.

First generation

a- Ohmic contacts

Optical lithography is employed to define the the ohmic contacts, after the SiN has been firstly etched by Ar plasma.. Before the TEM analysis, FIB sections were prepared along the contacts. A representative region next to the drain contact is investigated in figure 7.2. As can be seen, the annealing process of the ohmic contact (Ti/Al/Ni/Au) lead to the formation of multiple phases with regions Au-rich and Ni-

Al-rich. The larger diffusion areas inside the barrier are made of gold-rich areas, which appear to be through the threading dislocations.

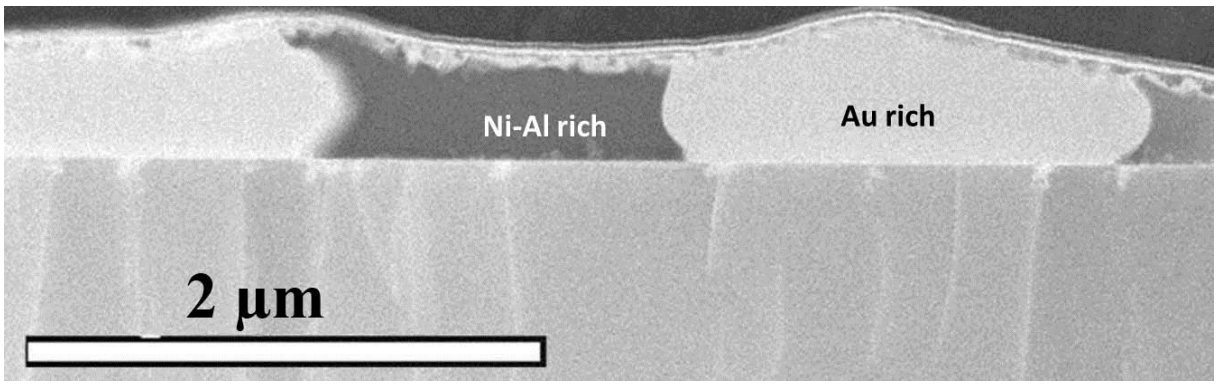

Figure 7.2: ADF of conventional ohmic contact. Multiple metallic phases are observed with gold-rich regions and Ni-Al rich regions.

At higher magnification, as can be seen in figure 7.3, the metallic part at the interface is made of small crystallites.

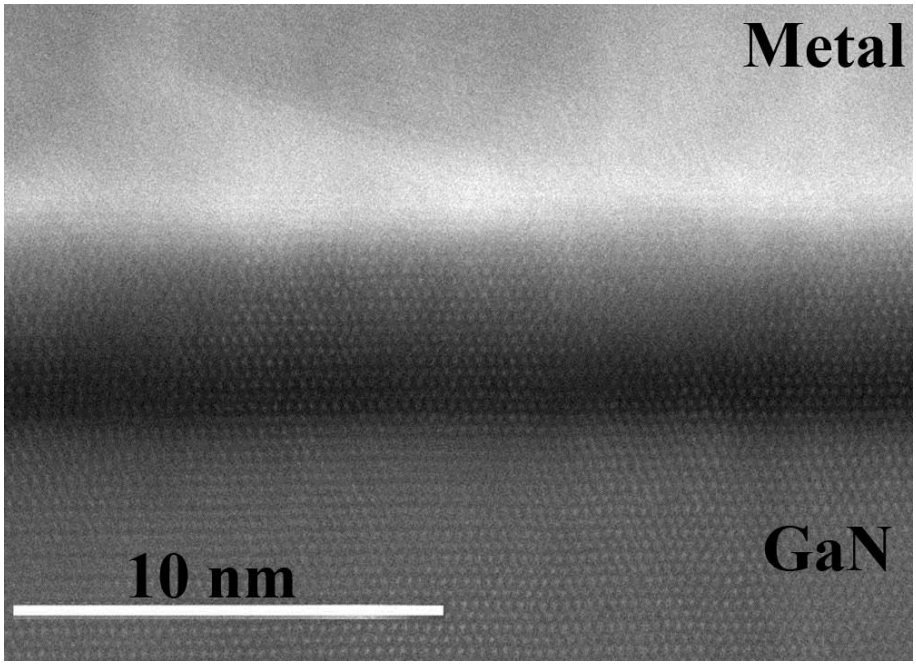

Figure 7.3: Higher magnification ADF observation of the conventional ohmic contact showing that the metal alloy is formed by small crystallites.

b- Schottky contact: Large gate lengths

The first devices that have been processed had large L_g= 3µm. At this stage, our aim was to investigate the quality and homogeneity of such gates deposited with an optical lithography process. Indeed, this is the most critical part of the device, as it monitors the operation of the whole HEMT. In order to carry out the TEM analysis,

FIB sections were prepared along the gate length. Along this length, the important features of the device are directly visible. Figure 7.4 shows the device in a <10-10> projection. We point out a small asymmetry in the gate contact. Metallic diffusion can be also observed under the source (right side) and drain (left side) contacts.

Figure 7.4: Geometry of a HEMT structure with its contacts. From left to right are the drain, gate and source. The source to gate length is shortest. The continuous large dark contrast indicates the SiN cap layer.

When a series of FIB sections are made perpendicular to the gate length, we often encounter partial non-adhesion of the metal as seen in figure 7.5. Along this direction, FIB exploration was systematically carried out along distances which could go above 10µm - 20 µm, in order to follow the evolution of this Schottky contact. We only extracted a lamella for TEM when a feature of interest was noticed.

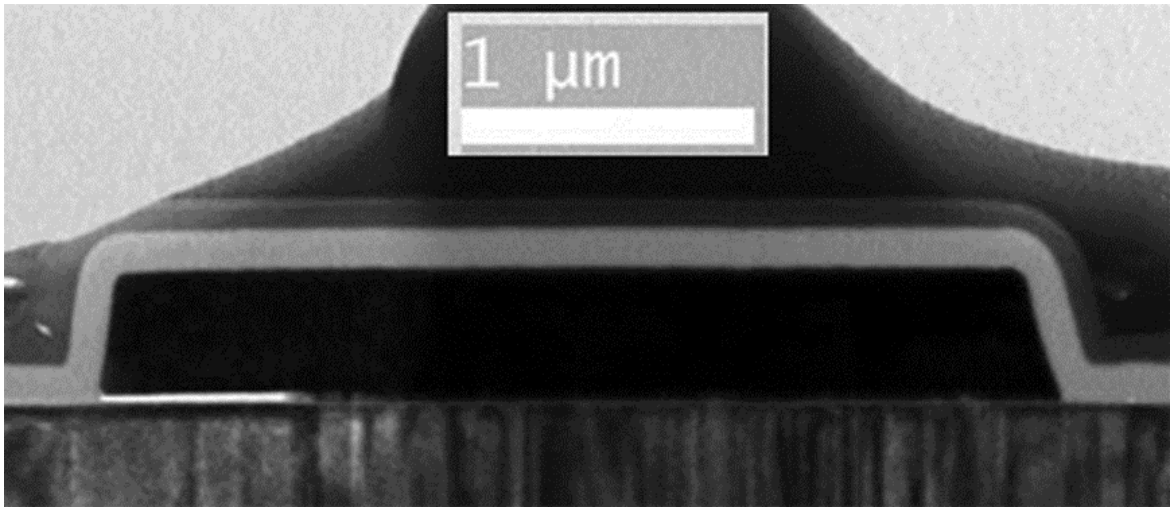

Figure 7.5: Bright field micrograph of the gate contact. The non-adhesion of the gate can be localized at its edge.

One point that should be underlined is that this non-adhesion was happening in a quite random way.

Second generation

a- Ohmic contacts

In order to improve the performance of the HEMTs, recent developments have consisted in carrying out localized epitaxy of the ohmic contact[158]. In this case, optimal values of the contact resistance on these types of barriers have been brought close to 0.16 Ω.mm. One of the goals of the LHOM project is to attain comparable performances with simpler process than localized MBE through setting up a prior surface treatment process. The process consists of the usual treatment to remove the in situ SiN by an Ar plasma, the improvement has been mostly the coupling with a chemical reagent, the used metal stack for the ohmic contact is again the same Ti/Al/Ni/Au. The annealing RTA is always rapid thermal annealing at 875°C. Interestingly, the resulting microstructure changes completely. As can be seen in figure 7.6, it may be pointed out that diffusion areas extend much in the direction parallel to the surface.

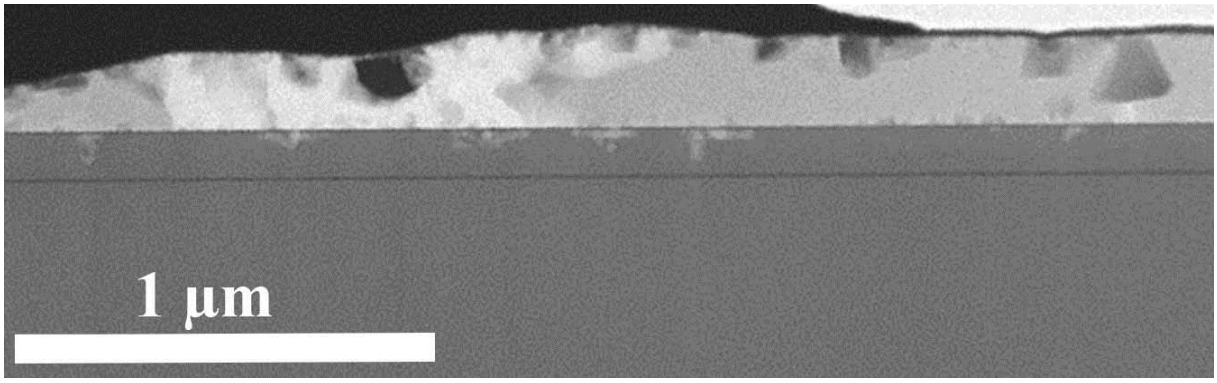

Figure 7.6: Large-scale ADF image of optimized ohmic contact showing a more uniform Ti/Al/Ni/Au alloy.

When the interfacial region is examined at high resolution, the difference is even more striking. As clearly exhibited in figure 7.7, although we also have small metallic crystallite in contact with the barrier, this time, they are coherently oriented and have epitaxial relationship.

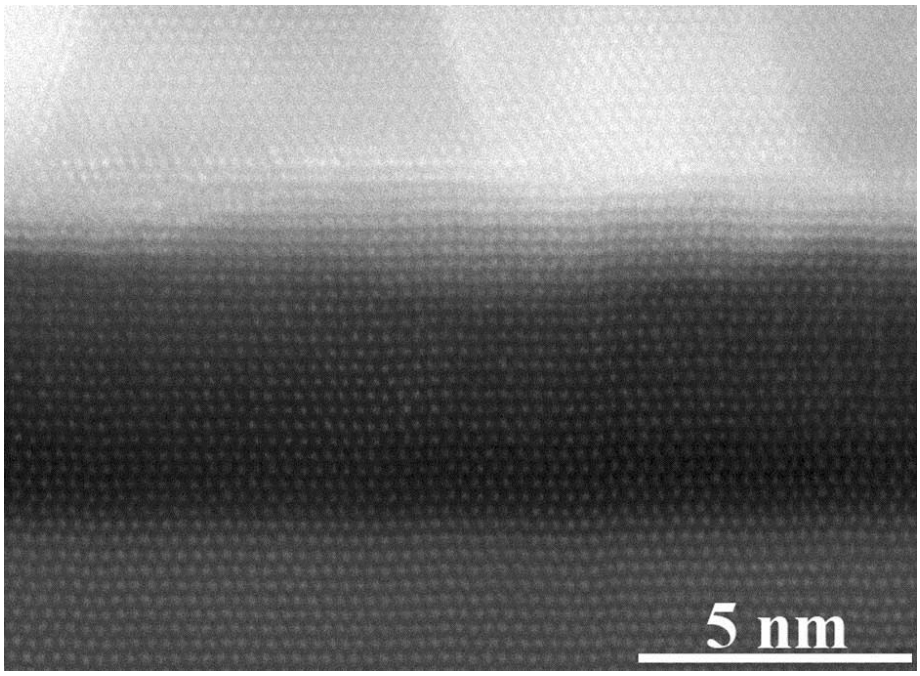

Figure 7.7: High magnification image of the optimized ohmic contact. After the RTA, an epitaxial relationship is established between the barrier and the ohmic contact.

b- Gate contact

The elaboration process of the gate has been then optimized. After the ohmic contact elaboration and by e-beam means, the gate site is precisely defined. Then using the optimized deposition process the Schottky contact is deposited. As can be seen figure 7.8, in this case, L_g is around 200 nm. Doing so, we did not detect any non-adhesion regions.

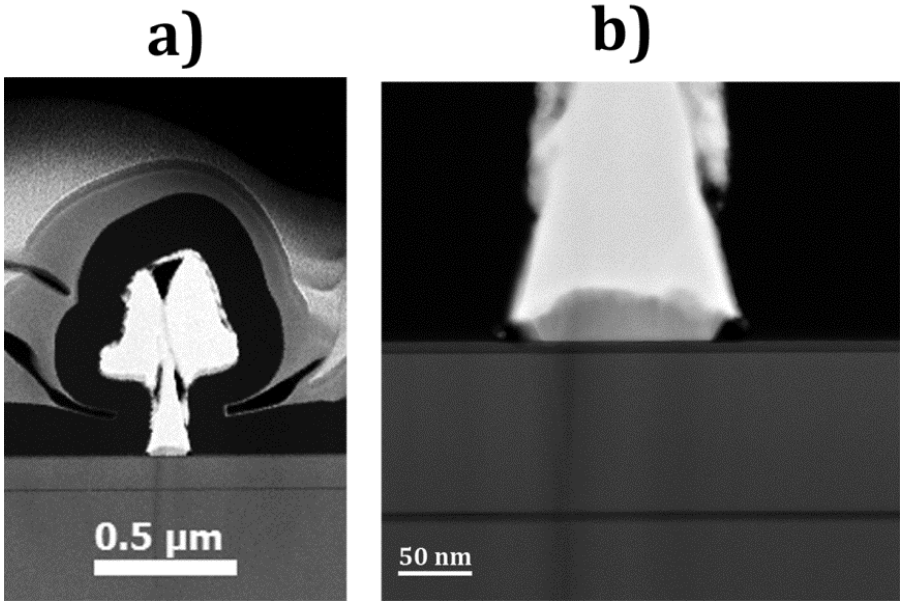

Figure 7.8: ADF showing optimized gate geometry. L_g= 200 nm a) large scale that highlights the "T"-shape b) the uniformity of the contact is shown at higher scale.

Characteristics of the two generations of devices

In order to operate at higher frequencies with higher efficiencies, the ohmic contacts resistance must be as low as possible. In this instance, by optimizing the process of the ohmic contacts deposition, their resistance dropped from 0.4 Ω.mm to 0.16 Ω.mm. Such values (0.16 Ω.mm) have been obtained by Guo et al.[158] while using a heavier process; which consists in a prior MBE regrowth of GaN below the ohmic contacts. For the first generation, the power-gain cut-off frequency was 190 GHz. Whereas for the second generation, power-gain cut-off frequency was *260* Ghz. Furthermore, by optimizing the Schottky contact, the leakage current between the source-drain to the gate is reduced from few µA to less than 100 nA.

7.2.2. AlN optimization

As shown by Gamarra et al.[159], the AlN spacer is affected by the V/III ratio, subsequently, the electrical properties of the device are directly affected. From a V/III of 1280 to 12800 the sheet resistance of the 2DEG drops from 1069 Ω/□ to 327 Ω/□.

Similarly to AlGaN/GaN, Song et al. [115] showed that optimizing the thickness of AlN helps reduce further the sheet resistance down to 307 Ω/□ and increases the 2DEG mobility up to 1600 $cm^2V^{-1}s^{-1}$.

For AlInN (7 nm thick) based devices, Xun et al.[116] observed that 1.3 nm of AlN strongly decreases the sheet resistance from 3020 Ω/□ (without AlN) to a minimum of 359 Ω/□. On the other hand, the electron mobility reached a maximum at 1051 $cm^2V^{-1}s^{-1}$ and a density of 1.84 $*10^{13}$ cm^{-2}.

On the same basis, the thickness of the AlN in the presented devices was optimized at 1.2 nm. The obtained sheet resistance did not exceed 191 Ω/□ and the electron mobility reaches 1800 $cm^2V^{-1}s^{-1}$ with a 2DEG density of 1.9 $*10^{13}$ at room temperature[152]. HAADF of figure 7.9 shows that the thickness obtained of AlN is close to the nominal one and that the interfaces are abrupt. Moreover, no IDs were observed and the TDs densities were very low. Thus, a high quality uniform AlN is systematically obtained.

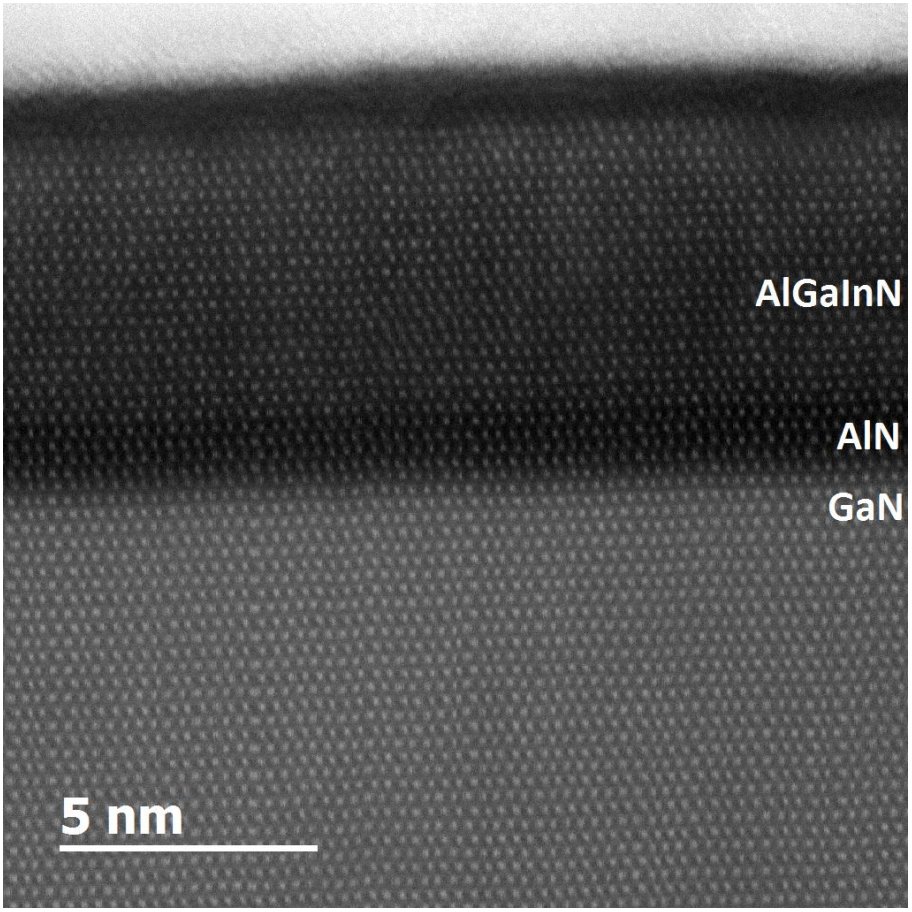

Figure 7.9: HAADF image of the AlN interlayer recorded along <11-20>.

7.2.3. SiN passivation layer

Following the objective of the LHOM research to develop an efficient passivation procedure, the first step was to try to avoid the surface oxidation of the barrier before the device processing. It is obvious that for an electronic component, oxidation is not desirable; because the involved metals would lead to the formation of various oxides which will exhibit non-homogeneous films. In addition, such as dangling bonds or surface defects may introduce additional electrons/holes states in the band gap of the semiconductor. This can be interpreted as a virtual gate located at the bottom of the metallic gate contact that controls the current flow[160]. Therefore, a drop in the current is observed. This phenomenon is known as gate lag. The deposition of a passivation layer can reduce the effect of this kind of degradations. In addition, as nitrogen is an intrinsic element in nitrides, it is expected that SiN constitutes a good passivating material for the active surfaces[80]. Depending on the deposition conditions, SiN will have different compositions up to the-high-temperature most stable crystalline Si_3N_4.

In the project, the passivation was carried out in two steps, 1) the optimization of the in-situ silicon nitride for the effective protection of the device surface from oxidation that follows the MOVPE of the barrier. Also, it avoids any modifications of the surface properties from air exposure which constitutes the main advantage to an ex-situ process. It is also a useful protection from any contact with liquids during device processing. 2) The second silicon nitride was grown ex-situ by plasma-assisted deposition (PAD).

As was noticed, the in-situ deposition of the SiN is a very slow process and a close optimization of its thickness had to be carried out for efficiency. At the beginning, it was expected that some 1-3 nm in-situ SiN would be enough to ensure the protection against the oxidation of the component, and this is the case. The optimized growth rate is 15nm/h[80]. It is found to prevent any indium desorption from the barrier and roughening of the surface. However, the second passivation step involves a thick silicon nitride layer by plasma-assisted deposition (PAD). In fact, it was noticed that this PAD brings in high energies and charges which need to be kept far from the barrier surface, to this end, it was found necessary to deposit in-situ SiN layers of at least 3.7 nm in the growth chamber.

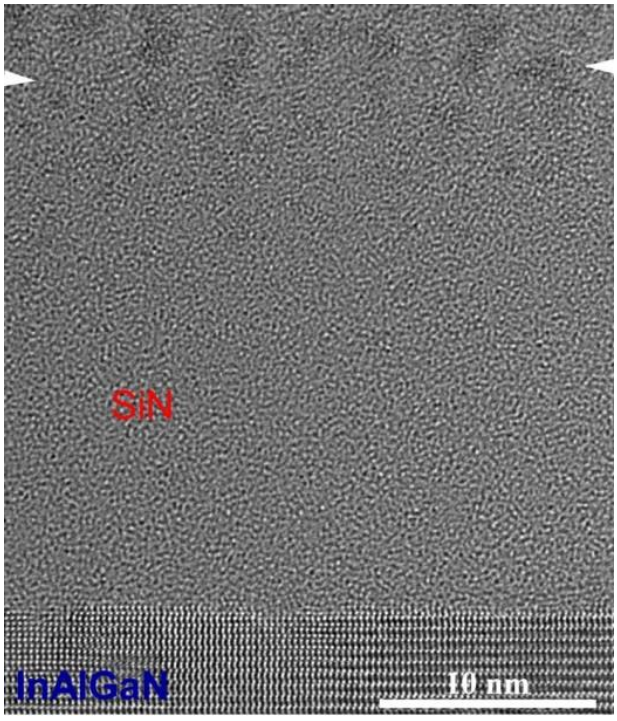

Figure 7.10: The SiN deposited in-situ at 875 °C exhibits an amorphous structure and an abrupt interface with the AlGaInN barrier.

Finally, the optimum thickness of the SiN for optimal passivation is 10 nm. As the deposition is carried out at the same temperature (875 °C) as that of the barrier, we investigated its structure.

The in-situ SiN is amorphous which is a clear indication that 875°C is still too low for SiN to crystallize, even to form visible nano-crystallites. In figure 7.10, no lattice fringes are visible, meaning that if any ordering is taking place in SiN, it is at very short distances (< 1 nm). Interestingly, all our analyses show that although we are unintentionally incorporating Ga to form a quaternary allow, as soon as the SiN deposition is initiated, no more gallium is incorporated.

The difference between the PAD and in-situ SiN film is clearly exhibited in figure 7.11. In this HAADF, the in-situ SiN presents a completely homogeneous contrast whereas inside the PAD SiN numerous dark areas can be seen especially at the interface with the in-situ SiN. From these areas, we did not detect any foreign material, which means that this film is porous. Therefore, in order to avoid the possible charge effects of this protection PAD SiN, it has to be kept at about 3.7 nm from the barrier surface using the high quality in-situ amorphous SiN.

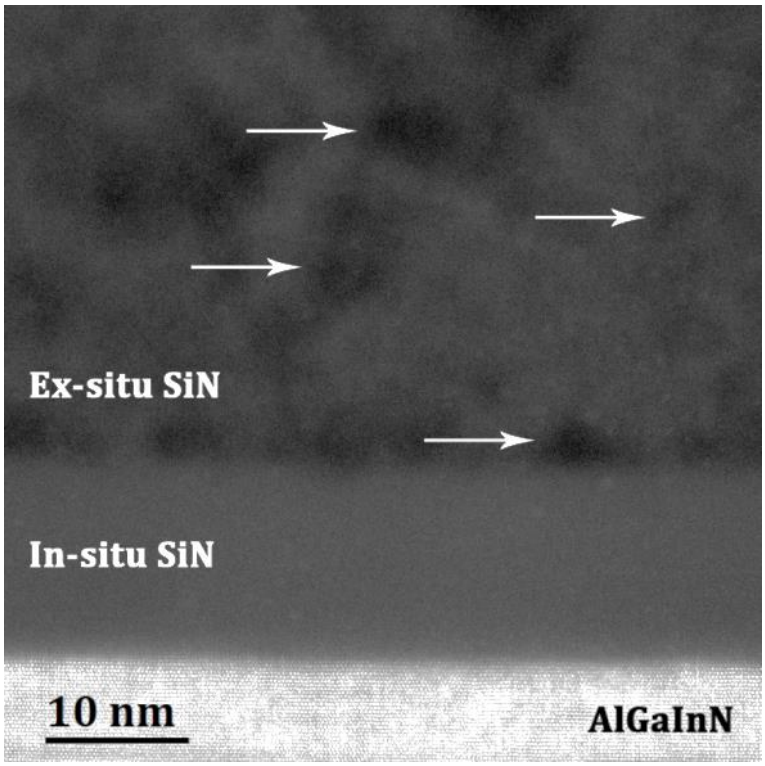

Figure 7.11: HAADF image showing the change in the quality between the in-situ and the PAD SiN

7.3. Summary

During the project different parts of the HEMT device have been optimized; both contacts (ohmic and Schottky), the passivation layer and also the AlN layer have been characterized. For these devices, the electron mobility is around 1800 $cm^2V^{-1}s^{-1}$ with a 2DEG density of 1.9 $*10^{13}$ cm^{-2}. The break-down voltage is higher than 200 V and the power-gain cut off frequency is as high as 260 Ghz.

Conclusions

The aims of the LHOM project were to develop high-quality HEMTs based on the ternary/quaternary alloys capable of sustaining breakdown voltages as high as 80 V and delivering high-frequency performances above 190 GHz.

This thesis was then focused on the study of the crystalline quality as well as the surface analysis of AlInN and AlGaInN grown by MOVPE. Furthermore, we have contributed to the devices characterization all along the project as different constituents were being optimized.

In our work, samples were provided by the III-V Laboratories. We have used TEM for a characterization from the nanometer scale to the atomic scale while using the different possibilities of this technique: diffraction contrast mode, EDS, CBD…. AFM was used for surface morphologies analysis and with the provided data, interesting features were determined and were further 1) observed in SEM which is equipped with a FIB thus 2) TEM samples were prepared around these features.

In the following, our major contributions and perspectives of our results are summarized.

The barriers in this thesis were grown in two distinct MOVPE chambers; a horizontal and a vertical CCS reactor. We have observed that gallium is systematically incorporated in the latter CCS reactor leading to quaternary alloys AlGaInN. This incorporation is predominantly due to the reactor geometry; its sources are the shower head and the interior walls during the same run. Through our analysis, we have excluded the susceptor because the incorporation was uniform along a wafer, and diffusion of gallium atoms from the GaN buffer because samples grown in the horizontal chamber are pure ternary AlInN directly grown on GaN. Through EDS measurements, we have found that the aluminum concentration is decreased by some 10% from the expected value at lattice match of the AlInN ternary alloy to GaN, whereas, the ratio Ga/In appears to change in a correlated way. Therefore, we propose that in the gas phase TMIn can react easier with residual gallium and form gallium-by-products which then contribute to the growth. Still, the presence of gallium can be avoided by adopting a cleaner growth procedure dropping its content

to 1%, or by tuning the total chamber pressure (80 Torr) which can help to decrease the Ga concentration to around 6%.

The second step of this thesis was to investigate defects in AlInN and AlGaInN barriers. The samples that we have studied were grown on silicon and sapphire which have several kinds of mismatches with GaN. Firstly, we have checked the quality of GaN by TEM. It was observed that, while using a two-step growth method, low TDs density around 10^{-8} cm^{-2} can be obtained in GaN. Still, subgrain boundaries can be generated between the LT-GaN and HT-GaN to accommodate strain. The few TDs reaching the surface generated pinholes. The correlation between the shapes of pinholes on hillocks and the associated dislocation type has been established. Pure edge-type threading dislocations open up as pinholes on the top of hillocks. Mixed-type threading dislocations form pinholes on their top but with larger hillocks. Moreover, smaller pinholes (twice as small) not connected to threading dislocations were systematically observed; they form during the growth of the AlGaInN alloy.

Besides pits, trenches related to inversion domains were also observed. The formation of these trenches was explained by the growth dynamics on N-polar GaN domain for which the growth rate is decreased and the built-up strain in the local region between N- and Ga-polar domains due to 1) composition fluctuations, mainly through 2) In and Al interplay and 3) altering the AlN interlayer. This leads to the formation of multiple ring trenches instead of separated pinholes as the barrier thickness has been increased.

As a consequence, defects were termed as extrinsic if their origins were defects from the buffer layer or intrinsic if they appear during the growth of the epitaxial layers.

In this analysis, we have pointed out that inherent defects appear for nearly lattice-matched layers probably due to an intrinsic 3D growth mode from the early stages of the epitaxy. In fact, for a nominal indium composition in a ternary of 19%, we have found from EDS that the fluctuation can be as high as 11% - 35%. This is most certainly due to phase separation as an intrinsic mechanism to relax the strain. It is shown theoretically that AlInN has the strongest mismatches in comparison to AlGaN and InGaN in terms of bond lengths and strengths. Also, the critical temperature for

the phase decomposition is the highest for this alloy. Thus the final layers quality is rapidly decreased whenever the thickness is increased.

In this instance, a direct observation of the intrinsic degradation should be considered as a priority. Nowadays, in-situ TEM measurements are being extensively developed. As a proposition, the development of a TEM/sample holder capable of generating MOVPE atmosphere would be an interesting technological challenge and a starting point to monitor at the atomic scale the growth of AlInN and AlGaInN.

Our contribution in the LHOM project was also the characterization of optimized components of the HEMT devices. Using TEM methods, we have analyzed both contacts (ohmic and Schottky), the passivation layer and also the AlN interlayer. The achievements of the LHOM project were electron mobility around 1800 $cm^2V^{-1}s^{-1}$ with a 2DEG density of 1.9 $*10^{13}$ cm^{-2}. Furthermore, the break-down voltage is higher than 200 V and the cut off frequency is as high as 260 GHz. This constitutes first steps toward the replacements of conventional AlGaN/GaN barriers with higher performances through the better understanding of AlGaInN barrier growth.

References

[1] M. Meneghini, G. Meneghesso, E. Zanoni, eds., Power GaN Devices, Springer International Publishing, Cham, 2017. doi:10.1007/978-3-319-43199-4.

[2] D. Zhu, D.J. Wallis, C.J. Humphreys, Prospects of III-nitride optoelectronics grown on Si, Rep. Prog. Phys. 76 (2013) 106501. doi:10.1088/0034-4885/76/10/106501.

[3] F. Fichter, Über Aluminiumnitrid, Z. Für Anorg. Chem. 54 (1907) 322–327.

[4] F. Fischer, F. Schröter, Über neue Metall-Stickstoff-Verbindungen und ihre Stabilität an der Hand des periodischen Systems, Eur. J. Inorg. Chem. 43 (1910) 1465–1479.

[5] W.C. Johnson, J.B. Parsons, Nitrogen compounds of gallium. I, II, J. Phys. Chem. 36 (1932) 2588–2594.

[6] H.P. Maruska, J.J. Tietjen, THE PREPARATION AND PROPERTIES OF VAPOR-DEPOSITED SINGLE-CRYSTAL-LINE GaN, Appl. Phys. Lett. 15 (1969) 327–329. doi:10.1063/1.1652845.

[7] H.M. Manasevit, F.M. Erdmann, W.I. Simson, The Use of Metalorganics in the Preparation of Semiconductor Materials, J Electrochem Soc. 118 (1971) 1864.

[8] S. Yoshida, S. Misawa, A. Itoh, Epitaxial growth of aluminum nitride films on sapphire by reactive evaporation, Appl. Phys. Lett. 26 (1975) 461–462. doi:10.1063/1.88210.

[9] S. Nakamura, T. Mukai, M. Senoh, N. Iwasa, Nakamura1992.pdf, Jpn J Appl Phys. 31 (1992) 139–142.

[10] H. Amano, M. Kito, K. Hiramatsu, I. Akasaki, P-type conduction in Mg-doped GaN treated with low-energy electron beam irradiation (LEEBI), Jpn. J. Appl. Phys. 28 (1989) 2112–2114.

[11] A. Yasan, R. McClintock, K. Mayes, S.R. Darvish, H. Zhang, P. Kung, M. Razeghi, S.K. Lee, J.Y. Han, Comparison of ultraviolet light-emitting diodes with peak emission at 340 nm grown on GaN substrate and sapphire, Appl. Phys. Lett. 81 (2002) 2151–2153. doi:10.1063/1.1508414.

[12] A. Yasan, R. McClintock, K. Mayes, D. Shiell, L. Gautero, S.R. Darvish, P. Kung, M. Razeghi, 4.5 mW operation of AlGaN-based 267 nm deep-ultraviolet light-emitting diodes, Appl. Phys. Lett. 83 (2003) 4701–4703. doi:10.1063/1.1633019.

[13] S. Nakamura, M. Senoh, S. Nagahama, N. Iwasa, T. Yamada, T. Matsushita, Y. Sugimoto, H. Kiyoku, Room-temperature continuous-wave operation of InGaN multi-quantum-well-structure laser diodes with a long lifetime, Appl. Phys. Lett. 70 (1997) 868–870. doi:10.1063/1.118300.

[14] S. Nakamura, M. Senoh, T. Mukai, High-power InGaN/GaN double-heterostructure violet light emitting diodes, Appl. Phys. Lett. 62 (1993) 2390–2392. doi:10.1063/1.109374.

[15] M.A. Khan, J.M. Van Hove, J.N. Kuznia, D.T. Olson, High electron mobility GaN/Al $_{x}$ Ga $_{1-x}$ N heterostructures grown by low-pressure metalorganic chemical vapor deposition, Appl. Phys. Lett. 58 (1991) 2408–2410. doi:10.1063/1.104886.

[16] M. Asif Khan, A. Bhattarai, J.N. Kuznia, D.T. Olson, High electron mobility transistor based on a GaN-Al $_{x}$ Ga $_{1-x}$ N heterojunction, Appl. Phys. Lett. 63 (1993) 1214–1215. doi:10.1063/1.109775.

[17] J. Kuzmík, Power electronics on InAlN/(In) GaN: Prospect for a record performance, IEEE Electron Device Lett. 22 (2001) 510–512.
[18] J.-F. Carlin, M. Ilegems, High-quality AlInN for high index contrast Bragg mirrors lattice matched to GaN, Appl. Phys. Lett. 83 (2003) 668–670. doi:10.1063/1.1596733.
[19] C. Hums, J. Bläsing, A. Dadgar, A. Diez, T. Hempel, J. Christen, A. Krost, K. Lorenz, E. Alves, Metal-organic vapor phase epitaxy and properties of AlInN in the whole compositional range, Appl. Phys. Lett. 90 (2007) 022105. doi:10.1063/1.2424649.
[20] Web of Science published by THOMSON REUTERS, WEB Sci. (2017). www.isiknowledge.com.
[21] R. Butté, J.-F. Carlin, E. Feltin, M. Gonschorek, S. Nicolay, G. Christmann, D. Simeonov, A. Castiglia, J. Dorsaz, H.J. Buehlmann, S. Christopoulos, G. Baldassarri Höger von Hög, A.J.D. Grundy, M. Mosca, C. Pinquier, M.A. Py, F. Demangeot, J. Frandon, P.G. Lagoudakis, J.J. Baumberg, N. Grandjean, Current status of AlInN layers lattice-matched to GaN for photonics and electronics, J. Phys. Appl. Phys. 40 (2007) 6328–6344. doi:10.1088/0022-3727/40/20/S16.
[22] F.G. McIntosh, K.S. Boutros, J.C. Roberts, S.M. Bedair, E.L. Piner, N.A. El-Masry, Growth and characterization of AlInGaN quaternary alloys, Appl. Phys. Lett. 68 (1996) 40–42. doi:10.1063/1.116749.
[23] D. Jena, J. Simon, A.K. Wang, Y. Cao, K. Goodman, J. Verma, S. Ganguly, G. Li, K. Karda, V. Protasenko, C. Lian, T. Kosel, P. Fay, H. Xing, Polarization-engineering in group III-nitride heterostructures: New opportunities for device design, Phys. Status Solidi A. 208 (2011) 1511–1516. doi:10.1002/pssa.201001189.
[24] N. Ketteniss, L.R. Khoshroo, M. Eickelkamp, M. Heuken, H. Kalisch, R.H. Jansen, A. Vescan, Study on quaternary AlInGaN/GaN HFETs grown on sapphire substrates, Semicond. Sci. Technol. 25 (2010) 075013. doi:10.1088/0268-1242/25/7/075013.
[25] T. Matsuoka, N. Yoshimoto, T. Sasaki, A. Katsui, Wide-Gap Semiconductor InGaN and InGaAIN Grown by MOVPE, J. Electron. Mater. 21 (1992) 157–163.
[26] G. Naresh-Kumar, A. Vilalta-Clemente, S. Pandey, D. Skuridina, H. Behmenburg, P. Gamarra, G. Patriarche, I. Vickridge, M.A. di Forte-Poisson, P. Vogt, M. Kneissl, M. Morales, P. Ruterana, A. Cavallini, D. Cavalcoli, C. Giesen, M. Heuken, C. Trager-Cowan, Multicharacterization approach for studying InAl(Ga)N/Al(Ga)N/GaN heterostructures for high electron mobility transistors, AIP Adv. 4 (2014) 127101. doi:10.1063/1.4903227.
[27] Ronghua Wang, Guowang Li, J. Verma, B. Sensale-Rodriguez, Tian Fang, Jia Guo, Zongyang Hu, O. Laboutin, Yu Cao, W. Johnson, G. Snider, P. Fay, D. Jena, Huili Xing, 220-GHz Quaternary Barrier InAlGaN/AlN/GaN HEMTs, IEEE Electron Device Lett. 32 (2011) 1215–1217. doi:10.1109/LED.2011.2158288.
[28] K. Makiyama, S. Ozaki, T. Ohki, N. Okamoto, Y. Minoura, Y. Niida, Y. Kamada, K. Joshin, K. Watanabe, Y. Miyamoto, Collapse-free high power InAlGaN/GaN-HEMT with 3 W/mm at 96 GHz, in: Electron Devices Meet. IEDM 2015 IEEE Int., IEEE, 2015: pp. 9–1. http://ieeexplore.ieee.org/abstract/document/7409659/ (accessed June 7, 2017).
[29] Z.T. Chen, K. Fujita, J. Ichikawa, T. Egawa, Threading dislocation-governed degradation in crystal quality of heteroepitaxial materials: The case of InAlN nearly lattice-matched to GaN, J. Appl. Phys. 111 (2012) 053535. doi:10.1063/1.3693039.

[30] Z.L. Miao, T.J. Yu, F.J. Xu, J. Song, C.C. Huang, X.Q. Wang, Z.J. Yang, G.Y. Zhang, X.P. Zhang, D.P. Yu, B. Shen, The origin and evolution of V-defects in InxAl1−xN epilayers grown by metalorganic chemical vapor deposition, Appl. Phys. Lett. 95 (2009) 231909. doi:10.1063/1.3272017.
[31] G. Perillat-Merceroz, G. Cosendey, J.-F. Carlin, R. Butté, N. Grandjean, Intrinsic degradation mechanism of nearly lattice-matched InAlN layers grown on GaN substrates, J. Appl. Phys. 113 (2013) 063506. doi:10.1063/1.4790424.
[32] H. Morkoç, S. Strite, G.B. Gao, M.E. Lin, B. Sverdlov, M. Burns, Large band gap SiC, III-V nitride, and II-VI ZnSe based semiconductor device technologies, J. Appl. Phys. 76 (1994) 1363–1398. doi:10.1063/1.358463.
[33] J. Serrano, A. Rubio, E. Hernández, A. Muñoz, A. Mujica, Theoretical study of the relative stability of structural phases in group-III nitrides at high pressures, Phys. Rev. B. 62 (2000) 16612.
[34] A.F. Wright, Elastic properties of zinc-blende and wurtzite AlN, GaN, and InN, J. Appl. Phys. 82 (1997) 2833–2839. doi:10.1063/1.366114.
[35] S. Keller, H. Li, M. Laurent, Y. Hu, N. Pfaff, J. Lu, D.F. Brown, N.A. Fichtenbaum, J.S. Speck, S.P. DenBaars, U.K. Mishra, Recent progress in metal-organic chemical vapor deposition of N-polar group-III nitrides, Semicond. Sci. Technol. 29 (2014) 113001. doi:10.1088/0268-1242/29/11/113001.
[36] F. Bernardini, V. Fiorentini, D. Vanderbilt, Spontaneous polarization and piezoelectric constants of III-V nitrides, Phys. Rev. B. 56 (1997) R10024.
[37] F. Bechstedt, U. Grossner, J. Furthmüller, Dynamics and polarization of group-III nitride lattices: A first-principles study, Phys. Rev. B. 62 (2000) 8003.
[38] C.E.C. Wood, D. Jena, eds., Polarization effects in semiconductors: from ab initio theory to device application, Springer, New York, NY, 2008.
[39] F. Bernardini, V. Fiorentini, Nonlinear macroscopic polarization in III-V nitride alloys, Phys. Rev. B. 64 (2001). doi:10.1103/PhysRevB.64.085207.
[40] O.V. Voznyy, V.G. Deibuk, Chemical bonding and optical bowing in III-nitrides solid solutions, Semicond. Phys. QUANTUM Electron. Optoelectron. 6 (2003) 115–120.
[41] Z. Dridi, B. Bouhafs, P. Ruterana, First-principles investigation of lattice constants and bowing parameters in wurtzite AlxGa1- xN, InxGa1- xN and InxAl1- xN alloys, Semicond. Sci. Technol. 18 (2003) 850.
[42] W. Terashima, S.-B. Che, Y. Ishitani, A. Yoshikawa, Growth and characterization of AlInN ternary alloys in whole composition range and fabrication of InN/AlInN multiple quantum wells by RF molecular beam epitaxy, Jpn. J. Appl. Phys. 45 (2006) L539.
[43] I. Gorczyca, S.P. ?epkowski, T. Suski, N.E. Christensen, A. Svane, Influence of indium clustering on the band structure of semiconducting ternary and quaternary nitride alloys, Phys. Rev. B. 80 (2009). doi:10.1103/PhysRevB.80.075202.
[44] I. Gorczyca, T. Suski, N.E. Christensen, A. Svane, Limitations to band gap tuning in nitride semiconductor alloys, Appl. Phys. Lett. 96 (2010) 101907. doi:10.1063/1.3357419.
[45] I. Gorczyca, T. Suski, N.E. Christensen, A. Svane, Band gap bowing in quaternary nitride semiconducting alloys, Appl. Phys. Lett. 98 (2011) 241905. doi:10.1063/1.3597795.
[46] V. Darakchieva, M.-Y. Xie, F. Tasnádi, I.A. Abrikosov, L. Hultman, B. Monemar, J. Kamimura, K. Kishino, Lattice parameters, deviations from Vegard's rule, and

E2 phonons in InAlN, Appl. Phys. Lett. 93 (2008) 261908. doi:10.1063/1.3056656.

[47] S. Magalhães, N. Franco, I.M. Watson, R.W. Martin, K.P. O'Donnell, H.P.D. Schenk, F. Tang, T.C. Sadler, M.J. Kappers, R.A. Oliver, T. Monteiro, T.L. Martin, P.A.J. Bagot, M.P. Moody, E. Alves, K. Lorenz, Validity of Vegard's rule for AlxIn1-xN (0.08x<0.28) thin films grown on GaN templates, J. Phys. Appl. Phys. 50 (2017) 205107. doi:10.1088/1361-6463/aa69dc.

[48] V.Y. Davydov, A.A. Klochikhin, R.P. Seisyan, V.V. Emptsev, S.V. Ivanov, F. Bechstedt, J. Furthmüller, H. Harima, A.V. Mudryi, J. Aderhold, O. Semchinova, J. Graul, Absorption and Emission of Hexagonal InN. Evidence of Narrow Fundamental Band Gap, Phys. Status Solidi B. 229 (2002) R1–R3. doi:10.1103/PhysRevB.74.115319.

[49] C.K. Gan, Y.P. Feng, D.J. Srolovitz, First-principles calculation of the thermodynamics of In x Ga 1 − x N alloys: Effect of lattice vibrations, Phys. Rev. B. 73 (2006). doi:10.1103/PhysRevB.73.235214.

[50] S. Amelinckx, The characterization of defects in crystals, J. Cryst. Growth. 24 (1974) 6–10.

[51] W. Kim, A.E. Botchkarev, H. Morkoç, Z.-Q. Fang, D.C. Look, D.J. Smith, Effect of ammonia flow rate on impurity incorporation and material properties of Si-doped GaN epitaxial films grown by reactive molecular beam epitaxy, J. Appl. Phys. 84 (1998) 6680–6685. doi:10.1063/1.369044.

[52] Z.-Q. Fang, D.C. Look, W. Kim, Z. Fan, A. Botchkarev, H. Morko?, Deep centers in n-GaN grown by reactive molecular beam epitaxy, Appl. Phys. Lett. 72 (1998) 2277–2279. doi:10.1063/1.121274.

[53] L. Li, J. Yu, Z. Hao, L. Wang, J. Wang, Y. Han, H. Li, B. Xiong, C. Sun, Y. Luo, Influence of point defects on optical properties of GaN-based materials by first principle study, Comput. Mater. Sci. 129 (2017) 49–54. doi:10.1016/j.commatsci.2016.12.017.

[54] J. Hornstra, Dislocations, stacking faults and twins in the spinel structure, J. Phys. Chem. Solids. 15 (1960) 311–323.

[55] D. Hull, D.J. Bacon, Introduction to dislocations, 5. ed, Elsevier/Butterworth-Heinemann, Amsterdam, 2011.

[56] D. Jena, A.C. Gossard, U.K. Mishra, Dislocation scattering in a two-dimensional electron gas, Appl. Phys. Lett. 76 (2000) 1707–1709.

[57] J. Kotani, A. Yamada, T. Ishiguro, S. Tomabechi, N. Nakamura, Low dislocation density InAlN/AlN/GaN heterostructures grown on GaN substrates and the effects on gate leakage characteristics, Appl. Phys. Lett. 108 (2016) 152109. doi:10.1063/1.4947004.

[58] C. Stampfl, C.G. Van de Walle, Energetics and electronic structure of stacking faults in AlN, GaN, and InN, Phys. Rev. B. 57 (1998) R15052.

[59] J. Lähnemann, U. Jahn, O. Brandt, T. Flissikowski, P. Dogan, H.T. Grahn, Luminescence associated with stacking faults in GaN, J. Phys. Appl. Phys. 47 (2014) 423001. doi:10.1088/0022-3727/47/42/423001.

[60] A. Konar, T. Fang, N. Sun, D. Jena, Charged basal stacking fault scattering in nitride semiconductors, Appl. Phys. Lett. 98 (2011) 022109. doi:10.1063/1.3543846.

[61] V. Potin, P. Ruterana, G. Nouet, R.C. Pond, H. Morkoç, Mosaic growth of GaN on (0001) sapphire: A high-resolution electron microscopy and crystallographic

study of threading dislocations from low-angle to high-angle grain boundaries, Phys. Rev. B. 61 (2000) 5587.
[62] G. Binnig, H. Rohrer, C. Gerber, E. Weibel, 7x7 reconstruction on Si (111) resolved in real space, Phys. Rev. Lett. 50 (1983) 120.
[63] DoITPoMS - TLP Library Atomic Force Microscopy - Tip Surface Interaction, Univ. Camb. - Teach. Learn. Packag. (n.d.). https://www.doitpoms.ac.uk/tlplib/afm/tip_surface_interaction.php (accessed October 31, 2017).
[64] D.B. Williams, C.B. Carter, Transmission electron microscopy: a textbook for materials science, 2. ed, Springer, New York, 2009.
[65] F.A. Ponce, Defects and interfaces in GaN epitaxy, MRS Bull. 22 (1997) 51–57.
[66] J.J. Hren, J.I. Goldstein, D.C. Joy, eds., Introduction to Analytical Electron Microscopy, Springer US, Boston, MA, 1979. doi:10.1007/978-1-4757-5581-7.
[67] JEOL, convergent beam electron diffraction, (n.d.). https://www.jeol.co.jp/en/words/emterms/search_result.html?keyword=convergent-beam%20electron%20diffraction (accessed October 31, 2017).
[68] P.J. Phillips, M. De Graef, L. Kovarik, A. Agrawal, W. Windl, M.J. Mills, Atomic-resolution defect contrast in low angle annular dark-field STEM, Ultramicroscopy. 116 (2012) 47–55. doi:10.1016/j.ultramic.2012.03.013.
[69] M. Saito, T. Aoyama, T. Hashimoto, S. Isakozawa, Transmission Electron Microscope Sample Shape Optimization for Energy Dispersive X-Ray Spectroscopy Using the Focused Ion Beam Technique, Jpn. J. Appl. Phys. 37 (1998) 355–359.
[70] T.F. Kelly, M.K. Miller, Atom probe tomography, Rev. Sci. Instrum. 78 (2007) 031101. doi:10.1063/1.2709758.
[71] J. Weimmerskirch-Aubatin, Propriétés de luminescence et caractérisation structurale de films minces d'oxydes de silicium dopés au cérium et codopés cérium-ytterbium, Université de Lorraine, 2014.
[72] P. Gamarra, Étude de composés semiconducteurs III-N à forte teneur en indium : application à l'optimisation des hétérostructures pour transistors à effet de champ piézo-électriques (HEMT), n.d.
[73] J.E. Ayers, Heteroepitaxy of semiconductors: theory, growth, and characterization, CRC Press, Boca Raton, 2007.
[74] J.R. Creighton, G.T. Wang, W.G. Breiland, M.E. Coltrin, Nature of the parasitic chemistry during AlGaInN OMVPE, J. Cryst. Growth. 261 (2004) 204–213. doi:10.1016/j.jcrysgro.2003.11.074.
[75] T.G. Mihopoulos, V. Gupta, K.F. Jensen, A reaction-transport model for AlGaN MOVPE growth, J. Cryst. Growth. 195 (1998) 733–739.
[76] S.A. Kukushkin, V.N. Bessolov, A.V. Osipov, A.V. Luk'yanov, Mechanism and kinetics of early growth stages of a GaN film, Phys. Solid State. 44 (2002) 1399–1405.
[77] A. Koukitu, Y. Kumagai, H. Seki, thermodynamic analysis of movpe growth of InAlN, Phys. Status Solidi A. 180 (2000) 115–120.
[78] A. Minj, D. Cavalcoli, G.R. Mutta Popuri, A. Vilalta-Clemente, P. Ruterana, A. Cavallini, Electrical properties of extended defects in III-nitrides, Acta Mater. 89 (2015) 290–297. doi:10.1016/j.actamat.2015.01.061.
[79] A. Minj, D. Skuridina, D. Cavalcoli, A. Cros, P. Vogt, M. Kneissl, C. Giesen, M. Heuken, Surface properties of AlInGaN/GaN heterostructure, Mater. Sci. Semicond. Process. 55 (2016) 26–31. doi:10.1016/j.mssp.2016.04.005.

[80] P. Gamarra, C. Lacam, M. Tordjman, F. Medjdoub, M.-A. di Forte-Poisson, In-situ passivation of quaternary barrier InAlGaN/GaN HEMTs, J. Cryst. Growth. 464 (2017) 143–147. doi:10.1016/j.jcrysgro.2016.11.014.

[81] J.J. Zhu, Y.M. Fan, H. Zhang, G.J. Lu, H. Wang, D.G. Zhao, D.S. Jiang, Z.S. Liu, S.M. Zhang, G.F. Chen, B.S. Zhang, H. Yang, Contribution of GaN template to the unexpected Ga atoms incorporated into AlInN epilayers grown under an indium-very-rich condition by metalorganic chemical vapor deposition (MOCVD), J. Cryst. Growth. 348 (2012) 25–30. doi:10.1016/j.jcrysgro.2012.03.035.

[82] M.D. Smith, E. Taylor, T.C. Sadler, V.Z. Zubialevich, K. Lorenz, H.N. Li, J. O'Connell, E. Alves, J.D. Holmes, R.W. Martin, P.J. Parbrook, Determination of Ga auto-incorporation in nominal InAlN epilayers grown by MOCVD, J. Mater. Chem. C. 2 (2014) 5787. doi:10.1039/c4tc00480a.

[83] S. Choi, H. Jin Kim, Z. Lochner, J. Kim, R.D. Dupuis, A.M. Fischer, R. Juday, Y. Huang, T. Li, J.Y. Huang, F.A. Ponce, J.-H. Ryou, Origins of unintentional incorporation of gallium in AlInN layers during epitaxial growth, part I: Growth of AlInN on AlN and effects of prior coating, J. Cryst. Growth. 388 (2014) 137–142. doi:10.1016/j.jcrysgro.2013.10.006.

[84] J. Kim, Z. Lochner, M.-H. Ji, S. Choi, H.J. Kim, J.S. Kim, R.D. Dupuis, A.M. Fischer, R. Juday, Y. Huang, T. Li, J.Y. Huang, F.A. Ponce, J.-H. Ryou, Origins of unintentional incorporation of gallium in InAlN layers during epitaxial growth, part II: Effects of underlying layers and growth chamber conditions, J. Cryst. Growth. 388 (2014) 143–149. doi:10.1016/j.jcrysgro.2013.09.046.

[85] B. Reuters, M. Finken, A. Wille, B. Holländer, M. Heuken, H. Kalisch, A. Vescan, Relaxation and critical strain for maximum In incorporation in AlInGaN on GaN grown by metal organic vapour phase epitaxy, J. Appl. Phys. 112 (2012) 093524. doi:10.1063/1.4764342.

[86] L. Liu, J.H. Edgar, Substrates for gallium nitride epitaxy, Mater. Sci. Eng. R Rep. 37 (2002) 61–127.

[87] E.V. Etzkorn, D.R. Clarke, Cracking of GaN films, J. Appl. Phys. 89 (2001) 1025–1034. doi:10.1063/1.1330243.

[88] H. Amano, N. Sawaki, I. Akasaki, Y. Toyoda, Metalorganic vapor phase epitaxial growth of a high quality GaN film using an AlN buffer layer, Appl. Phys. Lett. 48 (1986) 353–355. doi:10.1063/1.96549.

[89] X.L. Wang, C.M. Wang, G.X. Hu, J.X. Wang, T.S. Chen, G. Jiao, J.P. Li, Y.P. Zeng, J.M. Li, Improved DC and RF performance of AlGaN/GaN HEMTs grown by MOCVD on sapphire substrates, Solid-State Electron. 49 (2005) 1387–1390. doi:10.1016/j.sse.2005.06.022.

[90] S. Guha, N.A. Bojarczuk, Ultraviolet and violet GaN light emitting diodes on silicon, Appl. Phys. Lett. 72 (1998) 415–417. doi:10.1063/1.120775.

[91] J.H. Yang, S.M. Kang, D.V. Dinh, D.H. Yoon, Influence of AlN buffer layer thickness and deposition methods on GaN epitaxial growth, Thin Solid Films. 517 (2009) 5057–5060. doi:10.1016/j.tsf.2009.03.089.

[92] H. Lahrèche, P. Vennéguès, O. Tottereau, M. Laügt, P. Lorenzini, M. Leroux, B. Beaumont, P. Gibart, Optimisation of AlN and GaN growth by metalorganic vapour-phase epitaxy (MOVPE) on Si(1 1 1), J. Cryst. Growth. 217 (2000) 13–25.

[93] H. Lahrèche, M. Leroux, M. Laügt, M. Vaille, B. Beaumont, P. Gibart, Buffer free direct growth of GaN on 6H–SiC by metalorganic vapor phase epitaxy, J. Appl. Phys. 87 (2000) 577–583. doi:10.1063/1.371902.

[94] P. Waltereit, O. Brandt, A. Trampert, M. Ramsteiner, M. Reiche, M. Qi, K.H. Ploog, Influence of AlN nucleation layers on growth mode and strain relief of GaN grown on 6H–SiC(0001), Appl. Phys. Lett. 74 (1999) 3660–3662. doi:10.1063/1.123214.

[95] E. Dogmus, R. Kabouche, S. Lepilliet, A. Linge, M. Zegaoui, H. Ben-Ammar, M.-P. Chauvat, P. Ruterana, P. Gamarra, C. Lacam, M. Tordjman, F. Medjdoub, InAlGaN/GaN HEMTs at Cryogenic Temperatures, Electronics. 5 (2016) 31. doi:10.3390/electronics5020031.

[96] C. Kirchner, V. Schwegler, F. Eberhard, M. Kamp, K.J. Ebeling, K. Kornitzer, T. Ebner, K. Thonke, R. Sauer, P. Prystawko, M. Leszczynski, I. Grzegory, S. Porowski, Homoepitaxial growth of GaN by metalorganic vapor phase epitaxy: A benchmark for GaN technology, Appl. Phys. Lett. 75 (1999) 1098–1100. doi:10.1063/1.124609.

[97] S. Porowski, Bulk and homoepitaxial GaN-growth and characterisation, J. Cryst. Growth. 189 (1998) 153–158.

[98] D.F. Storm, D.S. Katzer, J.A. Mittereder, S.C. Binari, B.V. Shanabrook, X. Xu, D.S. McVey, R.P. Vaudo, G.R. Brandes, Homoepitaxial growth of GaN and AlGaN/GaN heterostructures by molecular beam epitaxy on freestanding HVPE gallium nitride for electronic device applications, J. Cryst. Growth. 281 (2005) 32–37. doi:10.1016/j.jcrysgro.2005.03.009.

[99] D.F. Storm, D.J. Meyer, D.S. Katzer, S.C. Binari, T. Paskova, E.A. Preble, K.R. Evans, L. Zhou, D.J. Smith, Homoepitaxial N-polar GaN layers and HEMT structures grown by rf-plasma assisted molecular beam epitaxy, J. Vac. Sci. Technol. B Nanotechnol. Microelectron. Mater. Process. Meas. Phenom. 30 (2012) 02B113. doi:10.1116/1.3676175.

[100] R. Dwiliński, R. Doradziński, J. Garczyński, L.P. Sierzputowski, A. Puchalski, Y. Kanbara, K. Yagi, H. Minakuchi, H. Hayashi, Bulk ammonothermal GaN, J. Cryst. Growth. 311 (2009) 3015–3018. doi:10.1016/j.jcrysgro.2009.01.052.

[101] R. Dwilinski, R. Doradzinski, J. Garczynski, L.P. Sierzputowski, M. Zajac, M. Rudzinski, Homoepitaxy on bulk ammonothermal GaN, J. Cryst. Growth. 311 (2009) 3058–3062. doi:10.1016/j.jcrysgro.2009.01.078.

[102] D.F. Storm, D.S. Katzer, J.A. Mittereder, S.C. Binari, B.V. Shanabrook, L. Zhou, D.J. Smith, X. Xu, D. McVey, R.P. Vaudo, G.R. Brandes, Growth and characterization of plasma-assisted molecular beam epitaxial-grown AlGaN/GaN heterostructures on free-standing hydride vapor phase epitaxy GaN substrates, J. Vac. Sci. Technol. B Microelectron. Nanometer Struct. 23 (2005) 1190. doi:10.1116/1.1885013.

[103] J.E. Northrup, L.T. Romano, J. Neugebauer, Surface energetics, pit formation, and chemical ordering in InGaN alloys, Appl. Phys. Lett. 74 (1999) 2319–2321. doi:10.1063/1.123837.

[104] T. Kehagias, G.P. Dimitrakopulos, J. Kioseoglou, H. Kirmse, C. Giesen, M. Heuken, A. Georgakilas, W. Neumann, T. Karakostas, P. Komninou, Indium migration paths in V-defects of InAlN grown by metal-organic vapor phase epitaxy, Appl. Phys. Lett. 95 (2009) 071905. doi:10.1063/1.3204454.

[105] A. Minj, D. Cavalcoli, G.R. Mutta Popuri, A. Vilalta-Clemente, P. Ruterana, A. Cavallini, Electrical properties of extended defects in III-nitrides, Acta Mater. 89 (2015) 290–297. doi:10.1016/j.actamat.2015.01.061.
[106] F.A. Ponce, D.P. Bour, W.T. Young, M. Saunders, J.W. Steeds, Determination of lattice polarity for growth of GaN bulk single crystals and epitaxial layers, Appl. Phys. Lett. 69 (1996) 337–339. doi:10.1063/1.118052.
[107] J.L. Rouviere, M. Arlery, R. Niebuhr, K.H. Bachem, O. Briot, Correlation between surface morphologies and crystallographic structures of GaN layers grown by MOCVD on sapphire, MRS Internet J. Nitride Semicond. Res. 1 (1996). doi:10.1557/S1092578300002052.
[108] P. Vermaut, P. Ruterana, G. Nouet, Polarity of epitaxial layers and (1 1 -2 0) prismatic defects in GaN and AIN grown on the (0001) $_{Si}$ surface of 6H-SiC, Philos. Mag. A. 76 (1997) 1215–1234. doi:10.1080/01418619708214224.
[109] B. Daudin, J.L. Rouvière, M. Arlery, Polarity determination of GaN films by ion channeling and convergent beam electron diffraction, Appl. Phys. Lett. 69 (1996) 2480–2482. doi:10.1063/1.117504.
[110] L.T. Romano, T.H. Myers, The influence of inversion domains on surface morphology in GaN grown by molecular beam epitaxy, Appl. Phys. Lett. 71 (1997) 3486–3488. doi:10.1063/1.120367.
[111] J. Jasinski, Z. Liliental-Weber, Q.S. Paduano, D.W. Weyburne, Inversion domains in AlN grown on (0001) sapphire, Appl. Phys. Lett. 83 (2003) 2811–2813. doi:10.1063/1.1616191.
[112] J. Jasinski, Z. Liliental-Weber, H. Lu, W.J. Schaff, V-shaped inversion domains in InN grown on c-plane sapphire, Appl. Phys. Lett. 85 (2004) 233–235. doi:10.1063/1.1772863.
[113] B. Pécz, Z. Makkai, M.A. di Forte-Poisson, F. Huet, R.E. Dunin-Borkowski, V-shaped defects connected to inversion domains in AlGaN layers, Appl. Phys. Lett. 78 (2001) 1529–1531. doi:10.1063/1.1355996.
[114] S. Mahanty, M. Hao, T. Sugahara, R.Q. Fareed, Y. Morishima, Y. Naoi, T. Wang, S. Sakai, V-shaped defects in InGaN/GaN multiquantum wells, Mater. Lett. 41 (1999) 67–71.
[115] J. Song, F.J. Xu, Z.L. Miao, Y. Wang, X.Q. Wang, B. Shen, Influence of ultrathin AlN interlayer on the microstructure and the electrical transport properties of AlxGa1−xN/GaN heterostructures, J. Appl. Phys. 106 (2009) 083711. doi:10.1063/1.3246866.
[116] D. Xun, L. Zhong-Hui, L. Zhe-Yang, Z. Jian-Jun, L. Liang, L. Yun, Z. Lan, X. Xiao-Jun, X. Xuan, H. Chun-Lin, Effects of AlN and AlGaN Interlayer on Properties of InAlN/GaN Heterostructures, Chin. Phys. Lett. 27 (2010) 037102. doi:10.1088/0256-307X/27/3/037102.
[117] S.L. Rhode, W.Y. Fu, M.A. Moram, F.C.-P. Massabuau, M.J. Kappers, C. McAleese, F. Oehler, C.J. Humphreys, R.O. Dusane, S. –L. Sahonta, Structure and strain relaxation effects of defects in In $_{x}$ Ga $_{1-x}$ N epilayers, J. Appl. Phys. 116 (2014) 103513. doi:10.1063/1.4894688.
[118] F.C.-P. Massabuau, S.-L. Sahonta, L. Trinh-Xuan, S. Rhode, T.J. Puchtler, M.J. Kappers, C.J. Humphreys, R.A. Oliver, Morphological, structural, and emission characterization of trench defects in InGaN/GaN quantum well structures, Appl. Phys. Lett. 101 (2012) 212107. doi:10.1063/1.4768291.
[119] S.-L. Sahonta, M.J. Kappers, D. Zhu, T.J. Puchtler, T. Zhu, S.E. Bennett, C.J. Humphreys, R.A. Oliver, Properties of trench defects in InGaN/GaN quantum

well structures, Phys. Status Solidi A. 210 (2013) 195–198. doi:10.1002/pssa.201200408.
[120] R. Datta, M.J. Kappers, J.S. Barnard, C.J. Humphreys, Revealing all types of threading dislocations in GaN with improved contrast in a single plan view image, Appl. Phys. Lett. 85 (2004) 3411–3413.
[121] G. Perillat-Merceroz, G. Cosendey, J.-F. Carlin, R. Butté, N. Grandjean, Intrinsic degradation mechanism of nearly lattice-matched InAlN layers grown on GaN substrates, J. Appl. Phys. 113 (2013) 063506. doi:10.1063/1.4790424.
[122] V. Potin, G. Nouet, P. Ruterana, The {10 1 0} inversion domains in GaN/sapphire layers: An electron microscopy analysis of the atomic structure of the boundaries, Philos. Mag. A. 79 (1999) 2899–2919. doi:10.1080/01418619908212032.
[123] C. Hums, J. Bläsing, A. Dadgar, A. Diez, T. Hempel, J. Christen, A. Krost, K. Lorenz, E. Alves, Metal-organic vapor phase epitaxy and properties of AlInN in the whole compositional range, Appl. Phys. Lett. 90 (2007) 022105. doi:10.1063/1.2424649.
[124] C. Hums, J. Bläsing, A. Dadgar, A. Diez, T. Hempel, J. Christen, A. Krost, K. Lorenz, E. Alves, Erratum: “Metal-organic vapor phase epitaxy and properties of AlInN in the whole compositional range” [Appl. Phys. Lett. 90, 022105 (2007)], Appl. Phys. Lett. 91 (2007) 139901. doi:10.1063/1.2785981.
[125] R. Butté, J.-F. Carlin, E. Feltin, M. Gonschorek, S. Nicolay, G. Christmann, D. Simeonov, A. Castiglia, J. Dorsaz, H.J. Buehlmann, S. Christopoulos, G. Baldassarri Höger von Hög, A.J.D. Grundy, M. Mosca, C. Pinquier, M.A. Py, F. Demangeot, J. Frandon, P.G. Lagoudakis, J.J. Baumberg, N. Grandjean, Current status of AlInN layers lattice-matched to GaN for photonics and electronics, J. Phys. Appl. Phys. 40 (2007) 6328–6344. doi:10.1088/0022-3727/40/20/S16.
[126] Y. Sakai, P.C. Khai, T. Egawa, Effect of metal-precursor gas ratios on AlInN/GaN structures for high efficiency ultraviolet photodiodes, J. Appl. Phys. 110 (2011) 103523. doi:10.1063/1.3662488.
[127] M.D. Johnson, C. Orme, A.W. Hunt, D. Graff, J. Sudijono, L.M. Sander, B.G. Orr, Stable and Unstable Growth in Molecular Beam Epitaxy, Phys. Rev. Lett. 72 (1994) 116.
[128] S. Vézian, F. Natali, F. Semond, J. Massies, From spiral growth to kinetic roughening in molecular-beam epitaxy of GaN(0001), Phys. Rev. B. 69 (2004). doi:10.1103/PhysRevB.69.125329.
[129] D.V. Dinh, D. Skuridina, S. Solopow, M. Frentrup, M. Pristovsek, P. Vogt, M. Kneissl, F. Ivaldi, S. Kret, A. Szczepańska, Growth and characterizations of semipolar (112-2) InN, J. Appl. Phys. 112 (2012) 013530. doi:10.1063/1.4733997.
[130] H.K. Cho, K.H. Lee, S.W. Kim, K.S. Park, Y.-H. Cho, J.H. Lee, Influence of growth temperature and reactor pressure on microstructural and optical properties of InAlGaN quaternary epilayers, J. Cryst. Growth. 267 (2004) 67–73. doi:10.1016/j.jcrysgro.2004.03.061.
[131] H. Sun, A.R. Alt, H. Benedickter, E. Feltin, J.-F. Carlin, M. Gonschorek, N. Grandjean, C.R. Bolognesi, High-speed and low-noise AlInN/GaN HEMTs on SiC, Phys. Status Solidi A. 208 (2011) 429–433. doi:10.1002/pssa.201000518.
[132] C. Berger, A. Dadgar, J. Bläsing, A. Lesnik, P. Veit, G. Schmidt, T. Hempel, J. Christen, A. Krost, A. Strittmatter, Growth of AlInN/GaN distributed Bragg

reflectors with improved interface quality, J. Cryst. Growth. 414 (2015) 105–109. doi:10.1016/j.jcrysgro.2014.09.008.
[133] Y. Liu, T. Egawa, H. Ishikawa, B. Zhang, M. Hao, Influence of growth temperature on quaternary AlInGaN epilayers for ultraviolet emission grown by metalorganic chemical vapor deposition, Jpn. J. Appl. Phys. 43 (2004) 2414.
[134] Q.Y. Wei, T. Li, Y. Huang, J.Y. Huang, Z.T. Chen, T. Egawa, F.A. Ponce, Compositional instability in InAlN/GaN lattice-matched epitaxy, Appl. Phys. Lett. 100 (2012) 092101. doi:10.1063/1.3690890.
[135] Z.L. Miao, T.J. Yu, F.J. Xu, J. Song, L. Lu, C.C. Huang, Z.J. Yang, X.Q. Wang, G.Y. Zhang, X.P. Zhang, D.P. Yu, B. Shen, Strain effects on InxAl1−xN crystalline quality grown on GaN templates by metalorganic chemical vapor deposition, J. Appl. Phys. 107 (2010) 043515. doi:10.1063/1.3305397.
[136] S. Yamaguchi, M. Kariya, S. Nitta, H. Kato, T. Takeuchi, C. Wetzel, H. Amano, I. Akasaki, Structural and optical properties of AlInN and AlGaInN on GaN grown by metalorganic vapor phase epitaxy, J. Cryst. Growth. 195 (1998) 309–313.
[137] B.P. Burton, A. van de Walle, U. Kattner, First principles phase diagram calculations for the wurtzite-structure systems AlN–GaN, GaN–InN, and AlN–InN, J. Appl. Phys. 100 (2006) 113528. doi:10.1063/1.2372309.
[138] J.A. Purton, M.Y. Lavrentiev, N.L. Allan, Monte Carlo simulation of GaN/AlN and AlN/InN mixtures, Mater. Chem. Phys. 105 (2007) 179–184. doi:10.1016/j.matchemphys.2007.04.024.
[139] T. Takayama, M. Yuri, K. Itoh, T. Baba, J.S. Harris Jr, Analysis of phase-separation region in wurtzite group III nitride quaternary material system using modified valence force field model, J. Cryst. Growth. 222 (2001) 29–37.
[140] T. Takayama, M. Yuri, K. Itoh, J.S. Harris, Theoretical predictions of unstable two-phase regions in wurtzite group-III-nitride-based ternary and quaternary material systems using modified valence force field model, J. Appl. Phys. 90 (2001) 2358–2369. doi:10.1063/1.1388170.
[141] T. Matsuoka, Calculation of unstable mixing region in wurtzite In1- x- yGaxAlyN, Appl. Phys. Lett. 71 (1997) 105–106.
[142] R. Mohamad, A. Béré, J. Chen, P. Ruterana, Investigation of strain effects on phase diagrams in the ternary nitride alloys (InAlN, AlGaN, InGaN): Strain effects on phase diagrams in the ternary nitride alloys, Phys. Status Solidi A. 214 (2017) 1600752. doi:10.1002/pssa.201600752.
[143] A.K. Kandalam, R. Pandey, M.A. Blanco, A. Costales, J.M. Recio, J.M. Newsam, First Principles Study of Polyatomic Clusters of AlN, GaN, and InN. 1. Structure, Stability, Vibrations, and Ionization, J. Phys. Chem. B. 104 (2000) 4361–4367. doi:10.1021/jp994308s.
[144] M. Marques, L.K. Teles, L.M.R. Scolfaro, L.G. Ferreira, J.R. Leite, Microscopic description of the phase separation process in Al x Ga y In 1 − x − y N quaternary alloys, Phys. Rev. B. 70 (2004). doi:10.1103/PhysRevB.70.073202.
[145] B.P. Burton, A. van de Walle, U. Kattner, First principles phase diagram calculations for the wurtzite-structure systems AlN–GaN, GaN–InN, and AlN–InN, J. Appl. Phys. 100 (2006) 113528. doi:10.1063/1.2372309.
[146] J.A. Purton, M.Y. Lavrentiev, N.L. Allan, Monte Carlo simulation of GaN/AlN and AlN/InN mixtures, Mater. Chem. Phys. 105 (2007) 179–184. doi:10.1016/j.matchemphys.2007.04.024.
[147] V.G. Deibuk, A.V. Voznyi, Thermodynamic stability and redistribution of charges in ternary AlGaN, InGaN, and InAlN alloys, Semiconductors. 39 (2005) 623–628.

[148] L. Rigutti, B. Bonef, J. Speck, F. Tang, R.A. Oliver, Atom probe tomography of nitride semiconductors, Scr. Mater. (2017). doi:10.1016/j.scriptamat.2016.12.034.
[149] H. Morkoç, Nitride Semiconductors and Devices, Springer Berlin Heidelberg, Berlin, Heidelberg, 1999. doi:10.1007/978-3-642-58562-3.
[150] U.K. Mishra, P. Parikh, Y.-F. Wu, AlGaN/GaN HEMTs-an overview of device operation and applications, Proc. IEEE. 90 (2002) 1022–1031.
[151] L. Shen, S. Heikman, B. Moran, R. Coffie, N.-Q. Zhang, D. Buttari, I.P. Smorchkova, S. Keller, S.P. DenBaars, U.K. Mishra, AlGaN/AlN/GaN high-power microwave HEMT, IEEE Electron Device Lett. 22 (2001) 457–459.
[152] F. Medjdoub, R. Kabouche, A. Linge, B. Grimbert, M. Zegaoui, P. Gamarra, C. Lacam, M. Tordjman, M.-A. di Forte-Poisson, High electron mobility in high-polarization sub-10 nm barrier thickness InAlGaN/GaN heterostructure, Appl. Phys. Express. 8 (2015) 101001. doi:10.7567/APEX.8.101001.
[153] Q. Fareed, A. Tarakji, J. Dion, M. Islam, V. Adivarahan, A. Khan, High voltage operation of field-plated AlInN HEMTs, Phys. Status Solidi C. 8 (2011) 2454–2456. doi:10.1002/pssc.201001103.
[154] Y.-R. Wu, M. Singh, J. Singh, Gate leakage suppression and contact engineering in nitride heterostructures, J. Appl. Phys. 94 (2003) 5826–5831. doi:10.1063/1.1618926.
[155] J. Kuzmik, J.-F. Carlin, M. Gonschorek, A. Kostopoulos, G. Konstantinidis, G. Pozzovivo, S. Golka, A. Georgakilas, N. Grandjean, G. Strasser, D. Pogany, Gate-lag and drain-lag effects in (GaN)/InAlN/GaN and InAlN/AlN/GaN HEMTs, Phys. Status Solidi A. 204 (2007) 2019–2022. doi:10.1002/pssa.200674707.
[156] E. Bahat-Treidel, O. Hilt, F. Brunner, V. Sidorov, J. Würfl, G. Tränkle, AlGaN/GaN/AlGaN DH-HEMTs Breakdown Voltage Enhancement Using Multiple Grating Field Plates (MGFPs), IEEE Trans. Electron Devices. 57 (2010) 1208–1216. doi:10.1109/TED.2010.2045705.
[157] G. Xie, E. Xu, J. Lee, N. Hashemi, B. Zhang, F.Y. Fu, W.T. Ng, Breakdown-Voltage-Enhancement Technique for RF-Based AlGaN/GaN HEMTs With a Source-Connected Air-Bridge Field Plate, IEEE Electron Device Lett. 33 (2012) 670–672. doi:10.1109/LED.2012.2188492.
[158] J. Guo, G. Li, F. Faria, Y. Cao, R. Wang, J. Verma, X. Gao, S. Guo, E. Beam, A. Ketterson, M. Schuette, P. Saunier, M. Wistey, D. Jena, H. Xing, MBE-Regrown Ohmics in InAlN HEMTs With a Regrowth Interface Resistance of 0.05 Ω · mm, IEEE Electron Device Lett. 33 (2012) 525–527. doi:10.1109/LED.2012.2186116.
[159] P. Gamarra, C. Lacam, M. Magis, M. Tordjman, M.-A. di F. Poisson, The effect of ammonia flow in the AlN spacer on the electrical properties of InAlN/AlN/GaN HEMT structures, Phys. Status Solidi A. 209 (2012) 21–24. doi:10.1002/pssa.201100090.
[160] M. Rzin, Impact of gate-drain spacing on low frequency noise performance of in-situ SiN passivated InAlGaN/GaN MIS-HEMTs, IEEE Trans. Device Mater. Reliab. (n.d.).

Publications and contributions to conferences

Publications

1. *The structure of InAlGaN layers grown by metal organic vapour phase epitaxy: effects of threading dislocations and inversion domains from the GaN template* ***H. Ben Ammar***, A. Minj, M.-P. Chauvat, P. Gamarra, C. Lacam, M. Morales, P. Ruterana, , J. Microsc. (2017). doi:10.1111/jmi.12651.

2. *Gallium incorporation in InAlN: role of the chamber design and history, and the effects of growth pressure: Gallium incorporation in InAlN* ***H. Ben Ammar***, A. Minj, P. Gamarra, C. Lacam, M. Tordjman, M.A. di Forte-Poisson, M. Morales, M.-P. Chauvat, P. Ruterana, Phys. Status Solidi A. **214** (2017) 1600441. doi:10.1002/pssa.201600441.

3. *InAlGaN/GaN HEMTs at Cryogenic Temperatures* E. Dogmus, R. Kabouche, S. Lepilliet, A. Linge, M. Zegaoui, ***H. Ben Ammar***, M.-P. Chauvat, P. Ruterana, P. Gamarra, C. Lacam, M. Tordjman, F. Medjdoub, Electronics. **5** (2016) 31. doi:10.3390/electronics5020031.

Contribution to conferences

1. Poster presentation during The Royal Microscopical Society (RMS) conference in Oxford (UK) April 2017: *Structural disruption in InAl(Ga)N/GaN heterostructures* **H. Ben Ammar**, A. Minj, P. Gamarra, C. Lacam, M. Tordjman, M. Morales,M. P. Chauvat, and P. Ruterana.

2. Oral Presentation during The European Materials Research Society (EMRS) conference in Lille (France) April 2016: *Defects generation mechanisms in InAlN layers grown by metal organic vapor phase epitaxy* **H. Ben Ammar**, M.-P. Chauvat, A. Minj, M. Morales, P. Gamarra, C. Lacam, M. Tordjman, M.A. Di Forte-Poisson, and P. Ruterana

3. Oral Presentation during The European Materials Research Society (EMRS) conference in Warsaw (Poland) September 2015: *Influence of growth parameters on the structure of InAlN layers grown by metal organic vapor phase epitaxy* **H. Ben Ammar**, M.-P. Chauvat, M. Morales, P. Gamarra, C. Lacam, M. Tordjman, M.A. Di Forte-Poisson, and P. Ruterana.

Analyse d'alliages ternaire et quaternaire (Al, Ga, In)N pour application aux transistors à haute mobilité électronique par microscopie électronique en transmission.

Résumé :

Les semi-conducteurs III-V à base d'azote et leurs alliages possèdent des propriétés remarquables et sont largement étudiés depuis les années 90. En comparaison à d'autres semi-conducteurs III-V, Les alliages de type ; AlGaN, InGaN et AlInN, ont leurs bandes interdites, directes, du lointain ultra-violet au proche infrarouge. Ainsi, ils sont appropriés pour de nombreuses applications dans des domaines tant civils que militaires tout en montrant de meilleures performances. De plus, l'alliage quaternaire AlGaInN montre des propriétés intéressantes car il peut être épitaxié soit avec un paramètre de maille ou une polarisation ou une bande interdite accordé au GaN. De plus, avec AlInN, ces deux alliages pourraient, à terme, remplacer les barrières conventionnelles AlGaN/GaN pour les applications aux Transistors à Haute Mobilité Électroniques (HEMT) grâce à des performances supérieures prouvées théoriquement.

Dans ce travail, nous avons étudié les alliages AlInN et AlGaInN dont la croissance a été faite par épitaxie en phase vapeur d'organométalliques (MOVPE). Pour cela, la microscopie électronique en transmission a été notre principal outil de caractérisation. Le but était de caractériser les défauts et les mécanismes de croissance pendant la MOVPE. Dans cette optique, l'incorporation de gallium dans la barrière en raison de la géométrie de la chambre de croissance menant à un alliage quaternaire a été étudiée. Le contrôle du taux de gallium est réalisé soit par un processus de nettoyage entre les épitaxies soit par les conditions de croissance. Les défauts ont été ensuite différenciés comme extrinsèques et intrinsèques. En effet, les dislocations et les domaines d'inversion dans le GaN produisent des défauts extrinsèques, tandis que, les « pinholes » non connectés aux dislocations et les « hillocks » responsables de la rugosité de surface sont définis comme intrinsèques. Les origines des défauts intrinsèques dépendent fortement des propriétés physiques des composés parents binaires. Ces dégradations systématiques sont observées même lorsque les conditions de croissance sont optimisées et quand la composition du film mince est changée ou son épaisseur augmentée.

Notre travail propose des mécanismes différents pour expliquer les processus de dégradation pour les différents défauts observés et constitue donc un pas en avant pour la réalisation de HEMT à base de AlInN et AlGaInN de meilleure qualité.

Mots clés : AlInN, AlGaInN, TEM, AFM, APT, HEMT, séparation de phase, pinholes, hillocks

Investigation of ternary and quaternary (Al, Ga, In)N alloys for High Electron Mobility Transistors by Transmission Electron Microscopy.

Abstract:

Group III-Nitrides and their alloys exhibit outstanding properties and are being extensively investigated since the 90's. In comparison to other III-V semiconductors, III-nitrides (AlGaN, InGaN, and AlInN) cover from deep ultraviolet (UV) to near infrared (IR) across the visible range of wavelengths. Thus, they are suitable for numerous applications both in civilian and military fields showing higher performances. Moreover, the quaternary alloy AlGaInN shows versatile properties as it can grow either lattice or polarization or bandgap matched to GaN. Alongside to AlInN, these two alloys are expected to replace conventional AlGaN/GaN High Electron Mobility Transistors (HEMT) barriers as higher performances have been theoretically demonstrated.

In this work, we have studied AlInN and AlGaInN grown by metal organic vapor phase epitaxy (MOVPE) using mainly TEM. The aim was to characterize defects and the MOVPE growth alloying process. In this instance, the gallium incorporation in the barrier due to the geometry of the growth chamber leading to a quaternary alloy was studied. The control of the gallium content is achieved by a cleaning process between runs or by the growth condition. Defects were then differentiated as extrinsic and intrinsic. In this way, dislocations and inversion domains from the GaN buffer layer generate extrinsic defects, while, pinhole not connected to dislocations and individual hillocks responsible of surface roughening are termed as intrinsic. The origins of the latter defects depend strongly on the physical mismatches of the end-binary compound. These systematic degradations happen also with optimized growth conditions as soon as the nominal composition is changed and/or the thickness is increased.

Our work proposes different mechanisms to explain defects generation processes which constitutes a forward step for higher quality HEMTs.

Keywords: AlInN, AlGaInN, TEM, AFM, APT, HEMT, phase separation, pinholes, hillocks,